Maximilian Schachner-Nedherer, BSc.

Image based monitoring of civil structures and natural phenomena

MASTER'S THESIS

to achieve the university degree of

Master of Science

Master's degree programme: Geomatics Science

submitted to

Graz University of Technology

Supervisor

Univ.-Prof. Dipl.-Ing. Dr.techn. Werner Lienhart

Institute of Engineering Geodesy and Measurement Systems

Graz, December 2019

AFFIDAVIT

I declare that I have authored this thesis independently, that I have not used other than the declared sources/resources, and that I have explicitly indicated all material which has been quoted either literally or by content from the sources used. The text document uploaded to TUGRAZonline is identical to the present master's thesis.

_____	_____
Date	Signature

Acknowledgements

I would like to express my appreciation to all the people who supported me during the writing of my thesis.

First of all, it would like to thank my supervisor Univ.-Prof. Dipl.-Ing. Dr.techn. Werner Lienhart, who guided and advised me throughout the whole research and writing process of my thesis and helped me to broaden, deepen and apply my knowledge within the evaluation of deformation monitoring.

My appreciation also goes to Dipl.-Ing. Slaven Kalenjuk, Dipl.-Ing. Peter Bauer and Dipl.-Ing. Christoph Monsberger. All of them supported me in different stages and always had a sympathetic ear for my questions.

In addition, a special thanks goes to my fellow students, who have been best associates in discussing current technical issues and in having multiple cups of coffee.

I would also like to express my huge gratitude to my parents Sabine and Alfred, who made my studying and graduation possible in the first place. Their support was an invaluable asset. Furthermore, my thanks goes to my sisters Anna-Laurence and Valentina for their personal support.

Finally, a huge thanks goes to my fiancée Anita, who helped me through all stages of my thesis and often regained my energy by her encouragement. Although working on her own thesis, she supported me whenever she could.

Abstract

The implementation of remote measuring systems, which do not require access to civil structures, cause a paradigm shift in engineering geodesy. As a consequence, manufacturers of surveying instruments develop new total stations, where, for instance, camera systems are integrated. These upgraded instruments are known as image-assisted total station (IATS).

Here, the combination of precise angle and distance measurements with image and video recordings is possible. To accomplish different surveying tasks for this thesis, the Leica Nova MS60 MultiStation (Leica MS60), equipped with an inbuilt 5 Mpx sensor, allows high-resolution image recordings. To assess the capability of the telescope camera, also known as on-axis camera (OAC), a deformation monitoring at Wald am Schoberpass (Styria) is used as a testing scenario.

In the course of the data evaluation, the implemented measurement routines are investigated to achieve improvements concerning the image and video recordings. Here, the steering procedure, the image exposure, an automated image analysis and the transformation from image coordinates to telescope angles are at the core of interest.

Additionally, an evaluation approach is introduced, which is based on measurements using an automatic target recognition technique. The obtained measurement noise is used as basis for the assessment of angle observations, which in a deformation monitoring would possibly indicate rigid body motion.

Kurzfassung

Der Einsatz von Messsystemen, welche nicht zwangsläufig einen direkten Zugang zum Messobjekt voraussetzen, bewirken teilweise einen Paradigmenwechsel in der Ingenieurvermessung. Das bedeutet, dass auch die Hersteller Produktlinien für neue Messinstrumente entwickeln, welche z.B. mit mehreren Kameras versehen sind. Die gängige Bezeichnung für diese Geräte ist Video-Totalstation.

Diese Umsetzung ermöglicht die Kombination von genauen Richtungs- und Distanzmessungen mit zusätzlicher Bildaufnahme, wobei die für diese Arbeit verwendete Multistation, die Leica MS60, mit Hilfe eines 5 Mpx Sensors arbeitet und somit hochauflösende Bild- und Videoaufnahmen möglich sind. Um diesen zusätzlichen Sensortyp zu testen, wurden im Zuge einer Rutschhangmessung in Wald am Schoberpass (Steiermark) Bild- und Videodaten aufgezeichnet, um die Leistungsfähigkeit der Teleskopkamera zu testen.

Im Zuge der Auswertungen werden die eingesetzten Messroutinen bewertet bzw. Verbesserungen im Zuge der Bildaufnahme vorgeschlagen. Dabei spielen das Ansteuern des Ziels, die richtige Belichtung, eine automatisierte Bildauswertung und Umrechnung der Bildkoordinaten in Winkelwerte eine zentrale Rolle.

Zusätzlich dazu wird eine Evaluierungsansatz vorgeschlagen, welcher auf dynamisch durchgeführten Messungen mit automatischer Zielerfassung basiert. Das sich dabei ergebende Messrauschen wird als Grundlage für die Bewertung von Winkelmessungen verwendet, welche im Zuge eines geodätischen Monitorings Objektbewegungen vermuten lassen.

Contents

List of Figures

List of Tables

List of abbreviations

AI	artificial intelligence
AIT	Austrian Institute of Technology
AOV	angle of view
ASCII	American Standard Code for Information Interchange
ATR	automated target recognition
CCD	charged-coupled device
CV	computer vision
CMOS	complementary metal-oxide-semiconductor
DIC	digital image correlation
DoG	difference of two Gaussians
DSLR	digital single-lens reflex
EDM	electronic distance measurement
FFT	fast Fourier transform
FLANN	fast library for the approximate nearest neighbors
IATS	image-assisted total station
IGMS	Institute of Engineering Geodesy and Measurement Systems
IRM	image registration or matching
LED	light-emitting diode
Leica	Leica Geosystems
Leica MS60	Leica Nova MS60 MultiStation
Leica TS15	Leica Viva TS15 TotalStation
LoG	Laplacian-of-Gaussian
LOS	line-of-sight
MAD	median absolute deviation
OAC	on-axis camera
OVC	overview camera
OpenCV	Open Source Computer Vision Library
PC	personal computer
RTS	robotic total station
RANSAC	random sample consensus
SAR	synthetic aperture radar
SHM	structural health monitoring
SIFT	scale-invariant feature transform
SoI	set of images
SoV	set of videos
SURF	speeded up robust features
TOF	time of flight
TU Graz	Graz University of Technology

1 Introduction

This chapter is a short introduction of the topic and thesis. Here, the motivation and interests of the stakeholders are described and the referring outline of the thesis is stated. Furthermore, related publications are presented, which have an impact on the underlying research.

1.1 Motivation

Nowadays existing geodetic measurement methods and processes are often assessed to reduce costs and time. For example, formerly two surveyors in the field were standard, but this is now questioned. In fact, innovations along the workflow have fundamentally changed approaches to solve geodetic tasks. Area measurements based on remote systems are more attractive and easier to handle than measuring prisms, which are cumbersomely installed on the objects of interest (Barras and Chapotte, 2017).

The objective of this thesis focuses on the use of image-based sensors which are already included in commercially available instruments like the Leica Nova MS60 MultiStation (Leica MS60). Combining a high-tech robotic total station (RTS) with image-based sensors increases the possible field of applications and offers different ways of performing geodetic measurements. The very precise angle and distance measurements of the Leica MS60 adds further dimensions to a picture concerning orientation and scale, because detecting motion is limited by the vertical and horizontal axis of the 2D image sensor plane. Therefore, combining image-based sensor techniques with position, scale and orientation given by the RTS is a huge advantage.

Using this combination the idea is to test an image-assisted total station (IATS) in the framework of a real application like the monitoring of a landslide at Wald am Schoberpass located in Styria, Austria. The ASFiNAG, which is responsible for the federal road network, classified this landslide as a possible risk for the nearby highway. Hence, it was monitored closely by an engineering office using a RTS and prisms.

This landslide is used as a test site to evaluate image-based monitoring techniques in order to give a valid statement concerning their functionality and additionally to point out advantages and disadvantages of image-based approaches when comparing them to the precise angle and distance measurements of the Leica MS60. Consequently, the heretofore implemented application protocols, which are included in the software modules and define the measurement procedures, have to be analysed. Based on different experiments, the routines should be enhanced for an even better workflow.

Concluding, a rethought approach for further field experiments like landslide monitoring should be introduced, discussing possible advantages compared to the previous used routines and how to compensate systematic deficits such as orientation and inclination drift and the impact of refraction on the angle readings during a field test.

1.2   Thesis outline

In chapter 2, the standard techniques to measure angles, distances and inclinations are presented. Furthermore, monitoring is defined and set into context of this thesis. Additionally, current state-of-the-art RTS and IATS are introduced.

Due to different approaches on how to extract information from an image, chapter 3 describes the basic components that are relevant when taking images. Common image evaluation techniques are discussed, which are able to solve issues of motion and deformation detection and if there are advantages and disadvantages due to different application requests.

In chapter 4, the relations of image-based observations and automated target recognition (ATR) based measurements are highlighted. Furthermore, a comparison between these two approaches is performed to describe possible issues, when combining them for an automated measurement routine.

Based on the knowledge that automatic target recognition is a common tool for deformation monitoring, an analysis of the ATR mode of Leica Geosystems (Leica) is given in chapter 5. Here, a measurement campaign is performed to assess the capabilities of this technique. Additionally, it is discussed how the measurement noise of dynamic ATR measurements can be used as an indicator to evaluate alarming measurements, because when dynamic or static systems are monitored various systematic effects influence the entire system. These aspects also have impact on taking images.

An overview of the measurement campaign at Wald am Schoberpass is given in chapter 6. Here, the measurement setup, the different measurement procedures and evaluation routines are described. The RTS measurements are used to verify a possible deformation of the landslide. Furthermore, the results obtained via image and video recordings are assessed concerning their usability for rockfall monitoring.

Following, different approaches are discussed which enhance previous used measurement protocols that have already been introduced in the underlying work of Ehrhart (2017). Here, especially the procedure of taking images is at the core of interest (section 7.1). Especially, an altered steering procedure and the adaptation of image settings during the set measurements is described.

The final chapter 8 gives a summery and outlook based on the knowledge gained during the research for this thesis. Occurring issues during the measurement campaign at Wald am Schoberpass are stated and further topics are proposed for subsequent investigations when it comes to an epoch wise deformation monitoring based on images and videos.

1.3   Related Publications

This thesis is related to the work of Ehrhart (2017), where surveying instruments and applications for image-based monitoring are introduced. Furthermore, concepts and routines are described, which are

of importance when it comes to the evaluation procedure of images and videos. Additionally, investigations concerning the known effect of refraction are performed and how its influence is measurable when using a state-of-the-art IATS.

2   State-of-the-art of monitoring with total stations

In this chapter, the measurement techniques of total stations are explained. Current commercial available IATS are discussed and their specifications are compared. Based on these, the used instruments for this thesis are introduced and how they have already been used for various static or dynamic measurements.

2.1   Principles of total station measurements

In the following sections, the basic measurement principles of geodetic observation quantities are described. Relevant to this thesis are angle, distance and tilt compensator measurements. Additionally, the concept of Leica's target recognition also known as ATR is outlined.
Although this thesis mainly handles the use of a commercial available IATS, the inbuilt camera systems are still fixed to a rotating platform, which is equivalent to a RTS. Therefore, the basic observations are not only necessary for performing a monitoring based on total station, but furthermore, the computation of image-based angles is built up on these observations, such as the measurements of the inbuilt angle encoders and the tilt compensator.

2.1.1   Angle measurement

The first measured quantities are the horizontal angle Hz and the vertical angle V. The vertical component can be seen as an absolute quantity referring to the plumb line, whereas the horizontal angle depends on the orientation settings of the theodolite. Their basic definitions are given by the instrument axis which are described as

- Vertical axis (S)

- Tilt axis (T)

- Collimation axis (C).

The horizontal angle is defined by the rotation about the vertical axis and is recorded by angle encoders, which are fixed to the underbody of the instrument. The vertical angle is described by the rotation about the tilt axis and is recorded by angle encoders which are fixed to the telescope of the instrument. Both components and the axis orientations are depicted in figure 2.1a.
The angle reading procedure consists of a coded circle made out of glass and up to four referring reading units. The basic principle is that an optical signal emitted by a light-emitting diode (LED) hits the glass circle illuminating a code which is received by a line sensor. The resulting code image is decrypted by an algorithm developed by Leica. The advantage of the printed code is that it is absolute and continuously. Like for e.g. the Leica MS50 or Leica MS60, four installed encoders and a high measurement frequency of up to 5000 Hz increase the quality of angles readings due to the minimization of systematic and periodic errors. Therefore, besides the precision also the reliability is significantly improved (Zogg et al., 2019, p.6).

(a) Schematic representation of the instrument axis which define the horizontal and vertical angle, after Deumlich and Staiger (2002)

(b) Visualization of the angle encoder including a light source, the coded glass circle and line sensor (Zogg et al., 2019, p.6)
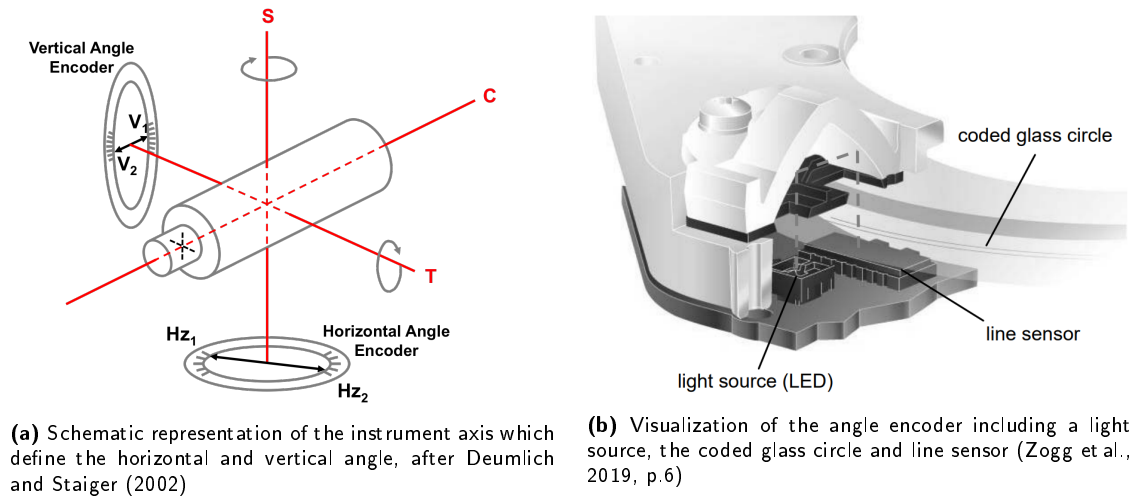
Figure 2.1: Principles of an angle measurement

2.1.2   Tilt compensator

The tilt compensator readings are used to evaluate the stability of the instrument. To do so, there are several approaches. According to Zogg et al. (2019), the current used technique implemented in Leica instruments is a 2-axis inclination sensor. Its longitudinal and transversal inclination readings are needed to correct Hz and V. As shown in figure 2.2, the principle is depicted and due to the movement of the line code along and across the line sensor, the tilt of the instrument in both axes can be indicated.

The inclination sensor or tilt compensator includes a light emitting source, an oil layer and a glass prism having a specific line code printed and the line sensor. Due to a specific order, the light passes through the oil and the prism projecting the line code of the sensor. Dealing with an inclination in longitudinal direction the centre of the line code moves along the sensor, having a transversal inclination the distance between the line groups changes.
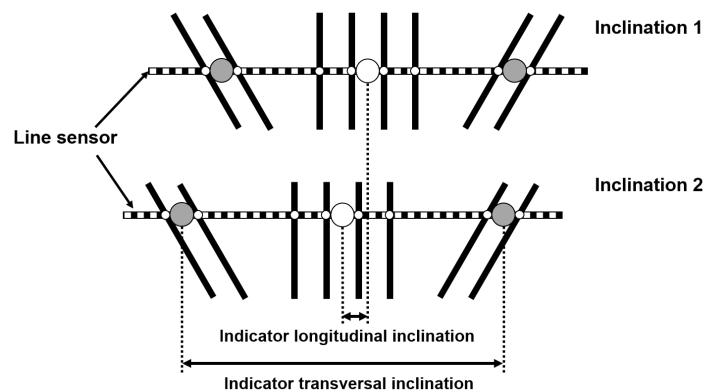
Figure 2.2: Schematic representation of the inclination measurement based on a line sensor and specific line code, after Zogg et al. (2019)

2.1.3   Distance measurement

The distance measurement is performed using EDM technology. The basic principle can be separated into two different techniques. One measures the time of flight (TOF) of the emitted light signal, the other one is known as phase shift measurement as described e.g. by Bayoud (2006) and Joeckel and Stober (1999).

The TOF principle is based on measuring the time difference δt of an emitted signal and its reflected counterpart. In combination with the velocity of light $\mathrm{v_c}$ in a specific medium, the distance $\mathrm{d_{TOF}}$ is the product of multiplying the time with the velocity $\mathrm{v_c}$ divided by two, as the path is twice the travelled light distance. Figure 2.3a depicts the principle, which is based on light impulses coming from a transmitter and measured by the receiver.

On the other hand, the phase shift measurement is based on specific wave lengths. Using a basic scale λ the integer counts, also known as ambiguities, plus the measurement fractional part $\delta\varphi$ of a single wavelength are used to determine the distance between instrument and target, shown in figure 2.3b. For both techniques, the properties of the target (type, material, surface) have to be considered to obtain a successful distance measurement.

(a) TOF

(b) Phase shift measurement
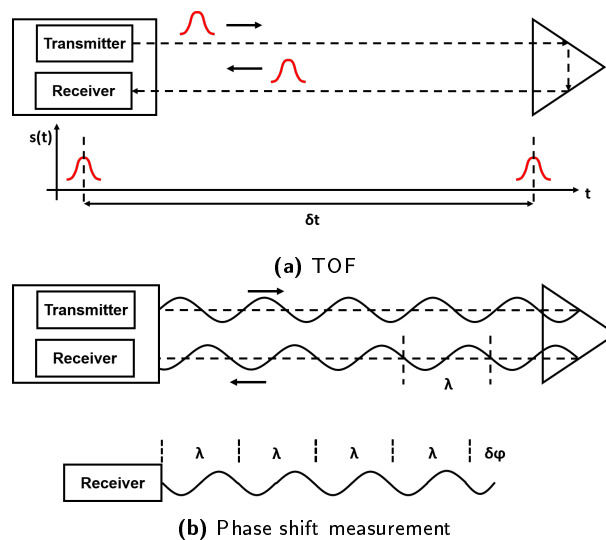
Figure 2.3: Schematic visualization of different types of EDM, after Bayoud (2006)

2.1.4   Automatic target recognition

Manufacturers have different implementations of automatic image recognition in currently avaiable RTS. Following industry examples are most widely spread (Weyman-Jones, 2010, p.1):

- Automatic Target Recognition (ATR, Leica Geosystems)

- AutoLock / FineLock (Trimble Navigation Ltd.)

- X-TRAC (Topcon)

- Auto Pointing (Sokkia)

This thesis utilises Leica surveying instruments, thus the ATR technique is or primary interest. The basic procedure is a laser emits a coaxial infrared light with a divergence of 1.5 gon via a telescope. The signal is reflected from a target or rather a prism onto a complementary metal-oxide-semiconductor (CMOS) sensor (Leica-Geosystems, 2015a, p.3). Due to its position relatively to the sensor's centre, the received signal is evaluated and compared to a certain threshold. Based on this comparison the decision is made whether the telescope's position has to be adjusted or the deviations due to the current field of view are small enough to correct the sighting axis mathematically. The threshold is about 5 mgon (Leica-Geosystems (2008); Bayoud (2006)). The precision of the newer ATR+ implemented in the Leica MS60 equals 0.3 mgon (Leica-Geosystems, 2015a, p.8).

2.2   State-of-the-art of image-assisted total stations with on-axis cameras

Various manufacturers presently offer geodetic surveying instruments, which refer to an IATS. Based on their specifications, Lachat et al. (2017) listed in their research the Leica MS60, the Topcon IS-3 and the Trimble SX10. These instruments do not only comprise the functionality of a modern RTS, but also include different combinations of cameras and offer scanning functionality. The IATS concepts have different designs, which require definition of specifications. Ehrhart (2017) describes these as follows:

- the pixel resolution of the image sensor in vertical and horizontal direction.

- the field of view defined as the angle of view (AOV) in vertical and horizontal direction. This quantity represents the extent of the depicted scenery.

- the relation between pixel and angle resolution defined as angle per pixel

$$\alpha_{\mathrm{px}} \approx \frac{\mathrm{AOV}}{\text{number of pixels}}. \tag{2.1}$$

  This value varies depending on the pixel position of the sensor. Apart from these variations, it is an indicator and therefore can be used to roughly estimate angle accuracies.

- the available frame rates, which are of interest when it comes to monitor moving structures. Depending on the frame rate e.g. the oscillation frequency of an object can be determined.

Based on these specifications, table 2.1 shows the referring values for the different imparted IATSs.

Table 2.1: Specifications taken from the datasheets and brochures of Leica-Geosystems (2019a), Topcon (2019) and Trimble (2016–2017) concerning the measurement capabilities

	Leica MS60	Topcon IS-3	Trimble SX10
	pixel resolution [px×px]		
	2560×1920 (5 Mpx)	1280×1024 (1.3 Mpx)	2592×1944 (5 Mpx)
	AOV [gon×gon]		
Telescope camera	1.3×1.0	0.9×0.7	2.9×2.2
Wide-angle camera	17.2×13.0	28.6×22.9	14.4×11.1
			63.9×47.8
	α_{px} [mgon/px]		
Telescope camera	0.5	0.7	1.1
Wide-angle camera	6.7	22.4	5.6
			24.6
	max. frame rate [fps]		
	20	10	15

2.3 Used total stations in this thesis

As stated previously, this thesis requires instruments to have both a RTS and an IATS, more specifically the Leica MS60 was chosen as it is comercially avaiable and state-of-the-art. Besides the very precise angle and distance measurement, the instrument has two cameras, an overview camera (OVC) based utilising a wide angle lens and an on-axis camera (OAC) also known as telescope camera. Additionally, the Leica MS60 comprises scanning functions performing with an measurement rate of up to 1000 Hz. In table 2.2 the serial number is given, in table 2.3 the angle and distance data is stated and table 2.4 shows the key inbuilt camera specifications.

Table 2.2: Name and serial number of the used Leica MS60

Name	Serial number
Leica MS60 I R2000	882001

Table 2.3: Specifications concerning the measurement capability of the Leica MS60 (Leica-Geosystems, 2019a; Ehrhart, 2017)

Angle Measurement	
Accuracy	0.3 mgon
ATR+ accuracy	0.3 mgon
Distance Measurement	
Type	Coaxial, visible red laser
Carrier wave	658 nm
Measuring system	R2000: Wave Form Digitizer
Accuracy in standard mode (with reflectors)	1 mm + 1.5 ppm
Accuracy in standard mode (without reflectors)	2 mm + 2.0 ppm

Table 2.4: Specifications concerning the image and video capabilities of the Leica MS60 (Leica-Geosystems, 2019a; Ehrhart, 2017)

Overview camera	
Sensor	5 Mpixel CMOS sensor
Focal length	21 mm
Field of view	17.2 x 13.0 mgon
Frame rate	$\leq$ 20 frames per second
Focus range	2.0 m to infinity
Image storage	JPEG up to 5 Mpixel (2560 x 1920)
White balance	Automatic and user configurable
ISO (automatically, manually)	[75 - 225 - 562 - 2249 - 9002]
Exposure time (automatically, manually)	0.0001 to 0.48 sec
α_{px}	6.7 mgon/px
Telescope camera	
Sensor	5 Mpixel CMOS sensor
Focal length	231 mm at focus infinity
Field of view	1.6 x 1.2 mgon
Frame rate	$\leq$ 20 frames per second
Focus range	1.7 m to infinity
Image storage	JPEG up to 5 Mpixel (2560 x 1920)
White balance	Automatic and user configurable
ISO (automatically, manually)	[88 - 220 - 553 - 2212 - 8850]
Exposure time (automatically, manually)	0.0001 to 0.48 sec
α_{px}	0.6 mgon/px

Besides the use of the Leica MS60 for the landslide monitoring, additionally the Leica Viva TS15 TotalStation (Leica TS15) is used for field tests. The relevant facts are listed in table 2.5. Even though the instrument also is equipped with an OVC, nevertheless this feature was not relevant for further investigations when using the Leica TS15.

Table 2.5: Specifications concerning the measurement capability of the Leica TS15 (Leica-Geosystems, 2019b)

Angle measurement	
Accuracy	0.3 mgon
ATR accuracy	0.3 mgon
Distance measurement	
Principle	Phase measurement
Type	Coaxial, visible red laser
Carrier wave	658 nm
Measuring system	System analyser basis 100 MHz - 150 MHz
Accuracy in standard mode (with reflectors)	1 mm + 1.5 ppm
Accuracy in standard mode (without reflectors)	2 mm + 2.0 ppm

2.4 Meaning of geodetic monitoring

The main monitoring goal is detecting and defining an or multiple objects' movement. This includes the metrological observation and evaluation of the gathered data derived from the deformed object.

Consequently, deformation measurements require different planning, implementation, evaluation and documentation (Heunecke et al., 2013, p.1).

Seen in the context of civil structures, monitoring is indispensable and also the basis of any action plan. Therefore, geodetic measurements have gained in significance for being a reliable method for gathering accurate and replicable results.

To provide meaningful data describing the movement of an object, a geometrical and temporal discretization has to be performed (Heunecke et al., 2013, pp.26-31). Furthermore, it is important to choose the right sensor technology to guarantee scalability of possible deformations. Rigid body motion and distortion needs to be differentiated (Heunecke et al., 2013, pp.93-94). Based on the geometrical discretization (point-wise or area-based) it can be classified whether the deformation equals a rigid body motion or a distortion, shown in figure 2.4.

Temporal discretisation is required to show if there are short or long term changes to the object (figure 2.5). Depending on the required time scale different measurements and analysis methods have to be considered.
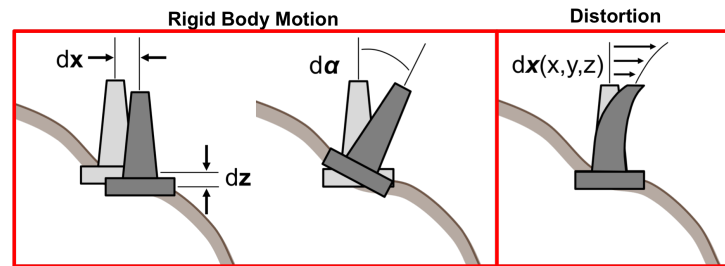
Figure 2.4: Schematical overview of rigid body motion, after Heunecke et al. (2013)
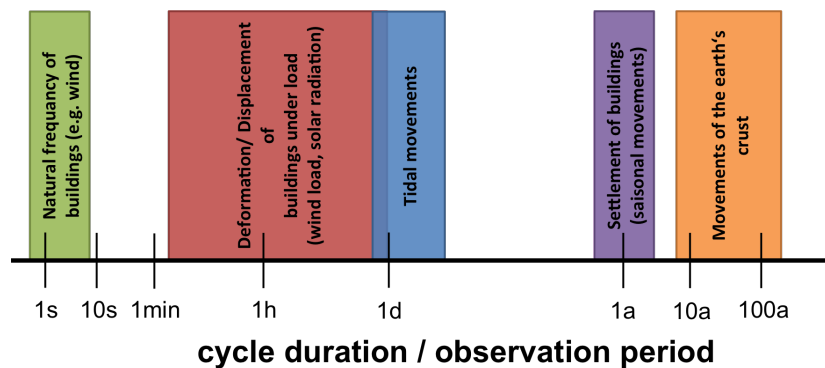
Figure 2.5: Description of different time depending motion, also known as cycle durations, after Lienhart (2017a)

2.4.1   Monitoring of landslides

Landslides are a natural phenomena, which amongst others are at the core of interests in monitoring applications (Wunderlich, 2006). Physically, landslides can be described as the movement of a mass of rock, debris or earth down a slope (Sassa et al., 2007, p.5).Varnes (1978) describes several landslide types. Due to their devastating consequences, construction sites are observed far in advance of

construction work. For example, the area of the Gotthard Basetunnel was monitored for years prior to commencing drilling, as described by Ryf and Studer (2014). The primary interest was to ensure if any natural disasters could happen as a result from construction work.

Summarising, landslide science consists of different branches, all concerned with stability and safety assesments. Sassa et al. (2007) describes these as follows:

- Water Sciences (Meteorology, Hydrology, Hydraulics, etc.)

- Earth Sciences (Geology, Geomorphology, Seismology, Volcanology, Geodesy, etc.)

- Engineering Sciences (Civil Engineering, Forest Engineering, Mining Engineering, etc.)

- Social Sciences (Policy, Administration, Risk Management, Recovery, etc.)

- Culture Heritage and the Environment (Protection of cultural heritage sites and the environment)

2.4.2   Image based monitoring applications

Previous applications using a current state-of-the-art IATS mainly have been dealing with bridge monitoring. In Ehrhart (2017) different approaches (static, dynamic) are introduced to describe the behaviour of a bridge. Here not only the maximum amplitude of the bridge bending, but also the natural oscillation are of primary interest.

One research object was a road bridge over the river Schwechat near to Mannwörth, Austria, that was statically monitored. The bridge, due to its planned replacement by a newer construction, was artificially damaged to evaluate safety assessments based on measurements. The selective destruction should simulate ageing effects. Here, the Institute of Engineering Geodesy and Measurement Systems (IGMS) was able to use the Leica MS60 carrying out IATS measurements.

The final results, obtained by IATS, were compared to the recorded information of a tilt sensor operated by the Austrian Institute of Technology (AIT), who were responsible for this field test. Here, different positions along the bridge pillar and bridge deck were observed to identify different regions and how they were affected by artificial ageing. During a 23 hour period, the inclination measurements of the bridge deck derived by the tilt sensor and the IATS based observations both yielded a similar result. The damage at the bridge pillar influenced the entire bridge, which was captured successfully by the Leica MS60. These results fitted to the temperature-corrected inclinometer measurements of the AIT, which confirmed the suitability using a IATS for static deformation monitoring.

Ehrhart (2017) also describes a field test where a bridge was dynamically monitored. Here the natural features of two bridges, the *Augartensteg* and *Pongratz-Moore-Steg* (both located in Graz), were observed. The main goal of this experiment was to evaluate the suitability of inbuilt cameras of state-of-the-art IATSs and if natural features are sufficient enough to perform dynamic deformation monitoring.

To do so, videos for the *Augartensteg* were recored at 10 fps and 320x240 px using a Leica MS50,

for the *Pongratz-Moore-Steg* at 30 fps and 640x480 px using a Leica MS60, whereby both times the instruments were about 30 m away from the construction. The results gained from applying image analysis tools on the raw image data were compared to measurements of a state-of-the-art RTS and accelerometer measurements. It yielded for all approaches that not only the amplitude of bridge responses corresponded, but also the natural oscillation frequency of the bridges was retraced. As a consequence the field tests not only showed that a state-of-the-art IATS is suitable for static and dynamic monitoring purposes, but also achieved better accuracy compared to conventional RTSs and prisms (Ehrhart, 2017, pp.72-73).

3 Digital images

Taking images is an invention, which has been part of humanity for a long time. As a consequence of digitalization also photography and all its disciplines developed. However there are distinctive differences in just taking pictures or using pictures as a medium for metrological operations (Burger and Burge, 2016, p.1). For a long time, image processing or rather working with images on a computer was a profession, which only a very small group of people was able to perform. On the one hand, it was important to possess the right equipment and on the other hand to have the knowledge concerning image processing and editing. For a while this combination was only found in research laboratories due to their resources. However nowadays the community has grown and is able to perform efficient and high-quality work concerning image processing, as hardware evolved to be more powerful and freely available at a lower cost. As a consequence, it is necessary to distinguish between the terms of image editing and image processing.

3.1 Image editing and digital image processing

Image editing refers to the manipulation of digital images based on already existing programs and software packages. On the other hand image processing describes the conception, design, and development of digital image programs (Burger and Burge, 2016, p.2). The research or work required indicates if image editing or digital image processing is required. In general, image analysis needs efficient, reliable and robust routines especially when it comes to the extraction of meaningful information. Extraction means finding unique spots or objects in an image, which will allow reliable conclusions for example about displacement or changes of motion. A powerful tool to achieve image analysis is computer vision (CV). CV handles the problem of engineering artificial visual systems. It is capable of detecting, describing and interpreting the real captured world. Covered topics are scene understanding, object recognition, image comparing, 2D and 3D correlation, motion interpretation and robotic manipulation of objects in a scene. CV has its origin in the development of artificial intelligence (AI) and therefore often AI methods were invented to tackle specific issues in CV (Burger and Burge, 2016, p.3).

In this thesis the image analysis is based on the Open Source Computer Vision Library (OpenCV), which is a software library for CV and machine learning. It provides tools to solve different issues when working with CV, such as simple image editing (e.g. cropping) and high-level algorithms like face detection, image matching etc. (Pulli et al., 2012, p.63).

3.2 Digital image acquisition

In literature the acquisition of images differs and is rather complicated to explain in its entirety. Therefore, only the basic method will be described by the means of the so called pinhole camera. A short explanation will be given to describe the transformation of an analog light signal to a digital image (Burger and Burge, 2016, pp.4-8).

3.2.1   The pinhole camera

The pinhole camera model is the basic method for describing the image taking process and was first developed in the 13th century. It still can be taken to explain the main optical components of any camera system, which in case of the pinhole camera is a closed box featuring a small aperture. Through this opening, light enters and forms an image on the opposing inner surface, however the result is smaller and inverted, as shown in figure 3.1. O defines the origin of a three dimensional
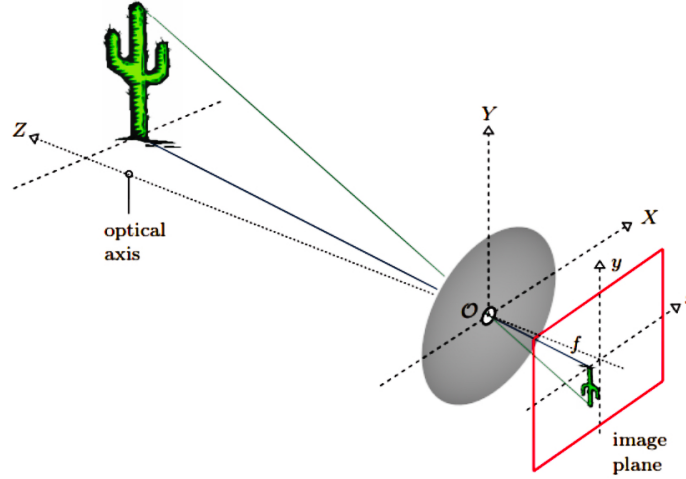
Figure 3.1: Schematic representation of the pinhole camera (Burger and Burge, 2016, p.6)

coordinate system (X, Y, Z) and the optical axis, which runs through the pinhole and further is perpendicular to the image plane. There is a second two dimensional coordinate system defined by x and y, which describe the projection points on the image plane. The last unknown is the focal length f being the distance between the opening O and the image plane and defines the scale of the projection.

Based on these parameters it is possible to describe the mathematical relation between the real and projected object. Assuming that Z is the horizontal distance from the object to the origin of the 3D coordinate system and defining Y as vertical distance to the optical axis, the height and width of the object w.r.t. to the image plane could be described as

$$
\begin{aligned}
y &= -f \cdot \frac{Y}{Z} \\
x &= -f \cdot \frac{X}{Z}.
\end{aligned}
\tag{3.1}
$$

It yields for both parameters in equation 3.1, that f is a scale parameter. Therefore, when using a wide angle lens having a small focal length, will cause a larger field of view, but the captured object will appear smaller. When increasing the focal length, the object occurs larger, however the viewing angle will get smaller. The negative sign means that the projected image is flipped (vertical & horizontal) and rotated by 180°. These relations have been known for a long time as the perspective transformation.

Is that its simple geometry is flawed, making it impractical. To achieve a suitable result to some extent, it would be necessary to decrease the opening to get a sharp image, which however automatically leads to much longer exposure times. Therefore in real applications complex optical lens systems are used, which of course perform better under varying conditions. Like shown in figure 3.2, the simple change from the pinhole to a perfectly symmetric and infinitely thin glass lens solves the problem. Here the light rays would be bundled and result in a picture caught at the virtual image plane. However, this model does not cover the complexity of lens distortions or refraction properties of different wave lengths.
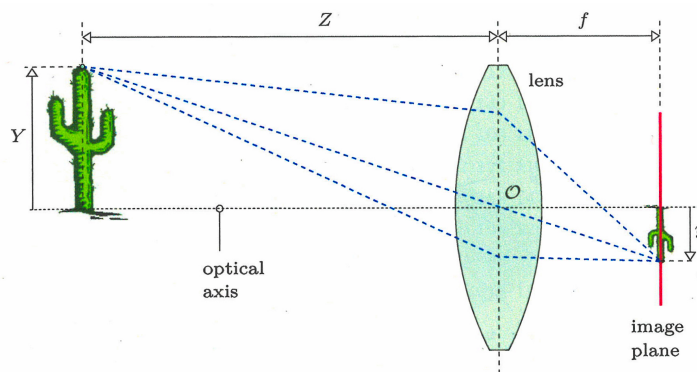
Figure 3.2: Schematic representation of a thin lens system (Burger and Burge, 2016, p.7)

3.2.2   Transformation of a scenery into a digital image

Having explained the simple method of catching a scene, it is necessary to transform what is projected on the image plane into a digital image. The idea is to use the distributed light energy for conversion. This operation requires some steps: (1) the spatial sampling of the light distribution, (2) temporal sampling of the light distribution, and (3) quantification as digital numbers.

Performing a spatial sampling of the continuous light distribution depends on the camera's sensor architecture. However, normally the sensor elements are arranged as an array on the sensor plane. Based on the measured time intervals (temporal sampling), the sensor elements will be stimulated by the incoming light energy and charged, e.g. similar to a charged-coupled device (CCD) sensor. The last step is the conversion of the analog to a (discrete) digital signal. Here, the continuous signal will be sampled based on a specific frequency and digitized as e.g. 2^8 quantification levels (grayscale values) (Bähr and Vögtle, 1991, p.24-28). The resulting digital image equals a two dimensional matrix of integers and therefore can also be formulated as a two dimensional function $I(u, v)$.

3.3   Digital image correlation and image registration or matching

Besides the common geodetic surveying methods such as levelling and tacheometry, photogrammetry metrologically quantifies information depicted in an image. Based on the knowledge gained over the years photogrammetry does not only describe the mathematical relations between the camera system

and the image itself, but has evolved over time. Nowadays virtual reality and augmented reality are one of the most attractive scopes, which both have their origins in photogrammetry. The inventions created new standards and increased the field of applications, also for geodetic purposes.

In case of performing geodetic monitoring a measured quantity is compared at different or consecutive epochs. The same principle holds for operations using digital images. The basic idea would be to compare images from different epochs, capturing the same object or situation and describing the similarity between those. For the human eye this is not a big deal, because it is sensitive to see patterns, parallelism and structures based on semantic information. However, computing changes and expressing them numerically from images is much more complicated. Especially when the system has to deal with influences like noise, quantization errors, different light conditions, shifts and rotations. Accoording to Wang et al. (2015), in CV the most common methods performing such operations are digital image correlation (DIC) and image registration or matching (IRM). The origin for DIC can be found in research fields such as surface deformations (strain or shifts). IRM is more often found in CV applications like object tracking. Therefore, it is important to know where to use each technique based on the application's requirements. In this thesis two methods for DIC and IRM are considered:

- Template Matching

- Feature Matching based on the scale-invariant feature transform (SIFT) operator

The workflow of each differs due to their functionality. The template matching works with subimages, also called *templates*, within a larger image and tries to find and track a certain in a scene over a period of time. The feature matching technique based on the SIFT operator instead tries to find reference points or rather unique spots, also called features, in a scene, defines respective descriptors (fingerprints) and, based on those, locates the points in another image. Further details can be found in the following subsections.

3.3.1   Template matching

Template matching is mainly used in DIC and therefore generally uses area-based matching. The technique applied here is also known as correlation-based method for intensity images (Burger and Burge, 2016, pp.566ff), where a reference image (template) R has to be localized in a larger image I (grayscale), which is also known as search image. Based on the pattern captured in the template, the position has to be found where the similarity between R and I is the highest. Hereby, R is shifted by the distance (r, s) expressed as

$$R_{r,s}(u, v) = R(u - r, v - s), \tag{3.2}$$

where $(r, s) \in \mathbb{Z}$ and $(u, v) \in \mathbb{N}$. In order to solve the matching problem, several issues need to be dealt with. These are, inter alia, the determination of a reasonable similarity value for approving a match and an effective search routine finding the optimal displacement. Based on the distance $d(r, s)$

it is possible to express the amount of agreement. For 2D images different distance measures are considered:

- Sum of absolute differences:

$$d_A(r, s) = \sum_{(i,j) \in R} |I(r + i, s + j) - R(i, j)| \tag{3.3}$$

- Maximum difference:

$$d_M(r, s) = \max_{(i,j) \in R} |I(r + i, s + j) - R(i, j)| \tag{3.4}$$

- Sum of squared differences:

$$d_E(r, s) = \sqrt{\sum_{(i,j) \in R} \left(I(r + i, s + j) - R(i, j) \right)^2} \tag{3.5}$$

d_E is nothing else than the Euclidean distance between two N-dimensional vectors. Based on the underlying properties and its value in statistics and optimization, the minimization of the square of d_E is used to describe the best fitting position concerning similarity between R and I. Due to the binomial theorem d_E is rewritten as

$$d_E(r, s) = \sum_{(i,j) \in R} I^2(r + i, s + j) + \sum_{(i,j) \in R} R^2(i, j) - 2 \cdot \sum_{(i,j) \in R} I(r + i, s + j) \cdot R(i, j), \tag{3.6}$$

whereas the last term equals the linear cross correlation of $I * R$, written for the boundaries given by the images

$$\sum_{i=0}^{M_R - 1} \sum_{j=0}^{N_R - 1} I(r + i, s + j) \cdot R(i, j) = \sum_{(i,j) \in R} I(r + i, s + j) \cdot R(i, j). \tag{3.7}$$

Because this computation of the cross correlation strongly depends on the intensity variations in the search image I, the normalized cross correlation is introduced to calculate the quantity $C_N(r, s)$, written as

$$C_N(r, s) = \frac{\sum_{(i,j) \in R} I(r + i, s + j) \cdot R(i, j)}{\sqrt{\sum_{(i,j) \in R} I^2(r + i, s + j)} + \sqrt{\sum_{(i,j) \in R} R^2(i, j)}} \tag{3.8}$$

Because $C_N(r, s)$ is normalized, the result based on its range [0,1] indicates the best match, when $C_N(r, s) = 1$ and $C_N(r, s) = 0$ equals no agreement between reference image R and search image I. Based on such a standardized correlation value indicating the match quality, it can be easily used to reject or accept a match position (Burger and Burge, 2016, pp.568-569).

3.3.1.1   Monitoring applications for DIC combined with other sensor systems

In the framework of getting into different methods of digital image processing, a previous task was the comparison of DIC with fibre-optic sensing. For this experiment Monsberger et al. (2018) installed a fibre optic cable used as distributed fibre optic sensor (DFOS) on a grouted steel anchor, which was bent in four steps up to a maximum of 21 mm at the top of the grouted steel anchor. Due to verification of the FOS sensor's results, DIC, as a contactless image-based remote sensing technique, is used as a further method to describe the physical change of the anchor when simulating loading phases, shown in figure 3.3. To achieve valid results using the area-based matching approach, the anchor was sprayed to have a random speckle pattern, which should allow a reliable point identification and matching. Based on the focal length (55 mm) and the distance between camera and the specimen (4,06 m), one pixel equals a size of 0,28 mm.
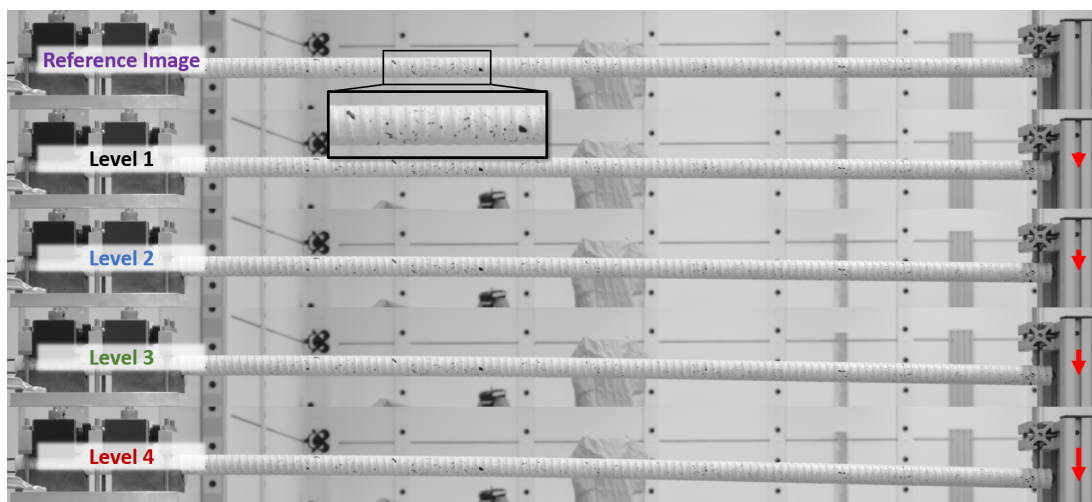
Figure 3.3: Stepwise loading of the steel anchor showing a higher bending magnitude

For the evaluation, different versions performing DIC are used for the verification of the bending characteristics of the steel anchor, introduced as

- Version 1 (#1): University of Rome Sapienza
  This version was at first stated as the derived results via DIC for this experiment. It was used for the comparison of the DFOS results by Monsberger et al. (2018). However, the results showed some deterministic effects such as a trend or rather periodic defects.

- Version 2 (#2): Graz University of Technology - routine written in Python
  This version is a self-written routine implemented in Python to improve understanding of template matching, whilst debunking periodic overlay in the results of the first version.

- Version 3 (#3): GOM Correlate
  According to GOM (2019), GOM Correlate is defined as

  > ... digital image correlation (DIC) and evaluation software for materials research and component testing.

It is used as a reference solution for the template matching results due to its professional development and capabilities.

Looking at versions #1 and #2, it is very important to be aware of the limitations using DIC. Implementing template matching, different aspects such as the pattern on the object, the search routine (grid and template size) or correlation computation have a huge impact on the likes of performance and accuracy (Gorny et al., 2013, pp. 8-9).

To achieve good results, the speckled pattern has to be high-contrast and random. There must not be any kind of periodic behaviour. Otherwise, the results will be wrong or ambiguous. Furthermore, template matching just offers a pixelwise determination of deformation. The basic implementation is not meant to achieve subpixel accuracy. Interpolation techniques have to be used to obtain a better resolution of less than a pixel. A further issue is the size of the template window. One the one hand, bigger subset sizes will lead to a more secure correlation result. On the other hand, the extent of the deformation will be summoned over a larger area of interest, which means that there is a probable loss of information. To compensate this side effect, the step width for the comparison has to be adapted. It is decisive for the metric resolution describing the deformation process along and across the object. However, minimizing the step width has a direct impact on the computation effort, which means that halving the resolutions causes a four times higher calculation time.

Bearing these limitations in mind, a basic configuration described in table 3.1 is chosen for the computation of the deformation levels. The template size equals approximately the thickness of the grouted steel anchor. A schematic visualization of the matching procedure is shown in figure 3.4. Based on the proclaimed OpenCV template matching routine, the *normalized correlation coefficient* method is used. The theoretical background for this approach is given in chapter 3.3.1.

Table 3.1: Settings for the search routine performing DIC via template matching

template size	100×100 [px×px]	28×28 [mm×mm]
step width	5 [px]	1.4 [mm]
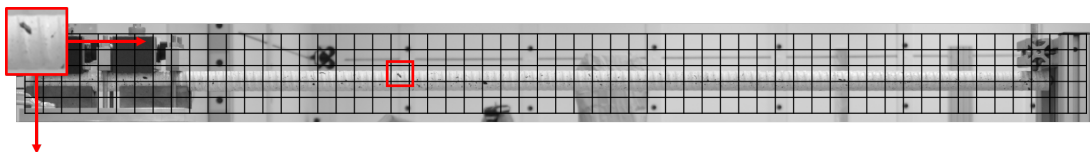
Figure 3.4: Schematic representation of the step wise image correlation showing the approximate size of a template window to compute the degree of similarity expressed by the normalized correlation coefficient

Due to the grid resolution of 5 px and based on the fact that the template matching routine does not support subpixel accuracy, the quantization problem is solved by introducing a 2D interpolation method. For the version #2 a 2D bicubic interpolation method is used (Burger and Burge, 2016, pp.553-554). In figure 3.5 the method is visualized, where first of all a 1D interpolation is performed in horizontal direction over four pixels. p_j marks the result for each line, as depicted in the left image

of figure 3.5. The vertical position is then obtained by computing one cubic interpolation over the positions p_j. Using this technique it is possible to achieve an accuracy of less than one pixel.
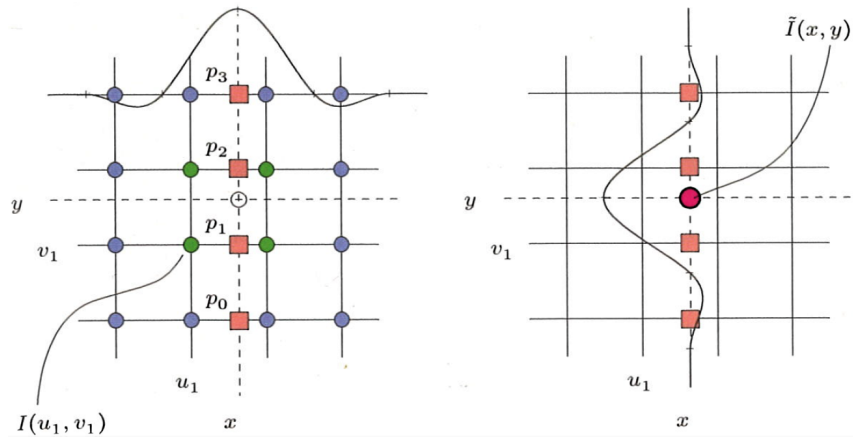
Figure 3.5: Principle of a 2D cubic interpolation for a 2D grid like an image (Burger and Burge, 2016, p.553)

Results derived by DIC concerning the detection of loading phases applied on the grouted steel anchor

Comparing the results of all routines, the horizontal component equals the x axis whereas the vertical component corresponds to the y axis. y is mainly sensible to the bending motion of the steel anchor. As shown in figure 3.7 on the left side, the displacement profiles of each loading step in the y component are distinctively visible. Despite this, version #2 shows quantization errors. This is due to the grid size resolution of 5 px ($\equiv 1.4$ mm). Nevertheless, the deformation amplitudes along x and y can be determined based on cubic interpolation with a sub-pixel accuracy of 0.25 px ($\equiv 0.07$ mm). Additionally, the possibility of deriving even higher sub-pixel accuracy might be achievable, but comes at the cost of a massively increased computation time.

Despite the quantization errors, there are further differences concerning the noise influencing the matching result. Solution (#2) delivers stable results due to the fact, that the template matching window is around the size of the grouted steel anchor. The other solutions show matching results that are rather noisy. A possible explanation is the use of a smaller template window or grid size steps. Furthermore, taking the solution of GOM, the detected deformation amplitudes along the horizontal and vertical component are influenced by the full surface motion like shown in figure 3.6.

Figure 3.6: Visualization of the matching results derived by GOM. Here, the whole surface profile of the grouted steel anchor is detected. Nevertheless, only one specific profile line is used as a representation for the whole bending motion.
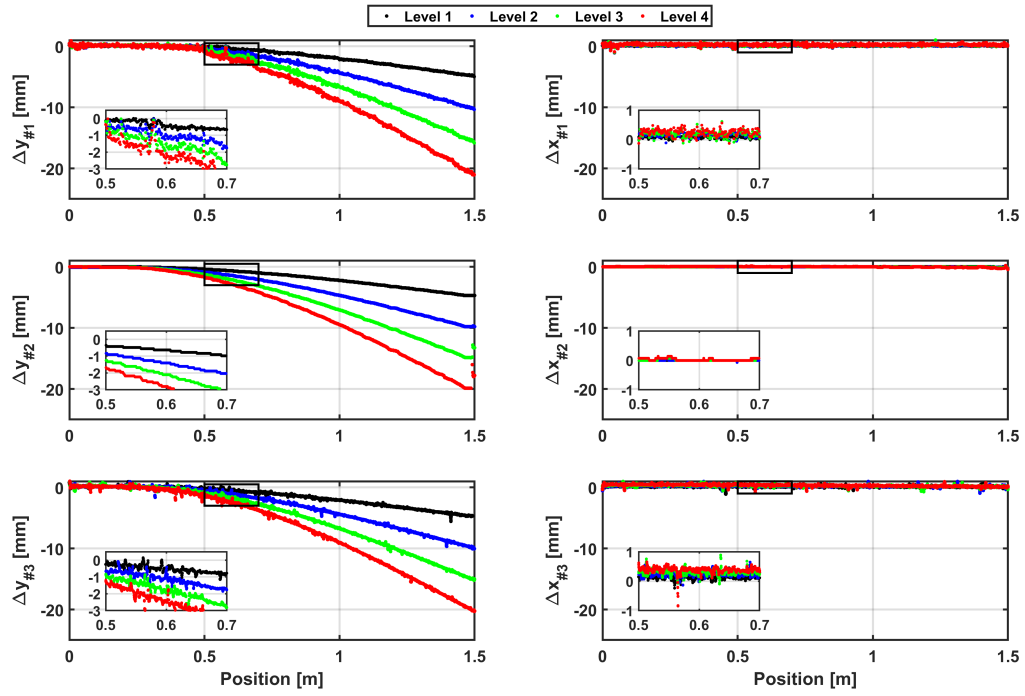
Figure 3.7: Results derived by DIC - All versions show similar deformations. #2 shows quantization issues due to the grid resolution.

Another issue, which is visible in the vertical component of version **#2**, are mismatches. They appear at the very end of the grouted steel anchor. The reason for that can be determined in the device applying the force to achieve the physical change. Here, the correlation value C_N can be taken as an indicator for the degree of similarity between the template and search image, like visualized in figure 3.8.
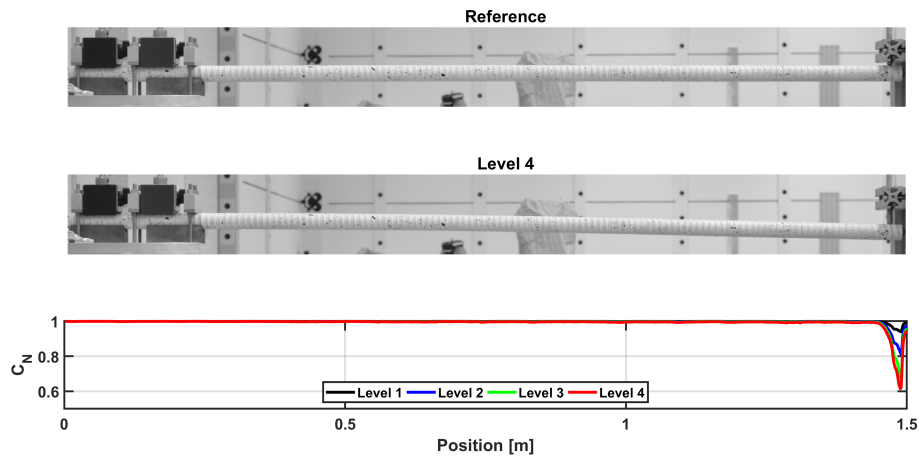
Figure 3.8: The correlation value C_N is fairly stable in respect to the changing background, which occurs due to the bending motion of the grouted steel anchor.

Finally, the differences between the separate approaches along the vertical component are depicted in

figure 3.9. In order to compare the variations, it is assumed that the solution of GOM (#3) delivers the most professional result for DIC. As already known from Monsberger et al. (2018), the matching results from version #1 show deterministic effects like trends and periodicity. These artefacts are visible in the deviations of version #3-#1 (second row in figure 3.9). Around the position of 0.5 m it seems that a bend appears in the determined differences concerning version #1. After that, the data shows another trend and small periodic jumps. These deterministic defects can be seen more clear when taking the difference from position 0.5 m up to 1.5 m, eliminating the remaining trend and computing the autocorrelation function, as shown in figure 3.10. The periodic behaviour indicated by the auto correlation value is visible especially from position 1-1.5 m.

In contrast to that, the differences between version #3 and #2 scatter around zero for each level, showing a maximum deviation of approximately 0.5 mm at the very end of the steel anchor. The maximum difference including version #1 is about 1 mm.
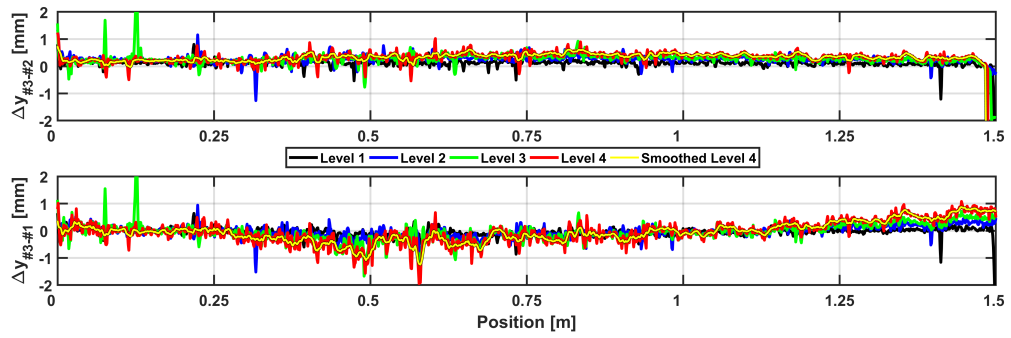
Figure 3.9: Differences between the different approaches using DIC showing the vertical deformation levels. (top: GOM (#3) minus self-written routine (#2); bottom: GOM (#3) minus DIC routine from the University of Rome Sapienza (#1))
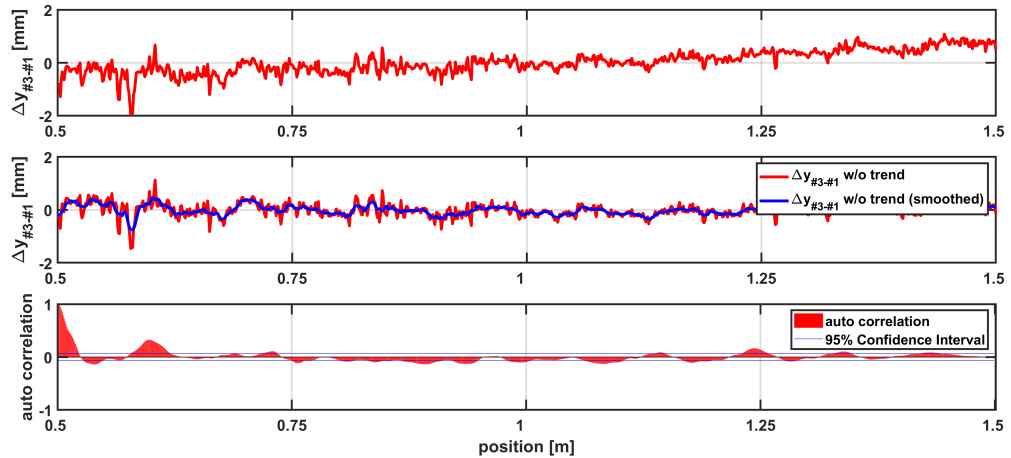
Figure 3.10: Signal processing of the differences computed on the basis of version #1. In the progress of the autocorrelation function periodic signal parts are visible.

3.3.2   Feature matching using the scale-invariant feature transform algorithm (SIFT)

As shown in the previous sections, template matching equals the approach of area-based image matching. However, image matching can also be performed using a feature-based concept. As explained in section 3.3.1.1, it is necessary to artificially mark the object of interest with a speckle pattern, sadly random patterns to suit image matching do not always occur in nature. Unlike the area-based approach, the IRM technique also works with natural patterns which occur in a scene (Wang et al., 2015, p.20).

The SIFT operator is a technique to detect local features and describe them uniquely. It was developed by Lowe (2004) and gained huge popularity in the CV community (Burger and Burge, 2016, p.609), because similar features can be located independent from specific image characteristics such as scale, resolution, illumination and rotation.

The SIFT algorithm consists of four distinctive steps to perform successfully. These are formulated as

1. The location of points of interest based on the computation of a scale space using Laplacian-of-Gaussian filters. These local extrema often occur as dark spots surrounded by brighter regions or reverse, a 2D Gaussian filter

$$G_\sigma(x,y) = \frac{1}{2\pi \cdot \sigma^2} \cdot e^{-\frac{x^2+y^2}{2\sigma^2}} \qquad (3.9)$$

and its second derivative, also known as Laplacian-of-Gaussian (LoG) and shown in figure 3.11

$$L_\sigma(x,y) = (\nabla^2 G_\sigma)(x,y) = \frac{\partial^2 G_\sigma}{\partial x^2} + \frac{\partial^2 G_\sigma}{\partial y^2}, \qquad (3.10)$$

are used to filter an image based on different scales to obtain a scale space to find scale invariant points of interest. However, to approximate the LoG kernel the scaled difference of two Gaussians (DoG) is used instead. Based on these, a multi-scaled DoG representation is computed to achieve an image pyramid, where the original image is smoothed and subsampled within different stages, also called octaves (figure 3.12). The image size can be reduced with regard to resolution (= sampling rate) not suffering from losses concerning distinctive signal information (Burger and Burge, 2016, pp. 619-623), because of the increasing scale σ.

(a) 2D Gaussian $G_\sigma(x,y)$ (b) Laplacian-of-Gaussian $L_\sigma(x,y)$
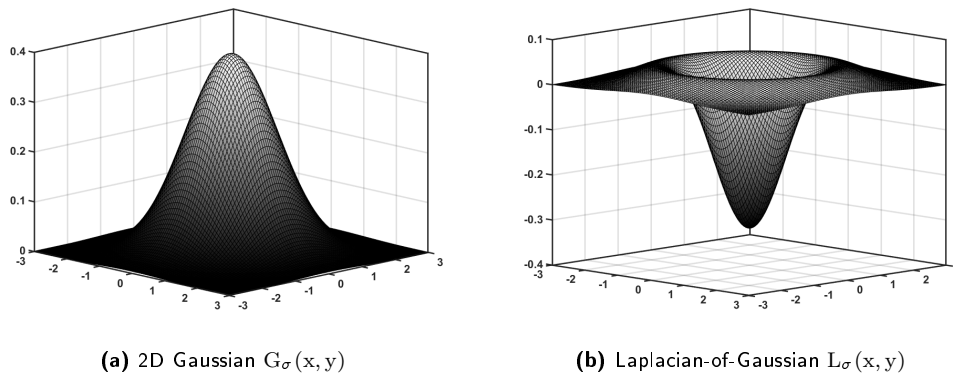
Figure 3.11: Feature detection for central regions in the picture using a center-surround operator like the 2D Gaussian.
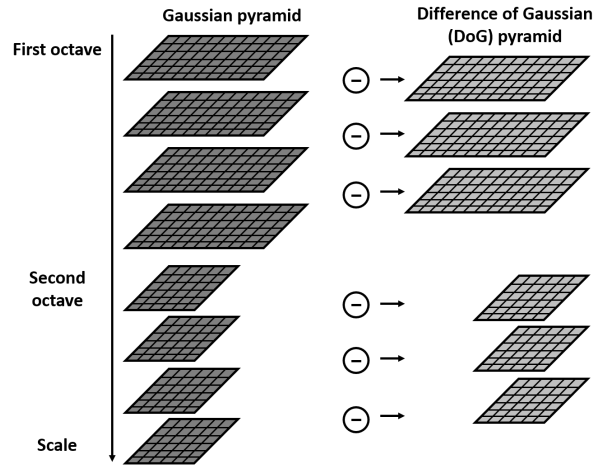
Figure 3.12: Schematic visualization of a Gaussian scale space in hierarchical order, after Lowe (2004). Each octave should at least exist of 4 scale levels

2. The selection of key points after computing the Gaussian pyramid. For this step, three operations are performed, formulated as: (1) find the local extrema based on the DoG scale space, (2) compute the exact position via a polynomial interpolation of second order, and finally (3) minimize the possibility of edge responses (Burger and Burge, 2016, pp. 630-636).
   The analysis of an interesting point at first is based on comparing one position (= one pixel) within the image pyramid with all its neighbours (26 pixel positions in a 3x3x3 box). Finding a position which is a local maxima or minima can be then described as a new 3D coordinate $\mathbf{c} = (u, v, q)$ including the pixel position and the current level q.
   Due to the goal of achieving subpixel accuracy, it is necessary to perform an interpolation based on a quadratic polynomial. This function is fitted into the local neighbourhood of the bright or dark spot, also called position refinement.
   The last step of detecting a key point is to eliminate the possibility of edge responses. Because the Gaussian filters strongly respond to any kind of edges, this could heavily influence the quality of finding similar points. Therefore to ensure an adequate repeatability and stability, an additional analysis of the local extrema is performed looking at the principal curvatures in this position. Based on the ratio between the two principal curvatures and defining distinctive thresholds, it is possible to filter edge responses.

3. uniquely describing a key point $\mathbf{k}' = (p, q, x, y)$ based on one or multiple local descriptors. To formulate a descriptor, following processes have to be involved: (1) computing the dominant orientations of the current position based on the gradient distribution, which can be derived from the Gaussian scale space, and (2) when finding a dominant orientation, to generate a corresponding SIFT descriptor (Burger and Burge, 2016, pp. 636-647).
   To do so, the gradient in the current Gaussian scale space $\mathbf{G}_{p,q}(u, v)$ (p corresponds to the octave, q to the current scale level) at the lattice position (u, v) is computed like

$$\nabla_{p,q}(u, v) = \begin{pmatrix} d_x \\ d_y \end{pmatrix} = \frac{1}{2} \begin{pmatrix} \mathbf{G}_{p,q}(u+1, v) - \mathbf{G}_{p,q}(u-1, v) \\ \mathbf{G}_{p,q}(u, v+1) - \mathbf{G}_{p,q}(u, v-1) \end{pmatrix} \qquad (3.11)$$

from which the orientation and magnitude can be deduced from, written as

$$
\begin{aligned}
\mathrm{E_{p,q}(u,v)} &= ||\nabla_{\mathrm{p,q}}(\mathrm{u,v})|| = \sqrt{\mathrm{d_x^2 + d_y^2}} \\
\varphi_{\mathrm{p,q}}(\mathrm{u,v}) &= \angle\nabla_{\mathrm{p,q}}(\mathrm{u,v}) = \tan^{-1}\left(\frac{\mathrm{d_y}}{\mathrm{d_x}}\right)
\end{aligned}
\tag{3.12}
$$

The next step is to sum up all orientations based on the corresponding weighted magnitude. This is because of a centred Gaussian window around the interrogation point, where the weight equals the detection scale (Wang et al., 2015, p.21). The final histogram contains 36 bins for classifying the dominant orientation.

After obtaining the dominant orientation for each feature point, the corresponding descriptor has to be formulated. This vector, which uniquely describes each key point based on its dominant orientation, consists of 128 bins (entries). This is because around each feature point a square region with a typical size of 4x4 is placed, where the cell size depends on the detection scale (to achieve scale invariance) and shows in the dominant orientation direction (to achieve rotation invariance). For each cell, a 8 bin histogram is defined, which summed up results in 128 entries for the descriptor vector.

4. normalizing the feature descriptor vector **f** to achieve invariance facing illumination differences (shown in equation 3.13), because any change in contrast is going to influence the gradient's magnitude (Burger and Burge, 2016, pp.645-647).

$$
\mathbf{f}(\mathrm{m}) \leftarrow \frac{1}{||\mathbf{f}||} \cdot \mathbf{f}(\mathrm{m})
\tag{3.13}
$$

After finding features in one image, the next step is about dealing with similar features in other images and matching them. There are different applications which benefit from matching equal features in images pairs, such as feature tracking, panorama stitching and matching stereo pairs. To do so, a huge database of descriptors is of advantage. Consequently, the amount of available features and the corresponding descriptors have direct impact on the reliability and efficiency of the whole SIFT matching procedure (Burger and Burge, 2016, pp.648-661).

To measure the amount of similarity between two sets of SIFT features ($\mathrm{s_1^a}$ and $\mathrm{s_1^b}$) in two images ($\mathrm{I_a}$ and $\mathrm{I_b}$) based on their descriptors is done via the computation of the distance

$$
\mathrm{d(s_i, s_j)} = ||\mathbf{f_i} - \mathbf{f_j}||,
\tag{3.14}
$$

where $\mathrm{s_i} = \langle \mathrm{x_i, y_i}, \sigma_\mathrm{i}, \varphi_\mathrm{i}, \mathbf{f_i} \rangle$ and $\mathrm{s_j} = \langle \mathrm{x_j, y_j}, \sigma_\mathrm{j}, \varphi_\mathrm{j}, \mathbf{f_j} \rangle$.

One problem, which is highly likely to occur, is that there will always be a best match for a feature, even if the corresponding counterpart does not exist, and therefore a false relation between features is established. To avoid this kind of mistake, Lowe (2004) introduced the idea of comparing the results of the distance computation of the best match with the second best based on their referring feature vectors $\mathbf{f_i}$ and $\mathbf{f_j}$. The intention of this method is that correct related features will show a small feature distance. In other words, the distance between two fitting features should be much smaller than to any other feature. However, if the best and second best match appear quite similar, the match is weak or ambiguous. One way, to describe this in mathematical terms is to compute the ratio w.r.t. to a reference descriptor $\mathrm{s_r}$ coming from the reference image, written as

$$\rho_{\mathrm{match}}(s_r, s_1, s_2) = \frac{d_{r,1}}{d_{r,2}}. \tag{3.15}$$

The range of ρ_{match} equals [0,1]. In case of a ratio close to 1, it is very likely that matching is either weak or ambiguous. On the other hand when ρ_{match} equals a small value, the matching process can be trusted and refers to the principle of nearest neighbor method. According to the implementation process, it is common to use a fast library for the approximate nearest neighbors (FLANN) algorithm. To finally get rid of the false matches one possibility is to define a global threshold for the ratio value, called ρ_{max}. According to Lowe (2004) the best value for ρ_{max} is 0.8, because around 90% of false matches and only 5% of correct matches will be discarded. As mentioned, the threshold method will not eliminate all false matches, a further method would be the random sample consensus (RANSAC), which was introduced by Fischler and Bolles (1981). Its a method widely used in CV to false positives effectively. With the help of the RANSAC algorithm it should be possible to obtain sets of features, which have valid matched counterparts. Consequently, a comparison between those features can be performed and used to determine whether their positions distinctively changed or not. Additionally, a defined region of interest may help to narrow down possible discrepancy between two images or frames.

3.4   Conclusion of digital image operations

There are various forms of image processing, as required for the research of this thesis, algorithms are the primary focus, which can clarify whether depicted scenes in an image are similar or not. Therefore, two techniques, known as DIC and IRM, are compared. Depending on the application, each of these approaches offers a slightly different outcome. The DIC approach utilizes area-based comparison. The IRM works with detected features like significant spots, corners or edges.

The DIC approach is variant concerning e.g. changes in illumination or rotation. Nevertheless, its main field of application can be found in experimental mechanics (Wang et al., 2015, p.23). As shown in section 3.3.1.1 or Burger et al. (2017), DIC meets the requirements to measure the deformation of a steel anchor or a bridge during controlled loading and unloading phases. Nevertheless, it is necessary to have random patterns applied to the object of interest. These could be natural given structures or if necessary artificially applied. However, the costs of this technique in terms of computation time and efficiency are not universally suitable. On the other hand, feature based matching like in IRM is more efficient and therefore is more used frequently in CV applications. There is no need to artificially apply a speckle pattern onto the surface of the object of interest. Additionally, changes in illumination are much better compensated when using SIFT algorithm instead of using DIC. There are different versions of SIFT, such as the speeded up robust features (SURF) algorithm, which allows even faster image analysis (Bay et al., 2008). However, when it comes to an application like landslide monitoring, the chosen image evaluation technique is SIFT due to its robust behaviour concerning illumination and rotation changes and because the evaluation procedure is not performed in real time, which compensates the need for even faster feature matching.

4 Analysis of image-based observations for static and dynamic monitoring purposes

Combining a RTS with a camera system is an innovation, which develops an already high tech surveying platform, especially when the camera is located in the optical path of the telescope. As a consequence, one of the main key advantages of an IATS is that it can be implemented as a fully contactless measurement system. Therefore, its application field is also attractive to cover the purpose of structural health monitoring (SHM), according to e.g. Ehrhart and Lienhart (2015b). Nevertheless, besides the advantages of an on-axis camera system, an IATS has to deal with certain issues when it comes to performing image-based measurements. ? introduce different aspects that deal with error sources of image-based observations, stated as

- Firstly, the derivation of image-based angle observations, where it is necessary to model the relation between the image coordinates and the necessary underlying angles of the theodolite.

- Secondly, the modelling of the image-based angle observation based on the camera based parameters, which have to determined via a calibration of the camera system.

- Thirdly, the dependency of the target type, causing the implementation of different evaluation routines, which have to be introduced to finally achieve useable image coordinates.

A further aspect discussed in this thesis covers the combination or rather separation of ATR based and image-based measurements. The reason for this consideration is the repeatability of instrument alignment when its comes to image and video recordings over longer measuring periods. Because both observation types can be used for static and dynamic monitoring purposes, the introduced measurement concept for the determination of displacements and vibrations by Ehrhart and Lienhart (2015b) is rethought based on the relations of image coordinates and angle observations introduced by ?.

4.1 Comparison of an IATS and a RTS using ATR

According to the specifications of the sensor technology used for image-based measurements (images, videos), the camera system is comparable to the common automatic target recognition technique, which most of the manufacturers implement in their instruments. Taking the ATR mode of Leica into account, image-based observations and measurements using ATR can be compared due to their basic functionality, shown in figure 4.1. As a consequence, it can be said that using an IATS corresponds to a passive ATR mode.

Summarising the advantages and disadvantages of using an IATS, it can be stated that

- + no targets have to be cumbersomely installed.
- + the pixel resolution of the sensor is better.
- - taking an image of a scenery, sufficient illumination has to be prevailed.
- - an IATS is normally much more expansive.

Automatic target recognition using total stations

RTS using ATR		IATS	
Active sensor	→ IR signal is emitted	Passive sensor	→ External illumination (e.g. sunlight)
Prism reflects IR signal	← Artificial target	Natural reflections	← Natural target
Reflected signal is detected by CMOS sensor	→ 1 px ≡ 30 cc	CMOS sensor receives light and produces an image	→ 1 px ≡ 6 cc
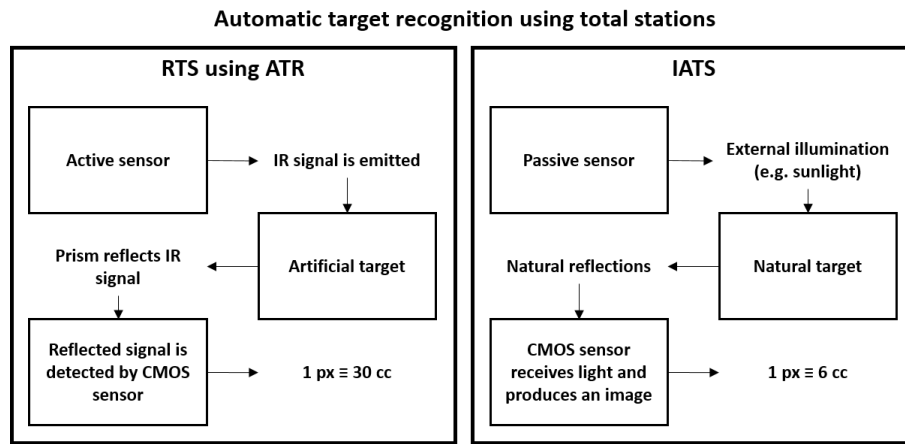
Figure 4.1: Comparison of the functionality of a RTS using ATR and an IATS taking pictures/videos (resolution given for Leica MultiStations e.g. Leica MS60)

4.2 Deformation monitoring using combined image- and ATR based measurements

Performing measurements based on images and videos, the recording depends on the framed scenery, which is defined by the telescope's orientation and the field of view. Therefore, the angle computation based on the recorded images or videos depends on how well the telescope position is known. Different aspects have to be considered when monitoring with automatic target recognition methods:

- The position refinement of the telescope is first of all based on predefined steering angles.

- After introducing the steering angles, the engine drive of the used IATS aligns the telescope, however this procedure cannot be performed precisely. Furthermore, the process depends on the previous orientation of the instrument and braking process of the motorization.

- When using the ATR mode, the sight axis of the instrument is mathematically corrected into the centre of the prism, if the ATR deviations are below 5 mgon. Therefore, there will be a difference between the recorded angles and the actual orientation of camera system, which is located in the optical path of the telescope, defined as OAC.

Taking the 5 mgon as a threshold, the referring deviations computed into metric deformation are listed in table 4.1. Like in section 2.2, **?** introduces a scale factor between angle and pixel resolution written as $\alpha_{\mathrm{px}} = 1\mathrm{px} \equiv 0.6\mathrm{mgon}$. This relation can be used for rough angle accuracy estimations. As a consequence, 5 mgon would refer to approximately 8-9 pixels. Therefore, when the telescope is aligned based on this threshold and only the image-based observations are available, the pixel differences would wrongly indicate a significant rigid body motion. Figure 4.2 visualizes this below.

Table 4.1: Metric deformation based on ATR threshold of 5 mgon

Distance [m]	Deformation [mm]
50	4.2
100	8.3
200	16.7
300	25.0
400	33.3
500	41.7
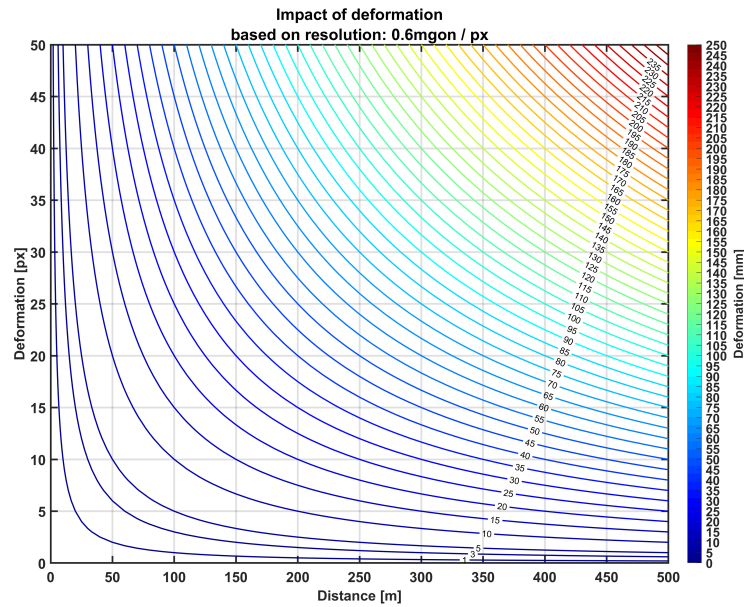
Figure 4.2: Computation of metric deformation based on the scale factor α_{px}

Stating this issue, the combination of image-based observations and ATR based position refinement have to be handled with caution. The problem is that the corrections caused by the ATR are not recorded. Furthermore, the variations of the telescope's alignment due to the motors positional setting accuracy are also included. These components influence an optimally repeatable position alignment of the telescope for each epoch or even each face measurement. A schematic visualization can be found in figure 4.3, where the idea behind the position adjustment is depicted.
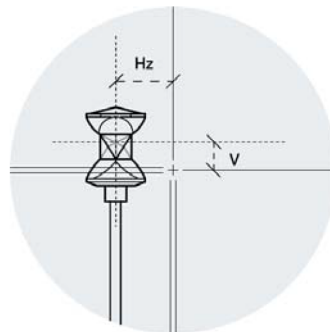
Figure 4.3: Visualization of the ATR deviations seen through the ocular of a instrument (Leica-Geosystems, 2008, p.6)

5 Analysis of ATR concerning precision and temperature dependency

A further scope, when performing static or dynamic deformation monitoring is the use of ATR, like presented in Lienhart et al. (2016). This technique was already used during the entire measurement campaign at Wald am Schoberpass and guarantees a precision for angle measurements of 3 cc (Leica-Geosystems, 2015a, p.8). As a consequence, it is implemented in automatically performed geodetic monitoring applications in general. Nevertheless, variations in the measurement data can occur causing deviations which could be equated with a displacement or deformation process. Rephrasing, an automatic warning system might react to those changes and triggers an alert. Like at Wald am Schoberpass, the angle data shows variations, which, compared to the measurement precision, are significantly high. Daily variations of 15-20 cc are equal to approximately 10-13 mm. Seen as a rigid body motion, this seemingly existing deformation could cause an evacuation of a building or the closure of a construction site.

Nonetheless, apart from the possibility of false positives in a data set, ATR simplifies a measurement procedure because of its automatic target aiming process (Leica-Geosystems, 2008). Still the question appears, how valid the technique works when used in the context of monitoring applications. Therefore, a measurement run is performed to determine the quality of ATR when enduring significant changes in ambient meteorological conditions like temperature. Based on this field experiment, the reliability is evaluated and if e.g. distinctive requirements for 3D point determination can be fulfilled. Furthermore, an indicator model based on the ATR's measurement noise is introduced to handle possible variations which could be misinterpreted as deformation.

5.1 Setup of the experiment concerning ATR's behaviour

The field test was performed on the institute's roof at Steyrergasse 30 (Campus Neue Technik, Graz University of Technology (TU Graz)). Here, a network of reference points distributed over the whole campus is available equipped with different target types like prisms or target marks. Precisely determined surveying pillars by Fleckl (2006) can be used for the installation of total stations. As shown in figure 5.1 six targets were used for the long-term evaluation of the ATR's functionality. As a measuring instrument, the Leica TS15 was used due to the research performed by Lienhart et al. (2016). The instrument's specifications is listed in section 2.3 in table 2.5.

The measurement routine shown in figure 5.2 is based on a self-written software using the GeoCOM protocol. A serial connection between the used PC and the Leica TS15 was established. The communication was based on three different serial cables and an USB converter, because of the local limitations. The downside of using these types of adapters is that the measurement frequency is affected (Lienhart et al., 2016, p.4). Nevertheless, the communication setup shown in figure 5.3 provided a stable connection between the PC and the Leica TS15.

The measurement routine in figure 5.2 was used for both static and dynamic ATR measurements.

Based on the gained knowledge of Lienhart et al. (2016) different GeoCOM requests were implemented to obtain useful data. Consequently, only during the static measurements a distance measurement was performed.

Figure 5.1: Overview of target setup, which were included during the static and dynamic ATR measurements
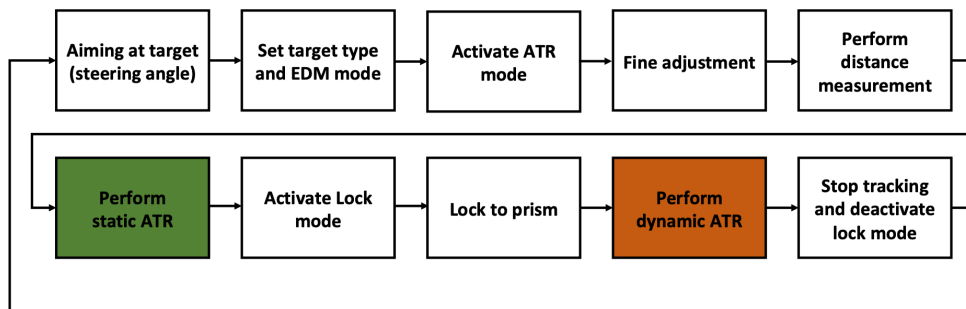
Figure 5.2: Overview of the implemented measurement procedure including static and dynamic ATR measurements
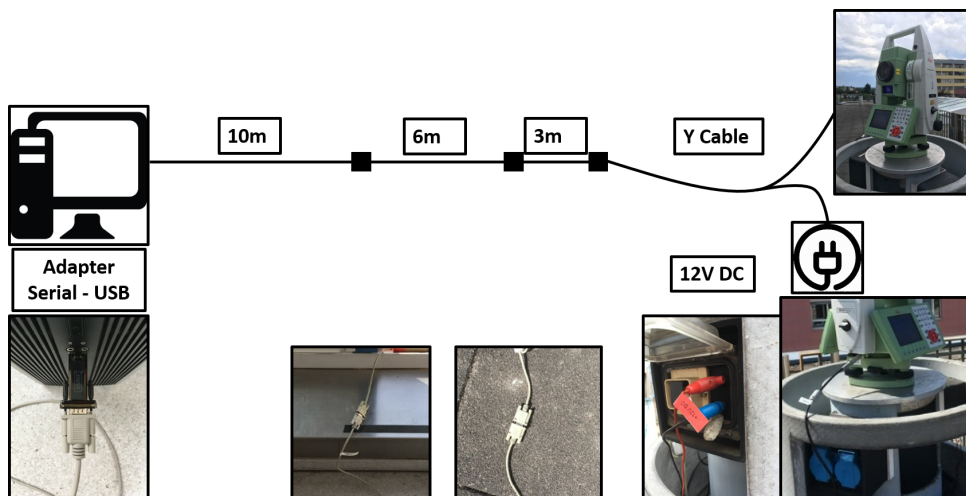
Figure 5.3: Schematic of the network connection for static and dynamic ATR measurements

5.2 Theoretical background of an ATR angle measurement

Assuming that none of the measured targets sustain deformation, the main influential components should be the setup point of the Leica TS15, the instrument itself or the air fluctuations along the measurement path (Lienhart, 2017b). Consequently, the different components affecting the angle measurement have to be discussed. Angle readings without taking refraction into account look like this:

$$\text{Hz} = \text{Hz}_{\text{encoder}} + \text{ATR}_{\text{Hz}} + \text{f}(\epsilon_{\text{coll}}) + \text{f}(\epsilon_{\text{tilt}}) + \text{f}(\alpha_{\text{across}}) \tag{5.1}$$

$$\text{V} = \text{V}_{\text{encoder}} + \text{ATR}_{\text{V}} + \epsilon_{\text{index}} + \alpha_{\text{along}}, \tag{5.2}$$

where

$$\text{f}(\epsilon_{\text{coll}}) = \frac{\epsilon_{\text{coll}}}{\sin(\text{V})} \tag{5.3}$$

$$\text{f}(\epsilon_{\text{tilt}}) = \epsilon_{\text{tilt}}\cot(\text{V}) \tag{5.4}$$

$$\text{f}(\alpha_{\text{across}}) = \alpha_{\text{across}}\cot(\text{V}). \tag{5.5}$$

These terms refer to the collimation error ϵ_{coll}, tilt axis error ϵ_{tilt} and the tilt sensor error α_{across}. The same applies to the angle readings considering the influence of refraction, written like

$$\text{Hz} = \text{Hz}_{\text{encoder}} + \text{ATR}_{\text{Hz}} + \text{f}(\epsilon_{\text{coll}}) + \text{f}(\epsilon_{\text{tilt}}) + \text{f}(\alpha_{\text{across}}) + \delta_{\text{Hz}} \tag{5.6}$$

$$\text{V} = \text{V}_{\text{encoder}} + \text{ATR}_{\text{V}} + \epsilon_{\text{index}} + \alpha_{\text{along}} + \delta_{\text{V}}. \tag{5.7}$$

Nevertheless, when computing the average of the angle readings in both faces, most of the terms will disappear. Rewriting equations 5.6 and 5.7, the terms of the ATR deviation and the refraction angle remain:

$$\text{Hz}^* = \text{Hz}_{\text{Av.}} + \text{ATR}_{\text{Hz (remaining error)}} + \delta_{\text{Hz}} \tag{5.8}$$

$$\text{V}^* = \text{V}_{\text{Av.}} + \text{ATR}_{\text{V (remaining error)}} + \delta_{\text{V}}. \tag{5.9}$$

Therefore, when computing the face averages, only the ATR and the refraction should still have an impact on the measurement.

5.3 Atmospheric influences on the Leica TS15

The main impact is temperature and its daily cycles over a long period. Therefore, table 5.1 gives an overview of the key values and characteristics during the whole period. Furthermore, figure 5.4 shows how the ambient temperature influences the internal temperature of the TS15. Especially in warmer environments, the Leica TS15 has to deal with an internal temperature of nearly 45°C. The ambient temperature was measured by a local meteo station installed at the top of the institute's roof. The internal temperature, which was extracted via the GeoCOM protocol refers to the motherboard

temperature.

The information which can be taken from the comparison of internal and ambient temperature in figure 5.4 is that there is a hysteresis effect. The warming and cooling phases of the Leica TS15 strongly correspond to daily cycle of temperature measurements, albeit with a small delay. The main reason is missing sun protection, such as a sunchade, resutling in a fairly heated up main board.

Table 5.1: Key values of the ambient and internal temperature performing the ATR test measurements. The Leica TS15 was not shadowed during the field test, which does not meet the perfect measurement setup, however guarantees extreme situations for the surveying instrument.

	max. T [°C]	min. T [°C]	av. T [°C]
Ambient temperature	32.9	18.6	25.2
Internal temperature of Leica TS15	43.8	22.4	33.0
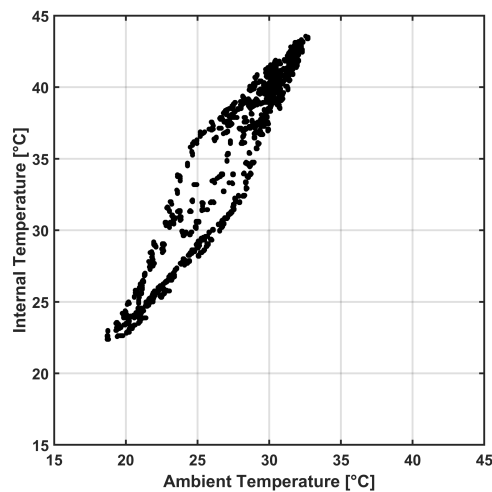
Figure 5.4: Internal temperature vs. ambient temperature

5.4 Obtained results from static ATR measurements

The next section will present the outcomes for each observation quantity measured by a total station using ATR from Leica. As explained in section 5.2, the angle measurements should indicate different influences. As a basis for the computations the epoch wise measurements are used. During each epoch three complete sets of measurements are performed. In the end, metric deformations are calculated to draw conclusions concerning the quality of the ATR measurements.

5.4.1 Angle measurements

The static ATR measurements contain the angular measurements Hz end V, the distance measurement SD and the readings of the tilt compensator along (Li) and across (Ci) the instruments axis. All observations are used for a proper analysis of the ATR functionality. As mentioned in the chapter 5.2 before, the angular measurements include different components. Measuring angles in one face, instrumental errors affect the angular reading. When looking at the results for Hz and V relating to

target 101, each face observation of both quantities shows strong correspondence to daily temperature cycle.

The results for Hz show that the single face measurements are similarly effected (figure 5.5). Therefore, the face average shows the same progress, visualized as white line in figure 5.5. Comparing all targets, the observations of Hz show for each target the same behaviour (figure 5.6 top). By reducing the horizontal angle measurements to the first measured target of each set, the systematic impact can be eliminated. The remaining deviations (figure 5.6 bottom) show no systematics any more and are considered as pure measurement noise. Calculating the standard deviation results in $\pm 10\,cc$ which equals $\pm 3\sigma$.

On the other hand, V shows a contrary behaviour for both faces (figure 5.7). This difference is mainly caused by the index error $\epsilon_{\mathrm{index}}$. This quantity shows variations of up to $70\,cc$, especially during the hottest parts of the day. Nevertheless, its influence should be eliminated when calculating the face average. The remaining parts are therefore classified as residuals errors, which could be caused as follows:

- The Leica TS15 suffered from expansion effects of the inner components, because of the missing sunshade. As a consequence, the inbuilt sensor systems are also affected.

- The refraction and its referring changes along the measurement path cause additional artefacts.

- Although the face average should be free from instrumental errors, these might have changed between the measurements in each face.

Additionally, the differences in V show different behaviours w.r.t. the target, shown in figure 5.8. Here, the targets 104 and 105 have to be highlighted. A possible explanation for target 104 might be that the prism is installed near to the ventilation system of the canteen. The ventilation system causes significant atmospheric disturbance even at night.

On the other hand, target 105 clearly shows an opposite progress compared to e.g. target 101. Comparing the transition from day to night, the referring signs of ΔV differ. Again, the location of the target is taken into account, because target 105 is located on the same roof such as the Leica TS15. Therefore, the atmospheric conditions for the LOS changes compared to the measurements of the other targets. On the roof top a continuous homogenous terrain exists. This is not true for the other measurement sightings. A possible consequence might be that the orientation of the temperature gradient along the LOS from the setup to the target point changes compared to having heterogeneous underground, such as house canyons and vegetated areas. Having different curved visual lines might have an impact on the sign of the ATR deviations, which finally remain visible when computing the differences of V.
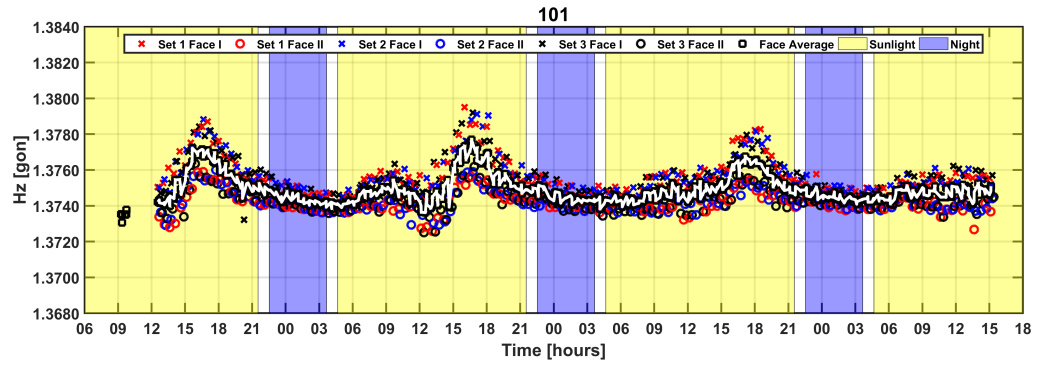
Figure 5.5: Derived values for Hz from GeoCOM for target 101 (ATR test measurement)
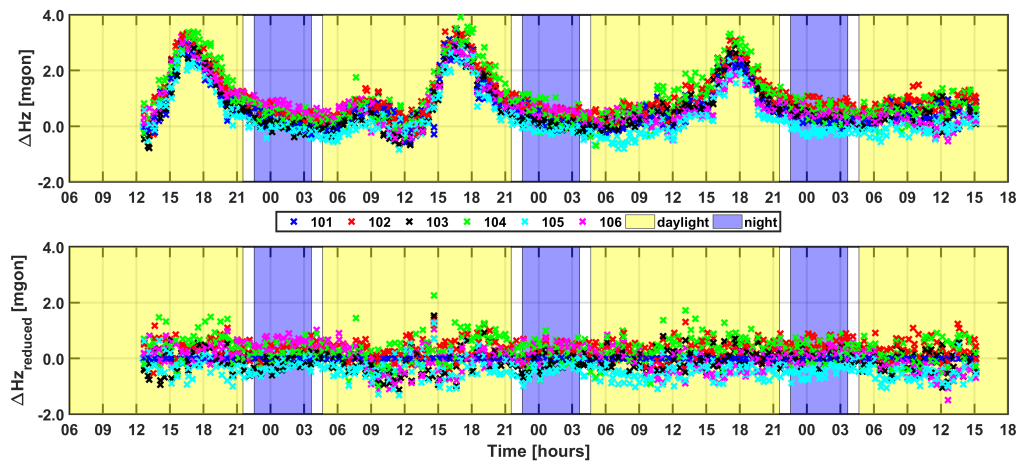
Figure 5.6: The systematic effects of Hz can be eliminated when reducing it to the first target of each set measurement.
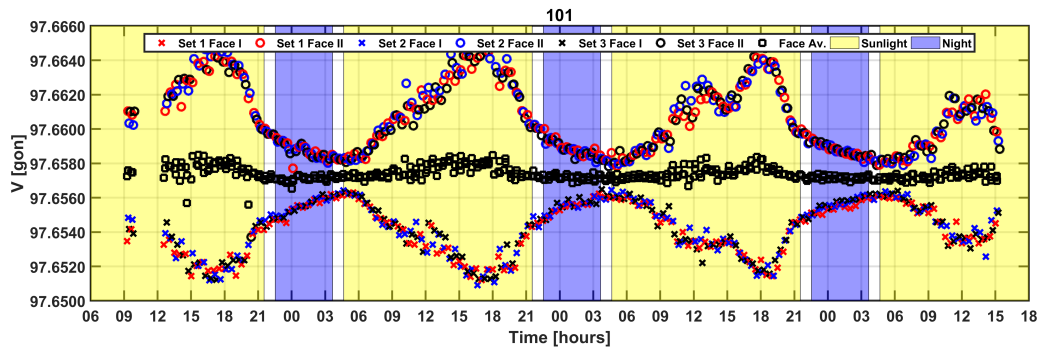
Figure 5.7: Derived values for V from GeoCOM for target 101 (ATR test measurement)
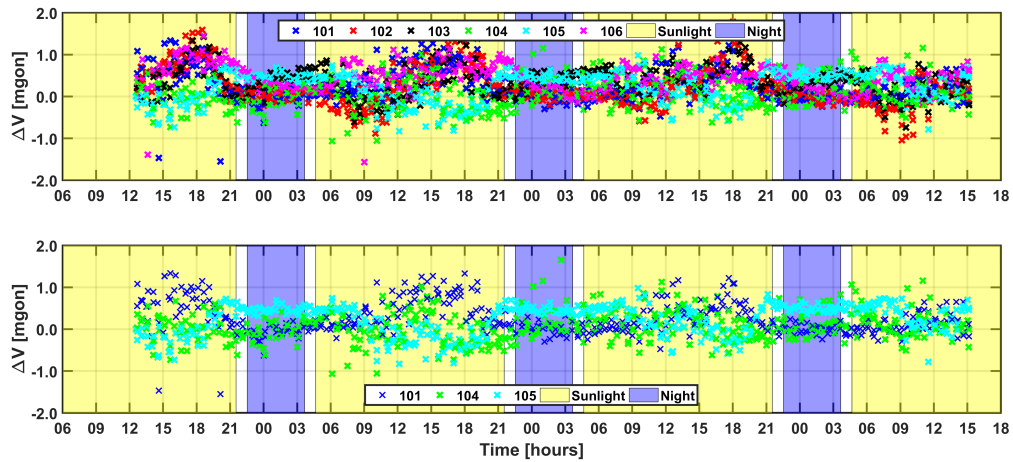
Figure 5.8: The differences in V show a different behaviour w.r.t. the target. Especially targets 104 and 105 show contrary deviations.

The next results displayed in figure 5.9 show the dependency of the differences in both components Hz and V, because the deviations strongly correspond to the temperature's cycle throughout the day. Here some interesting behaviour can be extracted. It yields for Hz that the deviations are distance independent. As a consequence, the main component causing the deviations has to be the instrument itself. It also seems that when reaching an internal temperature of 35°C the angle readings suffer from a systematic effect. This might be because of the warming and cooling phases until the motherboard cools to under 35°C. Comparing these findings with the obtained comparison of ΔV, again the sudden change after reaching the benchmark of 35°C is clearly visible. However, here the location of the targets seems to effect the sign of the deviations. Again, the target 105 stands out due to its opposite behaviour. Target 104 seems to have more scattered deviations in ΔHz and ΔV, however this spread can be traced back to the ventilation system of the canteen of the campus area, which is very near o the installed prism.

(a) ΔHz vs. internal temperature
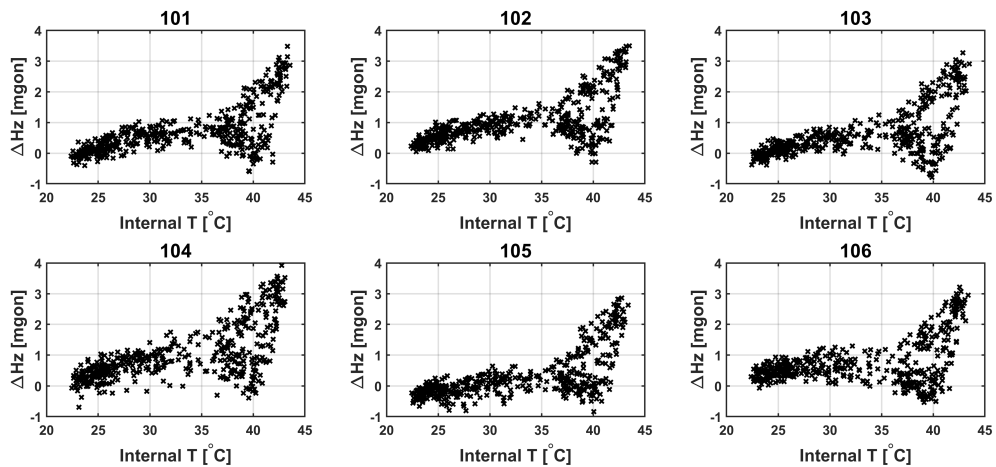
(b) ΔV vs. internal temperature
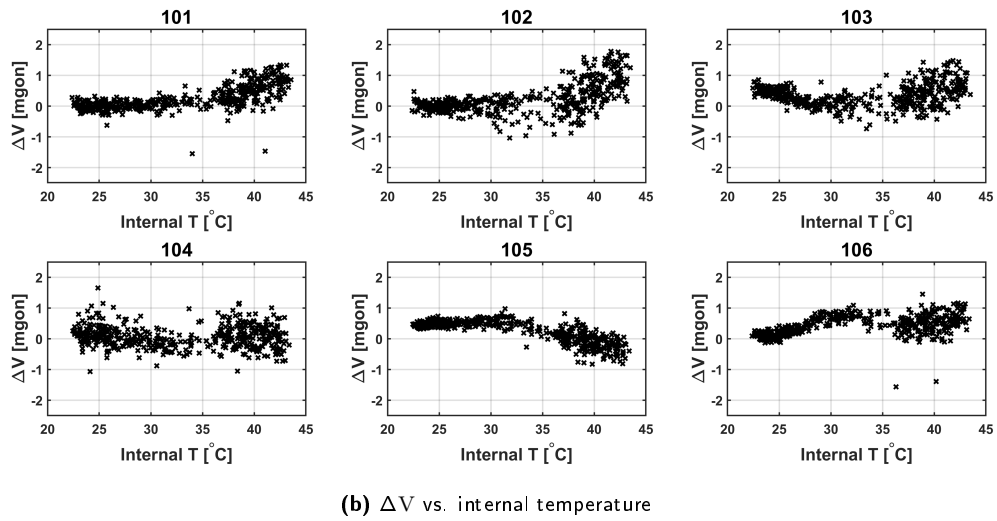
Figure 5.9: Comparing the deviations of Hz and V to the change of the internal Temperature of the Leica TS15 (ATR test measurement)

5.4.2   Inclination measurements

So far the presented results are all based on the fact, that each angle observation is corrected by the tilt compensator. V, because it refers to the plumb line, it is corrected by the longitudinal inclination. Similar to the angle measurements, the tilt readings in each face also correlate to the temperature change, which means that the installation setup of the instrument is not stable and shows a motion. However, the long-term behaviour of the zero-point error indicates for both axes that there is no systematic effect like a drift influencing the tilt compensator. This can be seen in figure 5.10a-b. Computing the absolute inclination of Ci and Li in north direction for the second day (figure 5.11), a very distinctive east-west alignment is visible, which indicates the daily motion of the sun.
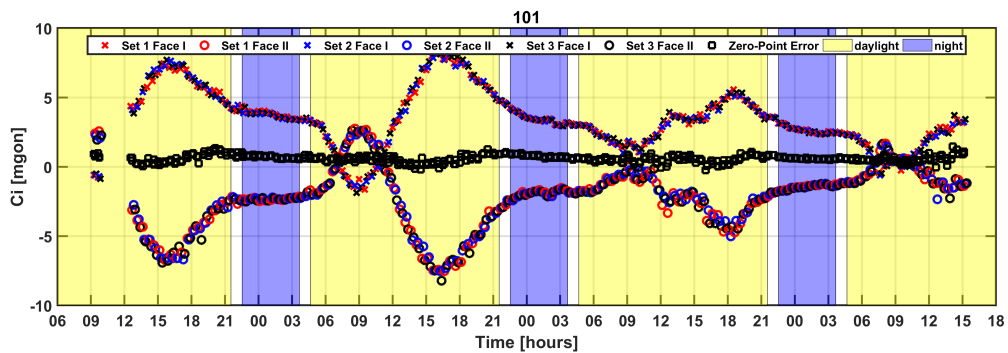
(a) Derived values for Ci from GeoCOM for target 101

(b) Derived values for Li from GeoCOM for target 101
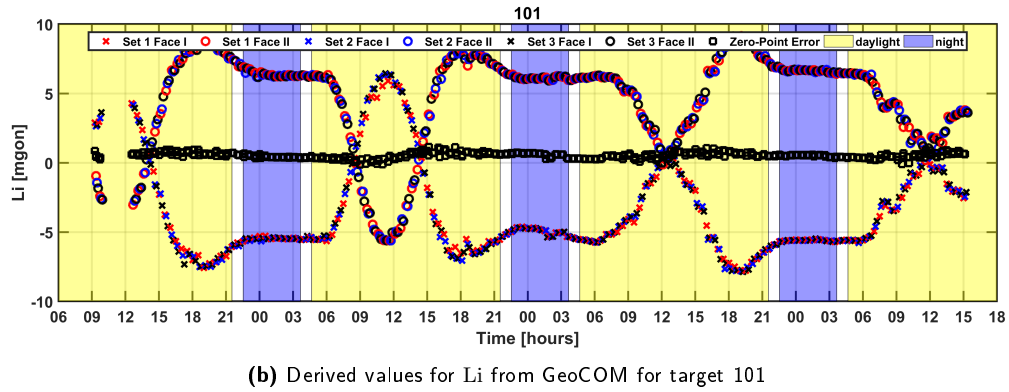
Figure 5.10: The tilt compensator's readings in each face and the referring zero point error in both axis
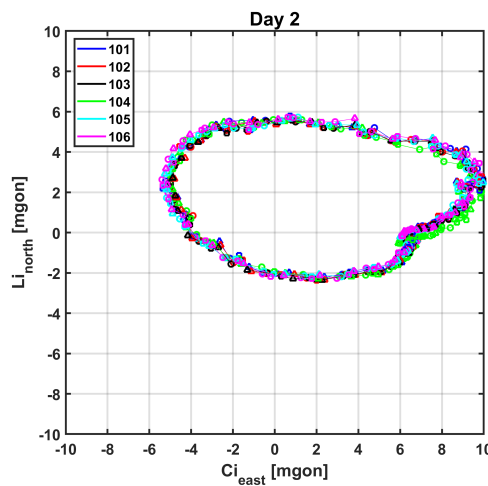
Figure 5.11: The behaviour of the absolute inclinations aligned in north direction prove that the tilt compensator's behaviour depends on the motion of the sun

5.4.3 Distance measurements

The distance measurements for the ATR test measurements were all performed using a Leica TS15 standard profile. The single EDM mode was used aiming at standard prisms which all have an offset of -34 mm. Normally, the distance measurement would have a huge impact on the communication performance of the GeoCOM protocol concerning the data transfer rate. Since static measurements are performed, the lower frequency described by Lienhart et al. (2016) is not of particular interest. Having a look at the raw readings it appears that the first measurement epochs have a huge offset compared with the remaining data (figure 5.12a). This issue was caused by a spontaneous missing data transfer between the PC and the Leica TS15. After adapting the USB converter to again obtain a serial connection, the communication status was rebuilt. However, because of this offset the data recorded in the first two epochs is not going to be part of further computations like coordinates. According to Leica-Geosystems (2019b) a meteorological correction has to be computed to obtain correct distances. Adapting these corrections should yield a faultless slope distance for further computations.

After taking the meteorological correction term into account, the corrections for target 101 are about

4 to 7 mm, which finally eliminate the atmospheric effect on the recorded slope distances SD (figure 5.12b). Similar to the results of Hz and V the computed face averages still show variations of over 1 mm especially during the warmer stages of the day (figure 5.12c). Because this applies for every measured target, again the deviations in dependency of the internal temperature of the Leica TS15 are visualized. Here, all 6 measured points show the same behaviour (figure 5.13). The differences, being measured from 22 to 35 °C, show a positive drift, whereas after passing the benchmark of 35 °C the deviations go the opposite way. Based on its longer distance, the target 101 shows a larger scattering than e.g. target 106. As a consequence of the obtained data, the distances measured by the instrument dealing with an internal temperature up to a maximum of 35 °C will appear longer, however when exceeding 35 °C the distances will be measured a little bit shorter. Again a possible explanation might be that a physical issue due to the expand of single components in the instrument might causes this effect. Due to internal strain a change of the laser beam's run time or rather of the measured fractional phase appears.

(a) Slope distance

(b) Meteorological distance correction

(c) Corrected slope distance
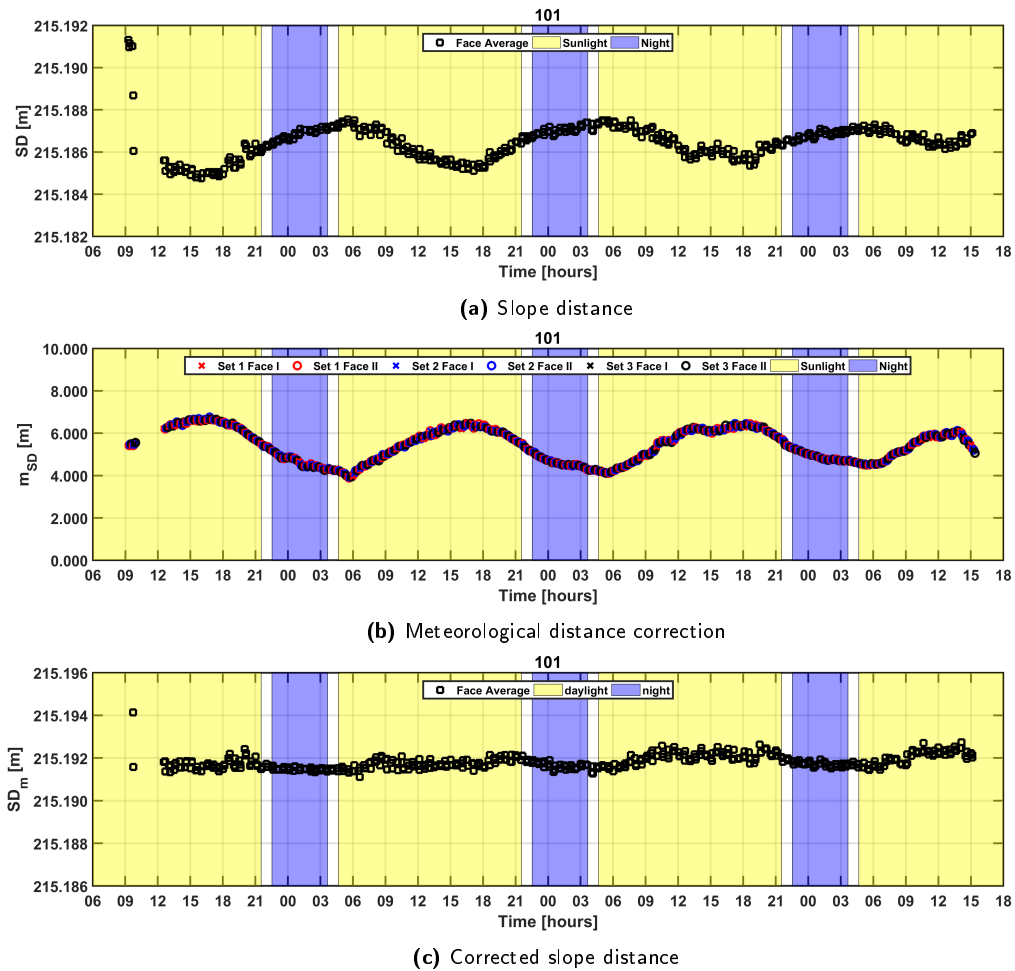
Figure 5.12: Computed meteorological distance correction adapted onto the measured slope distance to target 101
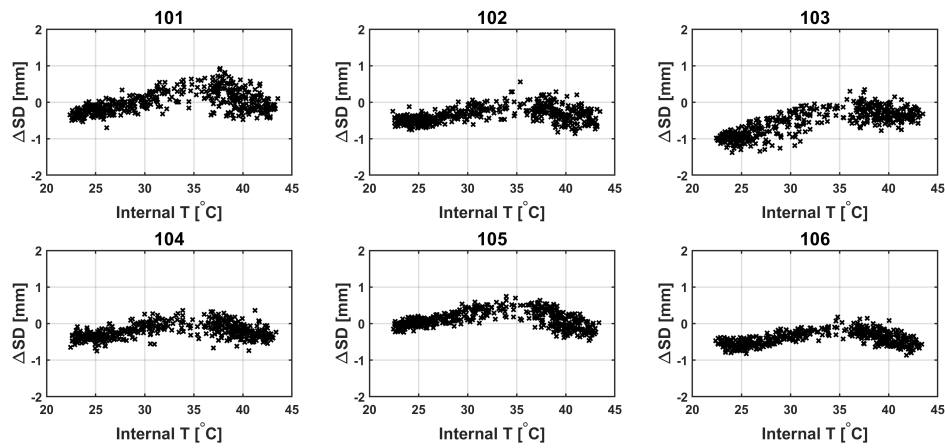
Figure 5.13: Computed deviations of the slope distance SD in dependency of the internal temperature

5.4.4 Point motion deviations

Based on the results derived for the different computations for Hz, V and SD, the motion of all targets is computed. It can be assumed that none of the targets should show a distinctive motion due to the fact that the used prisms are situated on stable buildings. A target's motion is described via the change along the LOS, across the LOS and the altitude difference between the setup point and its location. The change along the LOS correspond to the measured distance, which due to the meteorological correction should remain stable (figure 5.14a). The depicted deviations of about ± 1 mm equal the distance measurement accuracy of the Leica TS15.

In contrast to the deviations along the LOS, the change across the LOS highly correlates to the variations of Hz. As already mentioned in section 5.4.1, the face averages for each target show a similar behaviour. As a consequence, the reduction of Hz is necessary to eliminate all systematics, whereby the remaining deviations are seen as pure measurement noise. The remaining deviations of 1 mgon on 200 m, which would apply for the farthermost target 101, result in a metric deformation of approximately 3 mm, which is a significant difference to the depicted results of 1 cm in figure 5.14b, where Hz is not reduced.

The last component is the height which is computed as the altitude difference between the setup point and the current target. The main influential parameters are the distance and the vertical angle. Furthermore, a common assumption for the refraction coefficient is taken into account. Due to the behaviour of V the height corresponds to these deviations (figure 5.14c). Taking 15 cc on 200 mm, which applies for target 101, this equals approximately 5 mm referring to the maximum amplitude of Δh. Here, the sign of ΔV is very important. When the vertical angle gets smaller the height difference will increase and vice versa. Again target 105 shows a different behaviour. Furthermore, the sign of the height difference changes at around 9 o'clock in the morning, which approximately refers to the moment, where the internal temperature crosses the benchmark of 35 °C.

For a better comparison, target 105 and 106 are depicted in figure 5.15. Here, the sighting axis crosses different undergrounds. On the one hand target 105 is located on the roof (homogenous underground), on the other hand 106 is installed on the nearby building (heterogeneous underground). Again, the assumption is formulated, that the varying temperature gradient $\frac{dT}{dH}$ might have an impact. Nevertheless, it would be necessary to record the vertical change of the temperature gradient.

(a) Deviations along the LOS

(b) Deviations across the LOS

(c) Deviations of the height component
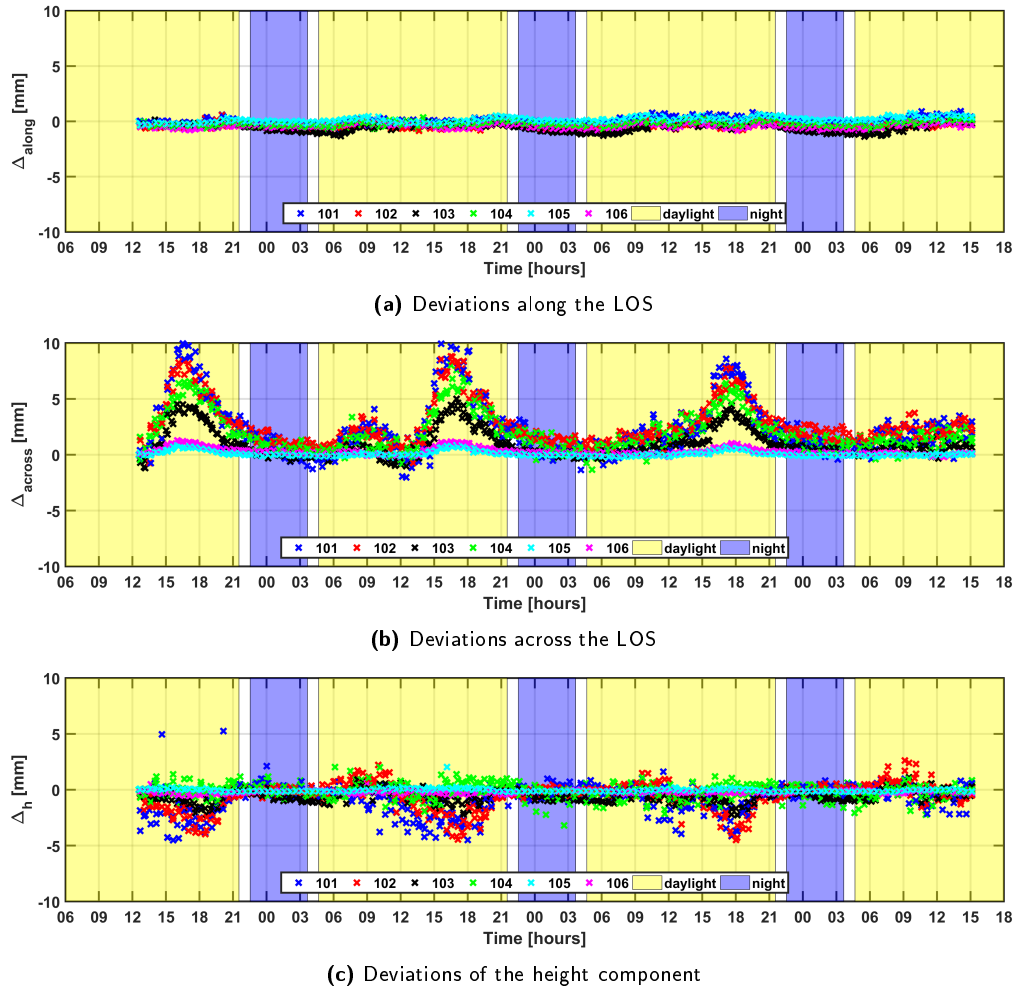
Figure 5.14: Differences of the point motion visualized for each target (101 - 106)
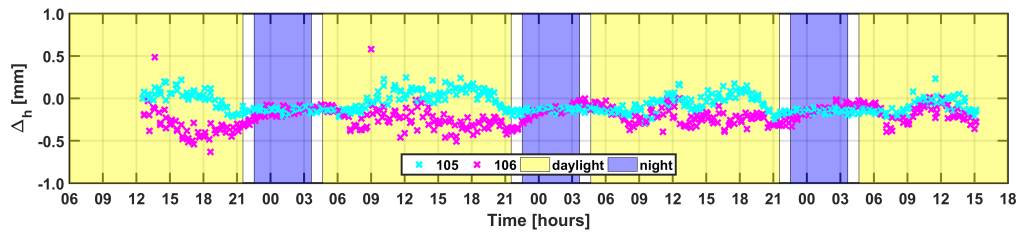
Figure 5.15: Comparison of target 105 and 106, which are nearly equidistant to the setup point, however different undergrounds

5.5   Obtained results from dynamic ATR measurements

For the performance of a dynamic ATR measurement, the locking onto prisms mode is used. Therefore, each dynamic face measurement contains 400 angle readings, where the Leica TS15 is locked onto each prism. As a consequence, it is possible to compute a mean value and the corresponding standard deviation. These parameters should give an insight into how well the ATR method deals with the thermal changes and if the measurement noise can be used for an evaluation process, which rejects measurements.

Proclaimed by (Lienhart et al., 2016, p.2), the attainable frequency of the dynamic measurements is a very important component, which is also decisive whether object motions like bridge vibrations are detectable or not. Normally, when using the tracking mode of the Leica TS15, a measurement rate of 20 Hz is possible. However, after reestablishing a serial connection via the USB converter, there is a distinctive loss of 30-40% in the data transfer performance. Due to the Shannon theorem the maximum detectable frequency of 10 Hz decreases to 6-7 Hz.

For the evaluation of the angle measurement it is necessary to compute the mean value and the corresponding standard deviation based on each sequence, which contains 400 measurements. To do so, it is necessary to exclude the first 50 measurements, because in this period of time the ATR causes variations which indicate a further steering process. Exemplary, three different time stamps which refer to three different meteorological conditions show similar behaviour in Hz and V. As a consequence, possible deviations are eliminated, which is visible in figure 5.16a and 5.16b, where the referring histograms show a normal distribution of the residuals, which is an expected behaviour.
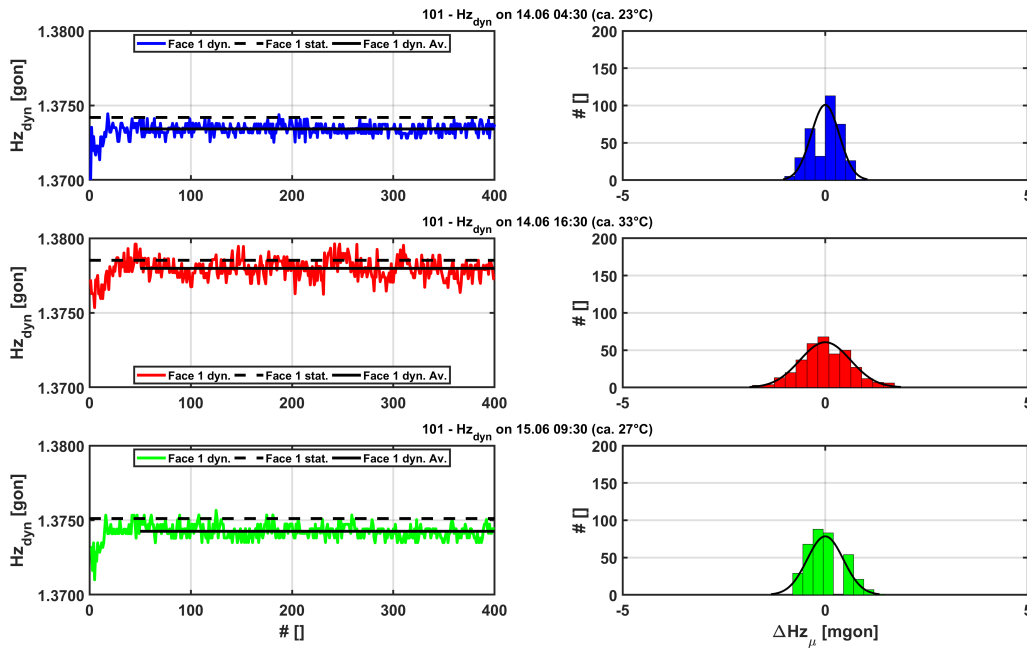
(a) Dynamic measurement of Hz
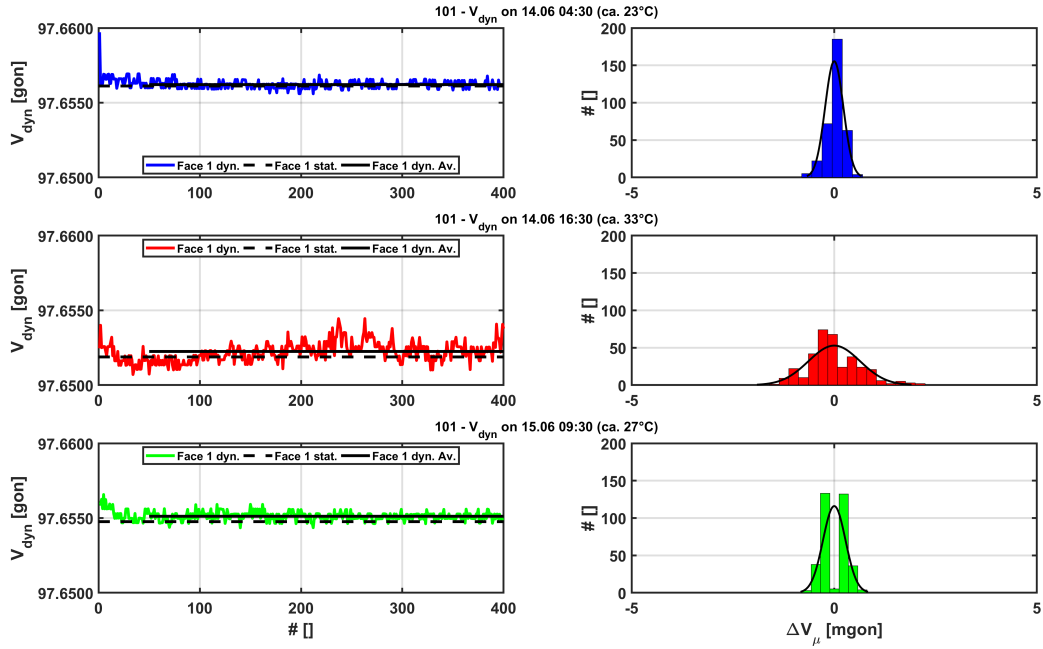
(b) Dynamic measurement of V

Figure 5.16: Visualization of the raw measurement of Hz and V, where the first 50 measurements are excluded to provide mean and standard deviation.

After computing each mean value for Hz and V or rather the face averages, the temporal progress is uniform to the static approach. For comparison, the angle deviations with respect to the first epoch are depicted in figure 5.17. The remaining errors show similar behaviour to the temperature change.
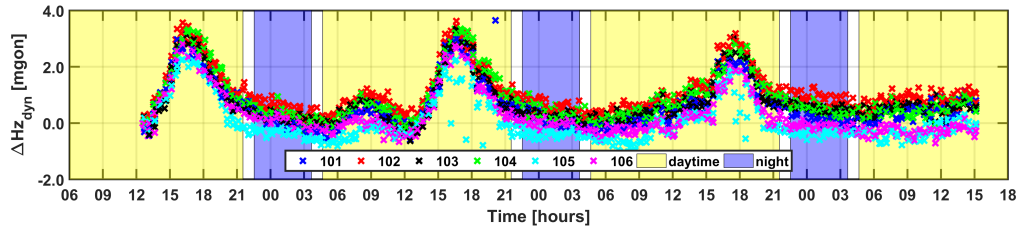
(a) Deviations Hz_{dyn}
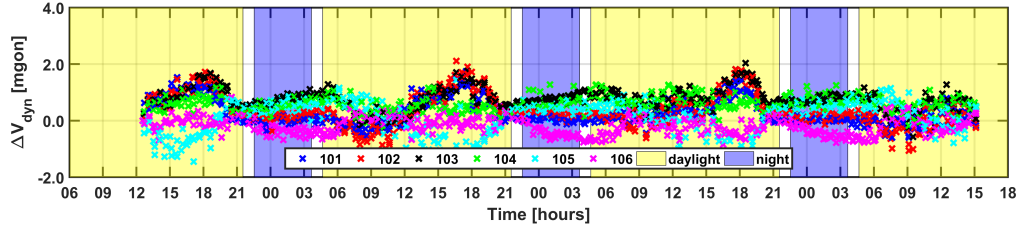
(b) Deviations in of V_{dyn}

Figure 5.17: Deviations of the dynamic angle measurements w.r.t. to the first epoch

Another aspect, which goes hand in hand with temperature, is the behaviour of the standard deviation. To compute the standard deviation for the face averages, variance propagation is needed. Here, the

measurement noise of each face measurement is combined using the Pythagorean addition:

$$s_{x_1,x_2}^2 = (\frac{1}{2})^2 s_{x_1}^2 + (\frac{1}{2})^2 s_{x_2}^2. \tag{5.10}$$

After computing the standard deviation, this shows that the higher the temperature, the higher the air fluctuation becomes. As a consequence of higher air fluctuation, the measurement noise increases. This leads to increased noise in the measurements, which is visualized for target 101 in figure 5.18.
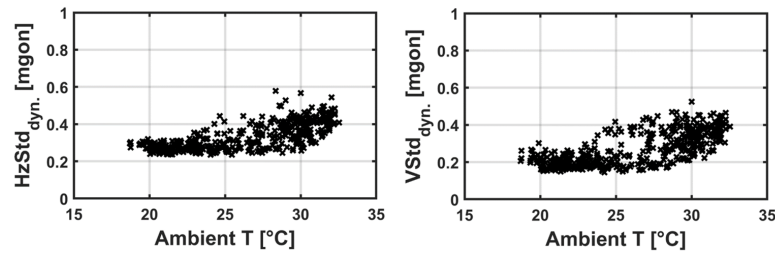
Figure 5.18: The standard deviations of the dynamic angle measurements to target 101 show an expectable correlation to the ambient temperature.

In figure 5.19a and 5.19b the temporal progress of the standard deviation is shown. Here, each target shows a sightly different scaling, which, inter alia, depends on the distance. For better understanding, table 5.2 lists the results for HzStd and VStd for the same time stamps as already used for the showing of the histograms in figure 5.16a and 5.16b. Target 104 can be seen as an exception due to its location near to the ventilation system of the campus's canteen. The depicted results in figures 5.19a-b indicate a large scattering even during the night.

Table 5.2: Comparison of the standard deviations of Hz_{dyn} and V_{dyn} for three different time stamps.

Target	Time [dd.mm HH:MM]	Temperature [°C]	HzStd [mgon]	VStd [mgon]
	14.06 04:30	23	0.27	0.18
101	14.06 16:30	33	0.42	0.43
	15.06 09:30	27	0.33	0.28
	14.06 04:30	23	0.24	0.15
102	14.06 16:30	33	0.39	0.40
	15.06 09:30	27	0.26	0.22
	14.06 04:30	23	0.16	0.12
103	14.06 16:30	33	0.37	0.36
	15.06 09:30	27	0.22	0.18
	14.06 04:30	23	0.19	0.18
104	14.06 16:30	33	0.44	0.49
	15.06 09:30	27	0.34	0.33
	14.06 04:30	23	0.07	0.08
105	14.06 16:30	33	0.31	0.42
	15.06 09:30	27	0.15	0.18
	14.06 04:30	23	0.08	0.08
106	14.06 16:30	33	0.25	0.26
	15.06 09:30	27	0.16	0.16

(a) Standard deviation of Hz

(b) Standard deviation of V
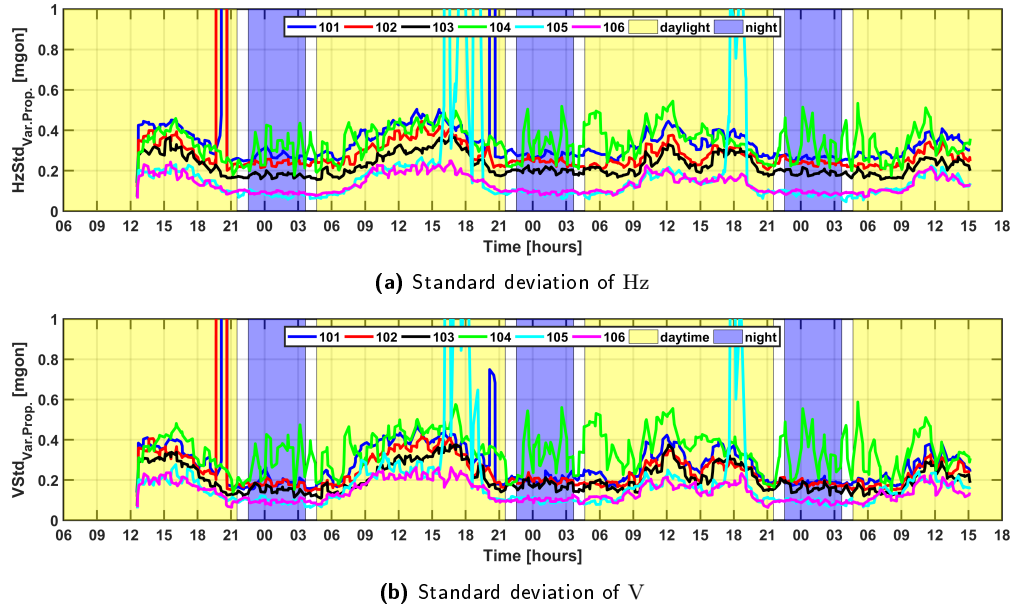
Figure 5.19: Visualized standard deviation of $\mathrm{Hz_{dyn}}$ and $\mathrm{V_{dyn}}$ for all targets showing a scaling factor depending on the distance

Another visible aspect concerns target 105, where at similar time stamps the standard deviation in Hz and V shows distinctive changes. These can also be seen in the raw measurements, shown in figures 5.20a and 5.20b, where both face measurements show distinctive deviations. When having a look at the written GeoCOM protocols, the received response code *1283* indicates a angle measurement, where the results are not corrected by all active sensors like e.g. tilt compensator or prism lock. For the shown example in figure 5.21 most of the measurements are uncorrected, which make them unusable and furthermore wrongly indicate an high measurement noise. Comparing the maximum deviations of $\mathrm{V_{dyn}}$ (middle) with the longitudinal inclination Li (bottom) in figure 5.21, the missing correction terms cannot be related to the tilt compensator's measurements. As a consequence, the source cannot be dissolved or exactly assigned. Furthermore, the maximum amplitude of the angle reading error varies, as shown in figure 5.20a-b. Also, the temporal repetition of the jumps is not solvable. Only for the shown example, a interval of approximately 50 measurements is visible, which does not approve any further knowledge. Therefore, following assumptions are introduced as an explanation for the causing of the obtained artefacts:

- The correction of the position refinement based on ATR and the prism lock show malfunctions.

- The glass surface of the prism is aligned in westerly direction to obtain a rather perpendicular sighting axis between setup point and target. As a consequence, sun reflections might have an impact on the fine adjustment of the Leica TS15. The actual position of the sun in the evening would underpin this assumption. Here, it has to be said, that the instrument does not aim into the direction of the sun, which could also influence the dynamic ATR measurements.

(a) Jumps during the day 2 at 6 o'clock pm

(b) Jumps during the day 3 at 6 o'clock pm
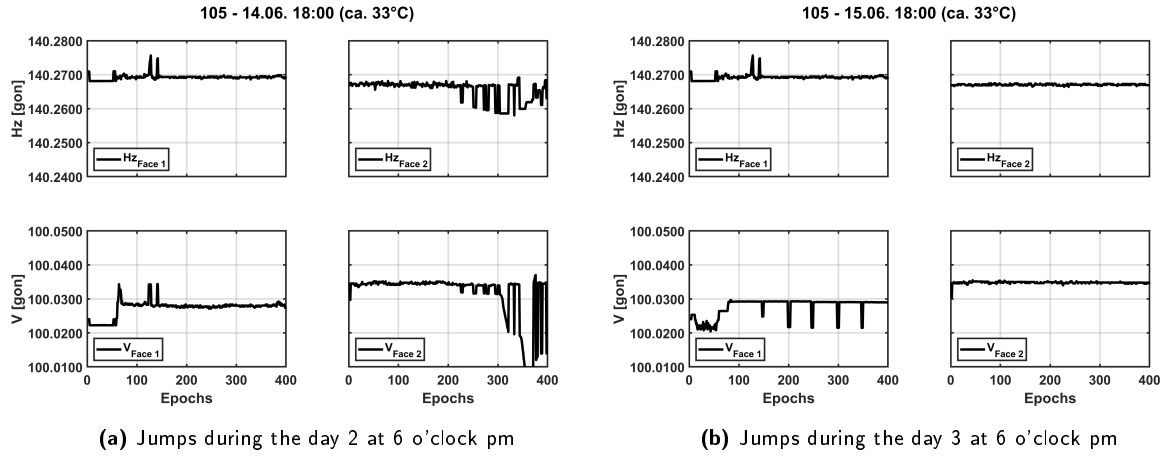
Figure 5.20: Visualization of the standard deviation of Hz and V for all targets, showing that there is a scaling factor corresponding to the distance of the targets.
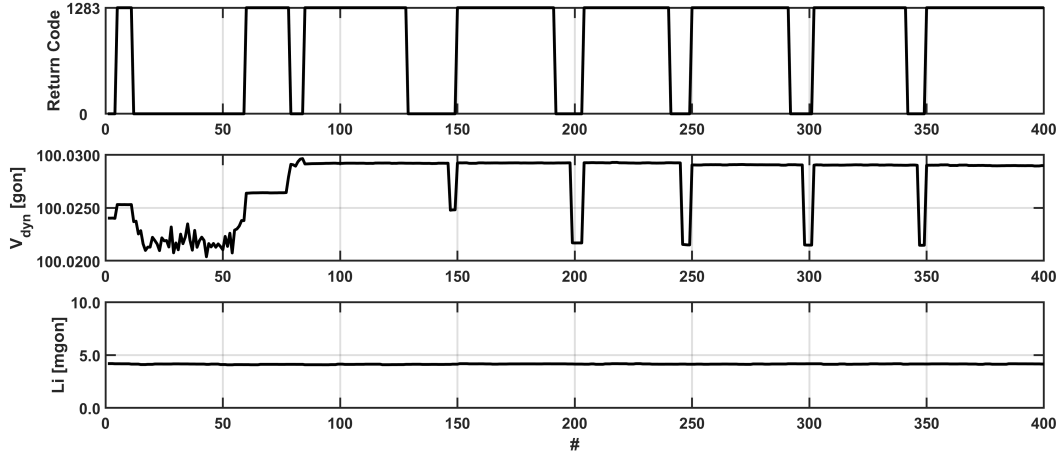
Figure 5.21: Comparison of the response code of GeoCOM, the angle readings based the prism lock mode and the longitudinal inclination measurements

Due to the scaling factor of the standard deviations depicted in figure 5.19a and 5.19b, the measurement's noise can be related to the distance in terms of a linear function, expressed as

$$f: \quad y = k \cdot x + d, \tag{5.11}$$

To depict the linear behaviour, figure 5.22 shows the outcome when estimating a linear function (polynomial function of first degree) based on the standard deviations of Hz_{dyn} and V_{dyn}. Here, as an example the relations are computed for the same time stamps as visualized in figures 5.16a-b. The referring numeric results are presented in table 5.3. It is visible that the offset varies, though the inclination is rather stable depending on the observation quantity.

Table 5.3: Comparison of k and d for three different time stamps.

	Time [dd.mm HH:MM]	Temperature [°C]	k [mgon/m]	d [mgon]
Hz_{dyn}	14.06. 04:30	23 (cool)	0.0010	0.06
	14.06. 16:30	33 (hot)	0.0012	0.22
	15.06. 09:30	27 (medium)	0.0011	0.12
V_{dyn}	14.06. 04:30	23 (cool)	0.0004	0.10
	14.06. 16:30	33 (hot)	0.0006	0.31
	15.06. 09:30	27 (medium)	0.0005	0.15
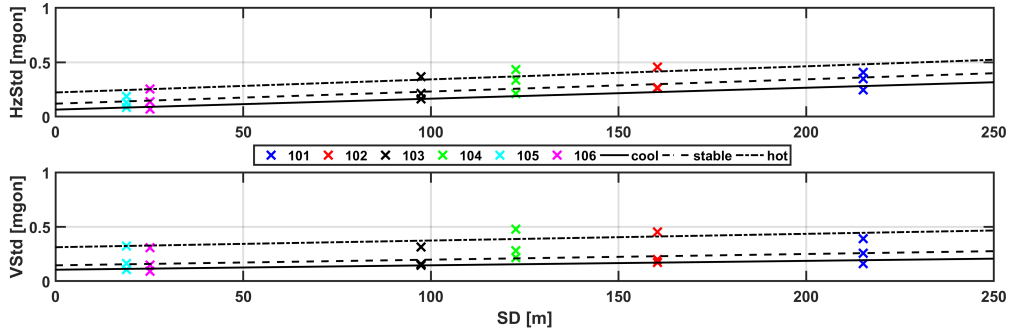
Figure 5.22: Comparison of the standard deviation and the distance, resulting in a linear function

The results for k and d including all epochs are visualized in figure 5.23. The referring outcomes are filtered based on a median absolute deviation (MAD) algorithm using a significance level of $\alpha = 5\%$ to exclude outliers. Because Hz_{dyn} and V_{dyn} show slightly different outcomes, two linear functions are declared. For the derivation of the two indicator functions I_{Hz} and I_V, representatives of k and d have to be expressed. Due to the stable behaviour of k, its average is computed. To avoid the temperature dependency of d, its average is computed only including the outcomes during stable meteorological stages. The resulting relations can then be written as follows

$$I_{Hz}[\text{mgon}] = 0.0010 \frac{[\text{mgon}]}{\text{m}} \cdot \text{SD}[\text{m}] + 0.12[\text{mgon}]$$
$$I_V[\text{mgon}] = 0.0007 \frac{[\text{mgon}]}{\text{m}} \cdot \text{SD}[\text{m}] + 0.15[\text{mgon}].$$

(5.12)
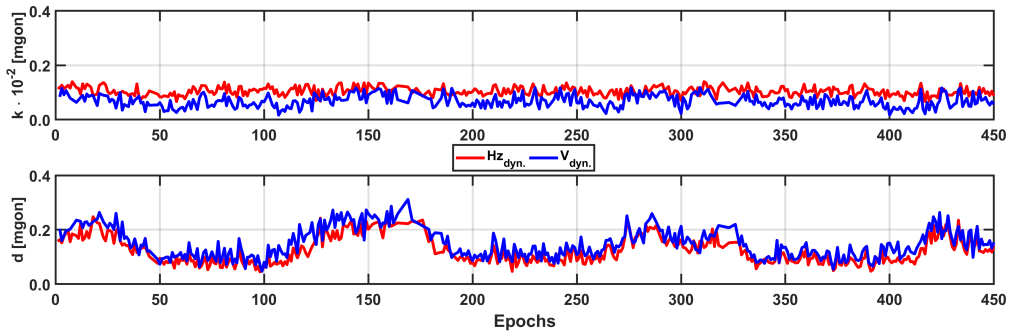
Figure 5.23: Visualization of k and d filtered by a MAD algorithm

The slope distance SD is used as an input parameter x to calculate a threshold. The amplitude of this new quantity therefore only depends on the measured slope distance. The quality of the derived thresholds should be sufficient enough because of different aspects. The first one is because of the use of stable targets, which means that target based variations can be more or less neglected. Furthermore, since the market launch of the TPS1200+ series of Leica (Leica-Geosystems, 2008), the proclaimed angle precision of 1" of the ATR mode remained. Meaning that using a Leica TS15, which has the same specifications, can be seen as representative for all other developed instruments. Other aspects, which prove the model's reproducibility, are the ATR's system accuracy specifications presented in Leica-Geosystems (2015b) and Leica-Geosystems (2019a), which both cover the relation depicted in figure 5.24. Taking the situations of the field test, the maximum distance of approximately 215 m (target 101) only covers a limited scope, which is also seen as a threshold in figure 5.24, where the standard deviation of the ATR remains 1" for measurement under 200 m. Nevertheless, the outcome of the self-obtained model refers to the manufacturer's results, as listed in table 5.4. As a consequence, it is assumed that the computed model based on the dynamic ATR measurements is valid and allows trustworthy evaluation of ATR measurements, which are performed in other deformation monitoring applications.

Table 5.4: Results for $\mathrm{I_{Hz}}$ and $\mathrm{I_V}$ depending on the slope distance of the used targets

Target	Slope distance [m]	$\mathrm{I_{Hz}}$ [mgon]	$\mathrm{I_V}$ [mgon]
101	215.192	0.34	0.29
102	160.357	0.29	0.25
103	97.354	0.22	0.21
104	122.664	0.25	0.23
105	18.869	0.14	0.16
106	25.179	0.15	0.16
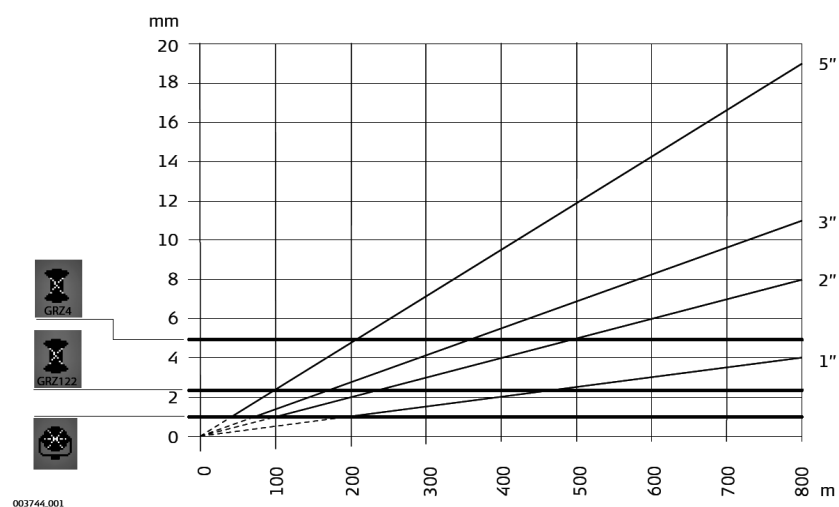
Figure 5.24: Due the system accuracy, the ATR standard deviation is at least based on prism type, distance and instrument accuracy (Leica-Geosystems, 2015b, p.86)

The presented thresholds in table 5.4 are then used to evaluate a measurement based on its noise. As a reference to compute the deviations, a mean value including measurements observed between 0 to 3 am on the 14th of April is computed. Taking these depicted angle deviations of Hz and V of target 101 in figures 5.25a and 5.25b, the measurements derived during daylight suffer from a higher measurement noise, which is consequently detected by the indicator model. On the other hand, throughout more stable meteorological phases like at night, the measurement noise decreases. To obtain a better overview, a classification of the measurements is performed to evaluate the outcome of the model, like:

- All measurements

- Measurements performed at night

- Measurements which are classified to be useful based on the indicator model (good measurements)

Based on this classification, a valid statement should be made, whether the model is a trustworthy tool for evaluating measurements or if hardly any improvements are visible. For that, the angle deviations given in *mgon* will be transformed into displacements given *mm* ($1cc/600m \approx 1mm$). Seen in the context of rigid body motion, it is an advantage to compute the angle deviations into the metric system.

(a) Excluded measurements of Hz
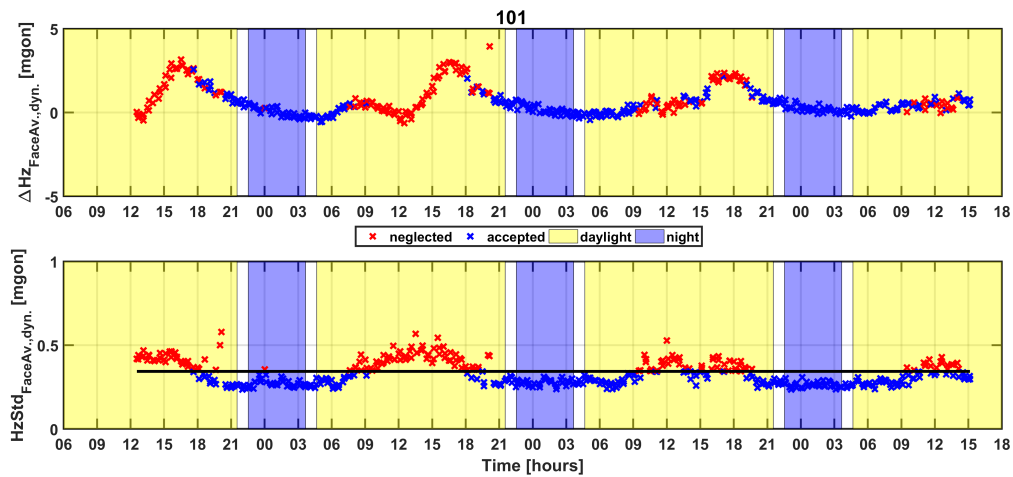
(b) Excluded measurements of V
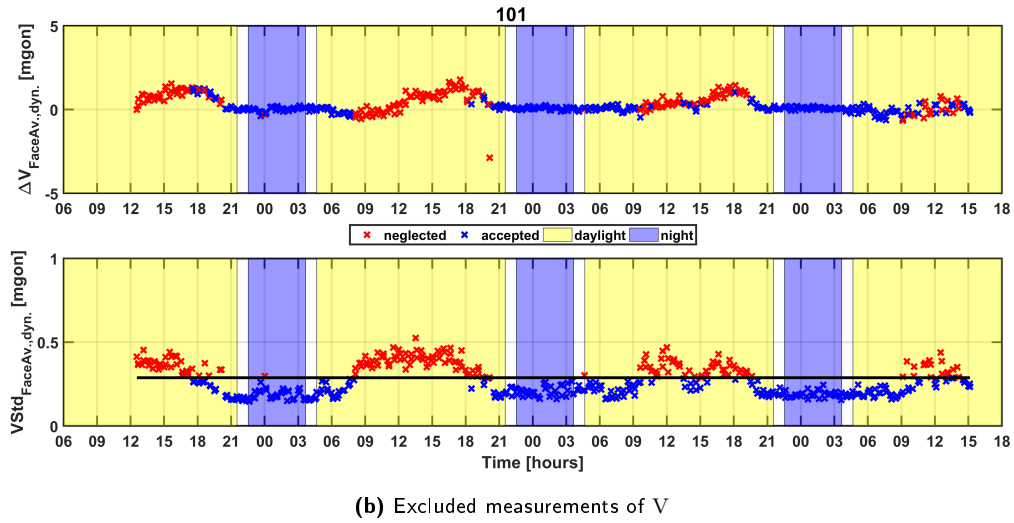
Figure 5.25: Visualization of the applied indicator model for filtering measurements based on their signal-to-noise ratio.

At first, the amount of measurements and the referring availability is compared. On average, approximately 29% of the measurements took place at night. In contrast to that, the amount of good measurements varies depending on the target. Especially target 104 shows a high default rate, which however was already in the looming based on the measurement noise. For all the other targets it yields that around 62% of the measurements of Hz and V are indicated as good measurements, which means that less than 2/3 of all recorded epochs would be used for further investigations.

An aspect, which has to be considered, is that the results of Hz depend on implementing reduced or unreduced measurements. Using unreduced measurements, the range of the calculated displacements is significantly larger than that of V, shown in table 5.5. However, for further research it is recommended to use the reduced measurements of Hz. Here, it is visible that the indicator model does not achieve a big improvement, because most of the systematic influences are neglected beforehand (table 5.6). For instance, the maximum deviation of Hz remain at the same level comparing all measurements with the declared good ones.

However, taking a further look at the outcome for V in table 5.7, an significant improvement is visible. Target 101 has a maximum vertical deviation 10 mm, which however can be reduced down to beneath 5 mm along vertical axis. Additionally, this displacement of approximately 5 mm caused by the vertical angle deviations can be seen as an exception. Only 3% of the good measurements of V show a higher displacement than 3 mm. This would approximately equal 9 epochs. Since the numbers taken as an example only refer to target 101, the actual improvement using the indicator model can be applied for every other target of this field test. The only exception again is target 104, where only approximately 20% of the taken angle measurements can be classified as useful.

Summarising it can be said that the introduced approach of evaluating the measurements based on their noise has some advantages. In contrast to the number of measurements, which only took place at night (from 10 pm to 4 am), a gain of around 100% is achieved. Furthermore, even when there are displacements larger than 3 mm, which would equal around 8-9 cc on 200 m, this still matches a range of $\pm 3\sigma$, due to the specifications given by the manufacturer. However, measurements, which

are neglected, have taken place during meteorologically unstable phases of the day most of the time. Consequently, the experiment in this well-defined framework can be used as a basis to establish an evaluation process based on the measurement noise. Seen in the context of a real monitoring application, it could be implemented as a control unit confirming or rejecting measurements, which normally would trigger an alert system. Therefore, measurements e.g. showing a residual error of 15-20 cc in the face averages, which only originates from daily meteorological variations causing a higher measurement noise, could be detected and neglected. Although, the systematic errors causing this effect cannot be described in more detail based on this experiment.

5.6   Conclusion of the ATR test measurements

The roof top field test is used to determine the systematic effects, which occur when it comes to the static or dynamic ATR measurements using a Leica TS15. The setup without protection from the sun intentionally causes an extreme ambient situation for the instrument. Therefore, especially the temperature correlation of each observation quantity is at the core of interest.

The remaining deviations in the face averages of the angle measurements, which in case of Hz can be eliminated by reducing it onto the first target measured in a set, can be to some extent set into context of the internal temperature change of the instrument. However, like for V the external measurement conditions like the underground are also assumed to effect the measurements. Another aspect is that stable meteorological conditions as seen at night are preferable.

Because these conclusions are already known from previous research, the measurement noise is then used as a basis for an evaluation of the measurements. Based on the dynamic ATR measurements it is possible to obtain a linear relation between the empirical standard deviation and the distance. Based on this function, it is possible to assess the ATR measurements concerning their usability, e.g. in an alarming system, which might be wrongly triggered only because of the variations caused by the temperature correlation. Another effect using such an assessment is that the amount of usable measurements can be significantly increased in contrast to only using observations performed at night.

It is important to mention, that the meaning of the indicator model can be applied to other applications. This is because compared to the specification declared by the manufacturer, the ATR standard deviation is reproducible by using the linear relation expressed in equation 5.12. Therefore the indicator model should give valid results, even when working with longer distances.

Table 5.5: Results based on the indicator model for the horizontal angle Hz

ID	#	Available [%]	|max.| [mm]	# 0-1 mm[%]	# 1-3 mm [%]	# >3 mm [%]
Horizontal Angle reduced - ALL MEASUREMENTS							
101	450	100	14,1	35,1	38,4	26,4
102	450	100	8,2	50,2	31,6	18,2
103	450	100	5,0	73,8	15,1	11,1
104	450	100	6,3	60,0	22,9	17,1
105	450	100	0,9	100,0	0,0	0,0
106	450	100	1,2	96,9	3,1	0,0
Horizontal Angle - MEASUREMENTS AT NIGHT							
101	132	29,3	3,1	59,1	40,2	0,8
102	132	29,3	2,5	72,7	27,3	0,0
103	132	29,3	1,1	98,5	1,5	0,0
104	132	29,3	1,8	85,6	14,4	0,0
105	132	29,3	0,2	100,0	0,0	0,0
106	132	29,3	0,2	100,0	0,0	0,0
Horizontal Angle - GOOD MEASUREMENTS							
101	280	62,2	9,1	44,3	42,9	12,9
102	297	66,0	6,6	58,6	33,3	8,1
103	257	57,1	3,9	89,1	10,1	0,8
104	117	26,0	3,9	78,6	19,7	1,7
105	263	58,4	0,6	100,0	0,0	0,0
106	299	66,4	1,1	99,3	0,7	0,0

Table 5.6: Results based on the indicator model for the reduced horizontal angle Hz

ID	#	Available [%]	|max.| [mm]	# 0-1 mm [%]	# 1-3 mm [%]	# >3 mm [%]
Horizontal Angle reduced - ALL MEASUREMENTS							
101	450	100	0,0	100,0	0,0	0,0
102	450	100	7,7	85,6	13,6	0,9
103	450	100	4,4	96,2	3,3	0,4
104	450	100	4,8	89,1	10,4	0,4
105	450	100	0,9	99,8	0,0	0,2
106	450	100	1,2	99,6	0,2	0,2
Horizontal Angle reduced - MEASUREMENTS AT NIGHT							
101	132	29,3	0,0	100,0	0,0	0,0
102	132	29,3	1,6	90,9	9,1	0,0
103	132	29,3	1,0	99,2	0,8	0,0
104	132	29,3	1,6	96,2	3,8	0,0
105	132	29,3	0,3	100,0	0,0	0,0
106	132	29,3	0,4	100,0	0,0	0,0
Horizontal Angle reduced - GOOD MEASUREMENTS							
101	280	62,2	0,0	100,0	0,0	0,0
102	297	66,0	7,7	88,2	11,4	0,3
103	257	57,1	4,3	98,1	1,2	0,8
104	117	26,0	4,8	94,9	4,3	0,9
105	263	58,4	0,9	99,6	0,0	0,4
106	299	66,4	1,2	99,3	0,3	0,3

Table 5.7: Results based on the indicator model for the vertical angle V

ID	#	Available [%]	|max.| [mm]	# 0-1 mm [%]	# 1-3 mm [%]	# >3 mm [%]
Vertical Angle - ALL MEASUREMENTS						
101	450	100,0	10,3	58,2	26,2	15,6
102	450	100,0	5,4	60,2	29,6	10,2
103	450	100,0	2,1	85,1	14,9	0,0
104	450	100,0	1,5	91,3	8,7	0,0
105	450	100,0	2,9	98,7	1,3	0,0
106	450	100,0	0,5	100,0	0,0	0,0
Vertical Angle - MEASUREMENTS AT NIGHT						
101	132	29,3	1,3	98,5	1,5	0,0
102	132	29,3	1,4	99,2	0,8	0,0
103	132	29,3	0,7	100,0	0,0	0,0
104	132	29,3	1,5	93,9	6,1	0,0
105	132	29,3	0,2	100,0	0,0	0,0
106	132	29,3	0,3	100,0	0,0	0,0
Vertical Angle - GOOD MEASUREMENTS						
101	273	60,7	4,5	82,4	14,3	3,3
102	286	63,6	4,2	78,7	17,1	4,2
103	260	57,8	1,7	91,9	8,1	0,0
104	88	19,6	1,0	98,9	1,1	0,0
105	255	56,7	0,6	100,0	0,0	0,0
106	305	67,8	0,5	100,0	0,0	0,0

6 Measurement campaign at Wald am Schoberpass

According to the stakeholders, a landslide in the area of Wald am Schoberpass is seen as potential risk to the local traffic infrastructure. Therefore, a local engineering office is instructed by the ASFiNAG to perform a monitoring. In cooperation with the TU Graz, the situation at Wald am Schoberpass is used as a testing scenario for different sensor types. Based on the agreements with the stakeholders and the assistance of the local engineering office, a measurement campaign at Wald am Schoberpass took place in 2018 and lasted from 9th to the 30th of April. In this period of time, different surveying instruments were installed to acquire geodetic data. Following sensors have been used to cover different scopes:

- Leica MS60 for prism surveillance

    - used as a RTS for geodetic measurements
    - used as an IATS for taking pictures and recording videos

- Leica GS16 for GNSS support

- Riegl Laser Scanner for full-area surface measurements

- Ground-based synthetic aperture radar (SAR) for full-area surface measurements

- digital single-lens reflex (DSLR) camera for taking overview pictures of the landslide

- Weather station to derive data about meteorological changes of

    - Temperature
    - Air pressure
    - Air humidity
    - Wind velocity
    - Wind direction

In this thesis the measurements derived by the Leica MS60 are mainly taken into account because, next to angle and distance measurements, images and videos are recorded by the OAC, which is located in the optical path of the Leica MS60. For further computation steps the recorded data of the weather station is also of importance to perform e.g. meteorological distance correction and should be used for the determination of the influence of the refraction angle.

6.1 Measurement setup

The instrument is installed on a concrete wall located nearby the critical area. For surveillance, the local surveyor installed targets in the landslide and in the surrounding near to the setup point. These are seen as reference points and basically used for long term stability control. Figure 6.1 gives an overview of the distribution of the target points. All together, there are 20 targets, which are measurable during the whole measurement campaign. The mean distance from the setup point to the landslide targets is about 370 to 450 meters, whereas the targets in the stable area are much

11	MP
12	BRT
13	BRT
14	BRT
15	BRT
16	MP
101	MP
102	MP
103	MP
106	MP
108	MP
109	MP
110	MP
205	MP
207	MP
208	MP
212	MP
1001	RM
1002	RM
1003	BRT
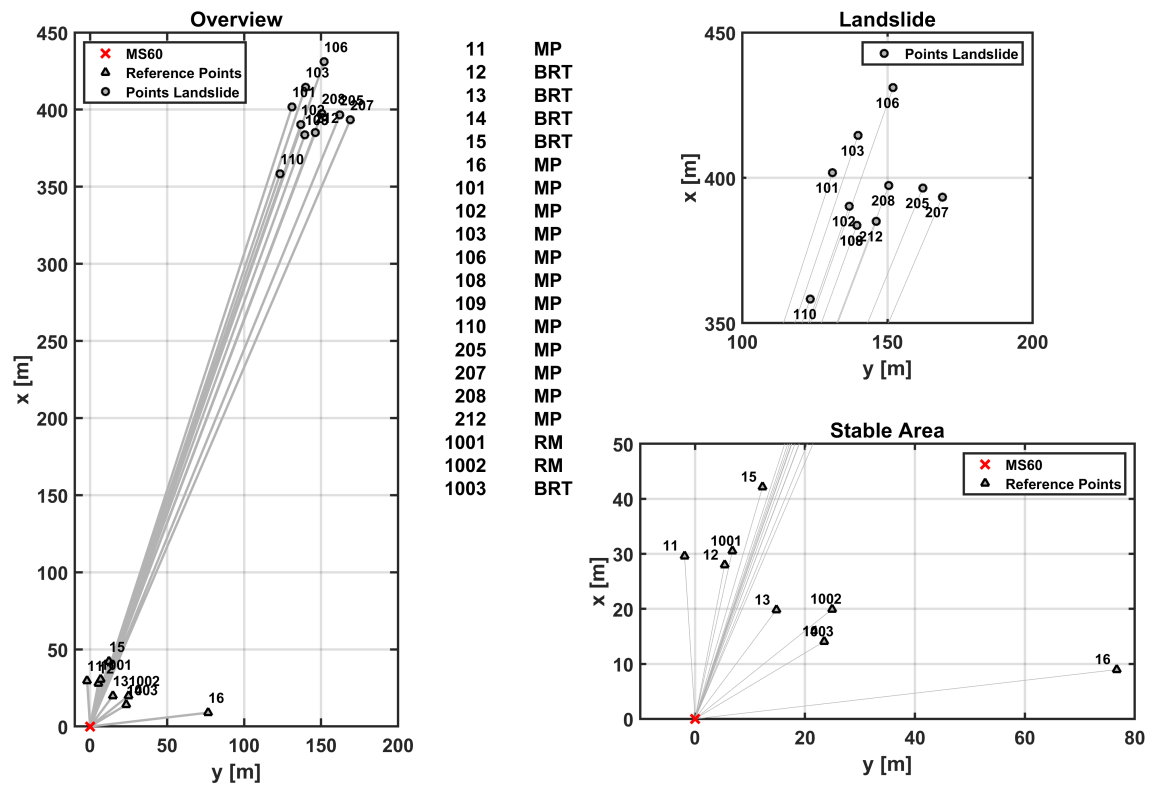
Figure 6.1: Overview of the measurement situation at Wald am Schoberpass during the campaign

closer. The furthest reference point (target 16) is about 80 meters apart. In figure 6.2 pictures are depicted, which show the whole setup of the Leica MS60 or rather its installation using a rail made of aluminium bolted on the small concrete wall. For protection, a wood cabin is put over the setup. The mobile meteo station stands nearby the installation site. In table 6.1 all targets are listed, which have been used during the deformation monitoring. It is important to mention that target 108 and 109 respectively target 14 and 1003 are the same. Is is assumed that during defining the set measurement, the targets got mixed up. The shown images are cropped to the centre part of each picture, showing the target in the middle. Exemplary for target 110, a full image is shown in figure 6.3.

Figure 6.2: Pictures taken from the setup point and the meteo station used for the measurement campaign at Wald am Schoberpass.

55

Figure 6.3: Full image of target 110, showing the mini prism installed on a single rock

Table 6.1: Overview of used targets during the measurement campaign

ID	Type	Area	Image
101	Mini Prism (MP)	Rock Face	
102	Mini Prism (MP)	Rock Face	
103	Mini Prism (MP)	Rock Face	
106	Mini Prism (MP)	Rock Face	

108	Mini Prism (MP)	Rock Face	
109	Mini Prism (MP)	Rock Face	
110	Mini Prism (MP)	Rock Face	
205	Mini Prism (MP)	Rock Face	
207	Mini Prism (MP)	Rock Face	
208	Mini Prism (MP)	Rock Face	
212	Mini Prism (MP)	Rock Face	

11	Mini Prism (MP)	Stable Area	
12	Bireflex Target (BRT)	Stable Area	
13	Bireflex Target (BRT)	Stable Area	
14	Bireflex Target (BRT)	Stable Area	
15	Bireflex Target (BRT)	Stable Area	
16	Mini Prism (MP)	Stable Area	
1001	Reflective Tape (RM)	Stable Areae	

| 1002 | Reflective Tape (RM) | Stable Area | |
| 1003 | Bireflex Target (BRT) | Stable Area | |

6.2   Data acquisition

The observed data measured by the Leica MS60 is split up into three different scopes. Each of these covers different aspects to perform deformation monitoring:

- Robotic Total Station (RTS)
  This set of data describes common geodetic measurements, which can be performed using the Leica MS60. Altogether, about 296 measurement epochs were observed during the campaign. The data mainly include the horizontal and vertical angle measurements, the distance measurements based on the EDM and finally the length and cross inclination of the inbuilt tilt compensator.

- Set of Images (SoI)
  This set of data describes the images, which have been taken using the OAC of the Leica MS60. Altogether, about 67 measurement epochs were observed, in which pictures of all targets were captured. The images are seen as supplement to the recorded RTS data and are compared to the angular measurements from the RTS data set.

- Set of Videos (SoV)
  This set of data describes the videos, which have been recorded using the OAC of the Leica MS60 aiming at one specific target. Altogether, about 75 videos have been recorded during the measurement campaign. The footage is mainly used to possibly describe the influence of the refraction.

6.2.1   Communication control

The data acquisition is based on the communication of the used instrument and the user via a personal computer (PC) (client - server principle). To do so, a serial connection has to be established using an explicit syntax, also known as GeoCOM. GeoCOM is the defined interface to write client applications based on the known platforms (Microsoft Windows, etc.) using American Standard Code

for Information Interchange (ASCII) based communication.

The user specifies requests, which are then received by the listening instrument. The instrument responds to those requests and replies a defined respond code or rather the desired information (Leica-Geosystems, 2006).

Seen in the context of the measurements at Wald am Schoberpass, for each variant of the data acquisition a fitting GeoCOM protocol is used as a basis. In general, at the beginning of each measurement the telescope has to be turned into the right position. This current state is described by steering angles, which have to be injected via the GeoCOM communication and originate from predefining the targets for the current epoch. This is very important, because here also the target type is declared and whether the ATR mode has to be activated or deactivated. Afterwards, the desired information from the instrument is transferred and the written into text files. These files are the basis of each data evaluation routine.

6.2.2   Robotic Total Station

In this section the measurement routine of the RTS data will be explained in detail. Based on a serial connection between the Leica MS60 and a PC, the observed data comprising angle, distance and inclination measurements are recorded and written into text files. The varying target types cause altering steering routines, where different configurations have to be managed, such as reflectorless distance measurement or the de-/activation of the ATR mode. To enlighten the basic idea behind the set measurement, figure 6.4 visualizes the consecutive steps. In addition, the image recording procedure is also included, which will be of primary interest in the next section.
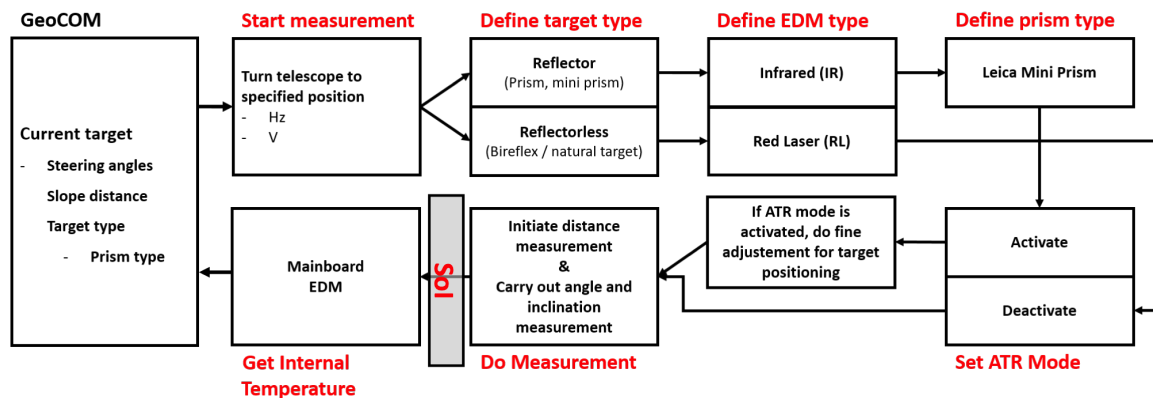
Figure 6.4: Flow chart of the data acquisition concerning RTS data. The syntax is based on GeoCOM protocol. The routine has to handle whether the ATR mode has to be activated or deactivated due to the current target type.

6.2.3   Set of Images

In this section, the measurement routine for the set of images (SoI) data will be described in detail. The process of taking images is included in the routine presented in figure 6.4 from the previous section. The process takes place after the geodetic measurements are recorded. According to the operating system of the Leica MS60, it is possible to distinguish between automatically defined image

settings and customized specifications, e.g. for white balance, exposure time and ISO. White balance or color balance equals the adjustment of color intensities or color correction. The exposure time is a setting describing how long the image sensor is exposed, whereas the ISO corresponds to temporary definition of the sensor's light sensitivity (Striewisch, 2007). It is the current used film speed standard. In table 6.2 the resolution and compression are shown for all images that were taken throughout the measurement campaign.

Table 6.2: Images Settings concerning resolution and compression

Resolution [px]	Compression
2560x1920	JPEG

Additionally, the user is able to fall back on different focus settings such as single shot auto focus, continuous auto focus, focus by distance and focus by contrast. In the context of the measurement campaign, the responsible members of the IGMS went for the manual image settings, however these specifications did not change over time.

One aspect, which has to be considered beforehand, is that the picture is taken after the ATR mode is switched on or off, depending on the target type (e.g. prism or reflective tape). Consequently, the camera position depends either on the steering angle or the position adjustment based on ATR. Figure 6.5 presents a detailed view, what happens when an image is taken based on the presented routine in the previous section. Similar to the RTS approach, the analysis of the images should provide data
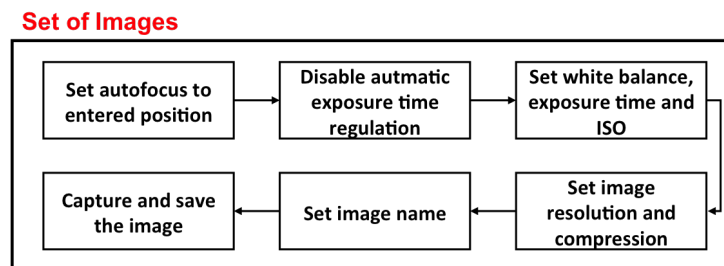
Figure 6.5: Chart of the data acquisition of SoI data based on GeoCOM communication

sets for the horizontal and vertical angles of the referring targets ideally yielding similar results. Unlike the process of evaluating geodetic measurements, the images do not provide angles in the first place. A routine has to be defined to describe the information seen in the images, quantify possible changes and then transform the displacements extracted from the images into angles. This procedure will be explained in section 6.3.

6.2.4 Set of Videos

In this section the measurement routine for the Set of Videos data will be described in detail. Like for the image data acquisition, the OAC of the Leica MS60 is used to record footage of one specific target during the measurement campaign. To do so, different aspects have to be considered. First of all, the stability of the camera system is one of the main problems, when capturing footage for e.g.

at least 10 minutes. Based on the stability control given by the tilt compensator, the simultaneous recording of videos and angle readings should be possible. However, during this process the recording may suffer from conceivably appearing effects like changing environmental influences.

Another issue which has to be considered, is the impact of instrumental errors. Normally, when measuring a set in two faces, the influence of e.g. the index error or collimation error is negligible, because these terms are eliminated when computing the face average. However, performing this kind of image-based monitoring only makes sense recording the video in one face. It is not recommendable to merge data of videos in both faces, when there is a time gap of at least 10 minutes due to the recording duration and other systematics like illumination changes (Ehrhart, 2017). Consequently, the terms of instrumental errors have to computed and applied onto the single face observations.

Citing these possible interferences, the measurement program for the set of videos (SoV) changes compared to the RTS and SoI data acquisition. Additionally, the procedure is mainly considered to determine the influence of the refraction angle. The video settings for all recordings are presented in table 6.3.

Table 6.3: Video specifications during the measurement campaign

Duration [min]	Resolution [px]	Frame Rate [fps]
15	640x480	10

Based on experiments performed by Ehrhart (2017), 10 fps are seen as sufficient enough to detect the refraction's influence. The idea is that a smaller frame rate allows longer shutter times. Consequently, the quality of the video rises especially when dealing with low ambient light conditions. These circumstances considered, the measurement program is presented in 6.6. Only having a time offset of 10 seconds, the measured angles in both faces can be combined to compute instrumental errors and the zero-point-error of tilt compensator. The image-based observations are used to determine a combined vertical index error, which is decisive for the computation of the refraction angle and will be explained in section 6.3 in more detail.

Figure 6.6: Chart of the data acquisition of SoV data

According to the given order depicted in figure 6.6, the measurement routine is the same for each recording sequence, defined by the GeoCOM protocol as follows:

1. Definition of recording settings for the videos based on resolution, frame rate, exposure time, ISO and white balance.

2. Introducing steering angles via GeoCOM protocol

3. The instrument or rather telescope is turned to the referring position

4. The ATR mode is activated and fine adjustment is performed (sighting axis is mathematically corrected into the centre of the prism)

5. Performing a complete measurement including distance and angles, which are corrected by the tilt compensator and ATR (GeoCOM request *GetFull*)

6. Perform simultaneously video and dynamic angle recordings (GeoCOM request *GetAngle*). Here, the angle readings are only corrected by the tilt compensator. This is because the lock mode for prism tracking is not used and therefore the read angles are recorded without the influence of the ATR.

7. After the dynamic measurements, again a complete measurement including distance and corrected angles (tilt compensator + ATR) is performed.

6.3   Data evaluation

The following section shows the different evaluation methods for each presented data set. The developed routines approve a comparison of the different data sets. The achieved outcomes are used to describe the behaviour of the landslide at Wald am Schoberpass.

6.3.1   Robotic Total Station

Based on the measurement routine, the main observation quantities are the horizontal angle Hz, vertical angle V, slope distance SD, length inclination Li and cross inclination Ci. The data evaluation in figure 6.7 depicts how the measured values are processed, examined concerning gross errors and finally combined to describe metric displacements over time.
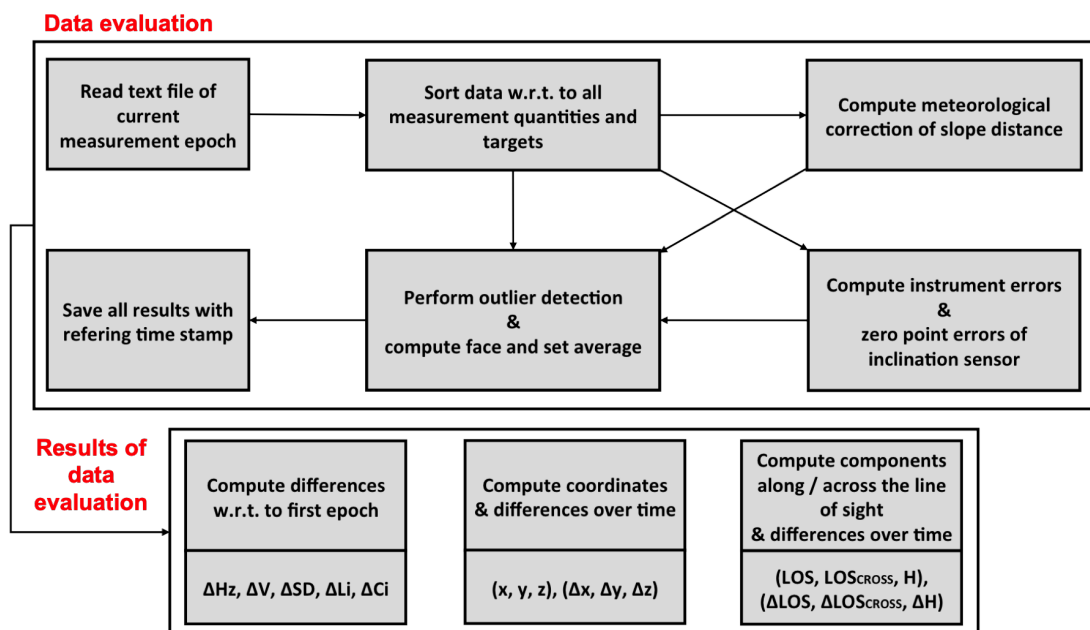
Figure 6.7: Chart of the RTS data evaluation

It is recommended to combine the single face measurements, because the observations are provided in both faces. Based on equation 6.1, the face averages and absolute inclinations can be computed (Möser et al., 2012).

$$
\begin{aligned}
\overline{\mathrm{Hz}} &= \frac{\mathrm{Hz_I} + (\mathrm{Hz_{II}} \pm \pi)}{2} \\
\overline{\mathrm{V}} &= \frac{\mathrm{V_I} + (2\pi - \mathrm{V_{II}})}{2} \\
\overline{\mathrm{SD}} &= \frac{\mathrm{SD_I} + \mathrm{SD_{II}}}{2} \\
\overline{\mathrm{Li}} &= \frac{\mathrm{Li_I} - \mathrm{Li_{II}}}{2} \\
\overline{\mathrm{Ci}} &= \frac{\mathrm{Ci_I} - \mathrm{Ci_{II}}}{2}
\end{aligned}
\tag{6.1}
$$

These equations fit for each set measurement. There is the possibility of combining the sets. Consequently, one representative for each measurement quantity within one epoch is defined and furthermore gross errors could be detected much easier due to the procedure of exclusion.

The instrument errors and zero point error of the tilt compensator along and across the instrument axes are also of primary interest (equation 6.2), because these values partially indicate the influence of environmental changes on the setup point (Walser, 2005, pp.44-46).

$$
\begin{aligned}
\epsilon_{\mathrm{coll}} &= \frac{((\mathrm{Hz_{II}} \pm \pi) - \mathrm{Hz_I})}{2} \\
\epsilon_{\mathrm{index}} &= \frac{(\mathrm{V_I} - (2\pi - \mathrm{V_{II}})}{2} \\
\epsilon_{\mathrm{Li}} &= \frac{\mathrm{Li_I} + \mathrm{Li_{II}}}{2} \\
\epsilon_{\mathrm{Ci}} &= \frac{\mathrm{Ci_I} + \mathrm{Ci_{II}}}{2}
\end{aligned}
\tag{6.2}
$$

Being affected by the atmosphere, the EDM measurements have to deal with similar issues. The meteorological distance measurement correction is presented in equation 6.3 (Leica-Geosystems, 2019a, pp.83-84).

$$
\Delta \mathrm{SD_m^i} = 286.338 - \left[\frac{0.29535 \cdot \mathrm{p^i}}{(1 + \alpha \cdot \mathrm{t^i})} - \frac{4.126 \cdot 10^{-4} \cdot \mathrm{h^i}}{(1 + \alpha \cdot \mathrm{t^i})} \cdot 10^{\mathrm{x}} \right]
\tag{6.3}
$$

where

$$
\mathrm{x} = \left(7.5 \cdot \frac{\mathrm{t}}{(237.3 + \mathrm{t})} \right) 0.7857.
\tag{6.4}
$$

As shown in equation 6.3, the meteorological data t (Temperature), p (air pressure) and h (air humidity) of the referring epoch *i* have to be taken into account to achieve the fitting correction. Consequently, the raw distance measurement is adjusted, as shown in equation 6.5 (Möser et al., 2012, pp.264-265).

$$
\overline{\mathrm{SD}}_{\mathrm{m}}^{\mathrm{i}} = \overline{\mathrm{SD}}_{\mathrm{raw}}^{\mathrm{i}} + \Delta \mathrm{SD_m^i}
\tag{6.5}
$$

After processing the averaged quantities $\overline{\mathrm{Hz}}$, $\overline{\mathrm{V}}$ and $\overline{\mathrm{SD_m}}$, it is possible to calculate 2D coordinates of the targets with respect to the setup point, using the first main task

$$
\begin{aligned}
\mathrm{x}_\mathrm{N}^\mathrm{i} &= \mathrm{x}_0 + \overline{\mathrm{SD}}_\mathrm{m}^\mathrm{i} \cdot \cos(\overline{\mathrm{Hz}}^\mathrm{i}) \\
\mathrm{y}_\mathrm{N}^\mathrm{i} &= \mathrm{y}_0 + \overline{\mathrm{SD}}_\mathrm{m}^\mathrm{i} \cdot \sin(\overline{\mathrm{Hz}}^\mathrm{i})
\end{aligned}
\tag{6.6}
$$

where x_0 and y_0 equals 0 and the Hz is declared as orientated horizontal angle. Though, it has to be considered, that the assumed deformation of the landslide is much better visible along and across the line-of-sight (LOS) of the Leica MS60. Therefore, these and the height components are computed to have a better idea of possible movements concerning the area. Because the change along the LOS refers to the change of SD, its deviations over time are computed as

$$
\Delta\mathrm{LOS}^\mathrm{i} = \overline{\mathrm{SD}}_\mathrm{m}^\mathrm{i} - \overline{\mathrm{SD}}_\mathrm{m}^1.
\tag{6.7}
$$

The component across the LOS shown in figure 6.8 is calculated as

$$
\Delta\mathrm{LOS}_\mathrm{CROSS}^\mathrm{i} = \overline{\mathrm{SD}}_\mathrm{m}^\mathrm{i} \cdot (\overline{\mathrm{Hz}}^\mathrm{i} - \overline{\mathrm{Hz}}^1)
\tag{6.8}
$$

assuming that $(\overline{\mathrm{Hz}}^\mathrm{i} - \overline{\mathrm{Hz}}^1) << 0$ and therefore can be computed like an arc element.
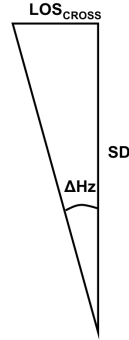
Figure 6.8: Schematic representation of the component across the LOS

The last component is the height computed as the height difference between the setup point and the current target like

$$
\Delta\mathrm{h}^\mathrm{i} = \overline{\mathrm{SD}}_\mathrm{m}^\mathrm{i} \cdot \cos(\overline{\mathrm{V}}^\mathrm{i}) + \frac{(\overline{\mathrm{SD}}_\mathrm{m}^\mathrm{i} \cdot \sin(\overline{\mathrm{V}}^\mathrm{i}))^2 \cdot (1-\mathrm{k})}{2\mathrm{R}},
\tag{6.9}
$$

where R equals the earth's radius ($\mathrm{R} = 6379000\,\mathrm{m}$). The included refraction coefficient *k* is based on literature (Möser et al., 2012). In practical use, the coefficient is supposed to be $\mathrm{k} = 0.13$ most of the times. This value was developed by *Gauß* in 1823 related to light waves. In case of Wald am Schoberpass, the setup point is near to the ground level, which provokes a much higher uncertainty concerning the refraction coefficient of about 10-20 times. The main influential parameter is the temperature gradient. At ground level, it is negative most of the times because of cooler air (Möser et al., 2012, Pages 318-319). All these aspects are not considered for the current evaluation of the height component, however knowing these impacts, the results of the height component are assessed

with caution.

6.3.2   Set of Images

The evaluation process concerning the SoI is parted into two consecutive steps (shown in figure 6.9). The first one refers to the image registration via feature matching. Here it is very important to define a reference epoch, from which an image for each target is taken and used for the comparison. As a consequence of this processing step, pixel differences can be derived.

The second step is based on mathematical relations introduced by Ehrhart and Lienhart (2017), whereby the theoretical framework is extended by Ehrhart (2017). In the thesis, a coarse overview is given to enlighten the basic principles behind transformation from image coordinates to theodolite angles.
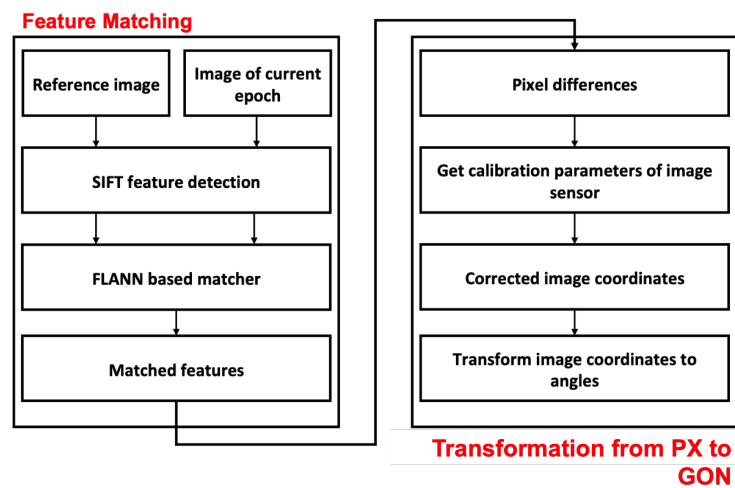
Figure 6.9: Chart of the SoI data evaluation process

6.3.2.1   Feature detection and matching

Feature Matching is one possibility of image registration. It is based on the fact, that there a characteristic spots in each picture declared as feature points plus referring unique specifications called descriptors. The feature detection routine, which has been used, was implemented via OpenCV and is based on the SIFT algorithm developed by Lowe (2004). For the matching procedure, the FLANN based matcher algorithm is used. The apt theoretical background is explained in chapter 3.3.2.

The adapted algorithm evaluating the SoI data of Wald am Schoberpass delivers corresponding keypoints in the reference and second image for each comparison. Dealing with possible mismatches, it is absolutely vital to perform an outlier detection. Therefore, two consecutive routines are used, which are

1. Lowe's threshold

2. RANSAC.

Using Lowe's threshold, it is possible to detect up to 90% of the false matches by discarding less than 5% of the correct ones. The RANSAC algorithm is often used in CV, especially when comparing feature points, because it is one of the most robust detectors (Luhmann, 2018, pp. 131-132). After filtering false positives, the detected local maxima should perfectly fit, like demonstrated in figures 6.10b.
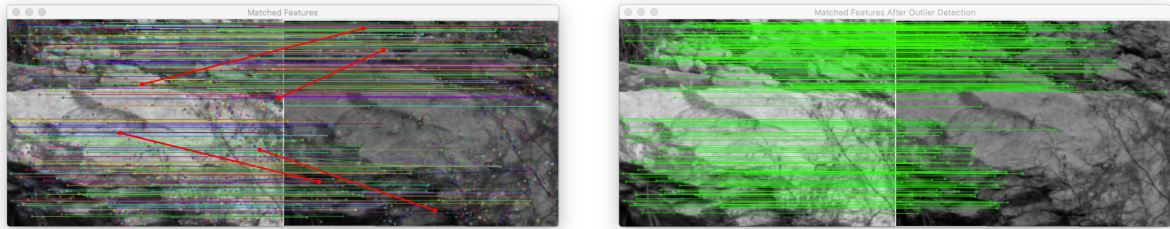
(a) First matching result after adpating Lowe's threshold   **(b)** Second matching result after adapting RANSAC algorithm

Figure 6.10: Performing outlier detection using both, the approach of Lowe (2004) and the RANSAC algorithm

Having a valid detection of mismatches is necessary. A further idea is separating the image into multiple regions to compensate different feature point motions. Due to varying backgrounds (trees, stones, etc.) like in figure 6.11a, the idea is to perform the feature matching for two regions of interests to reduce the impact of these influences in the image shown in figure 6.11b, where e.g. individual stones might change their position and orientation or leaves of the trees will move because of wind.

Furthermore, these regions are declared near to the centre of the image to reduce the impact of lens distortion and normally the images are more crisp in the middle. This equals better contrast and sharper edges (Luhmann, 2018, p.448).
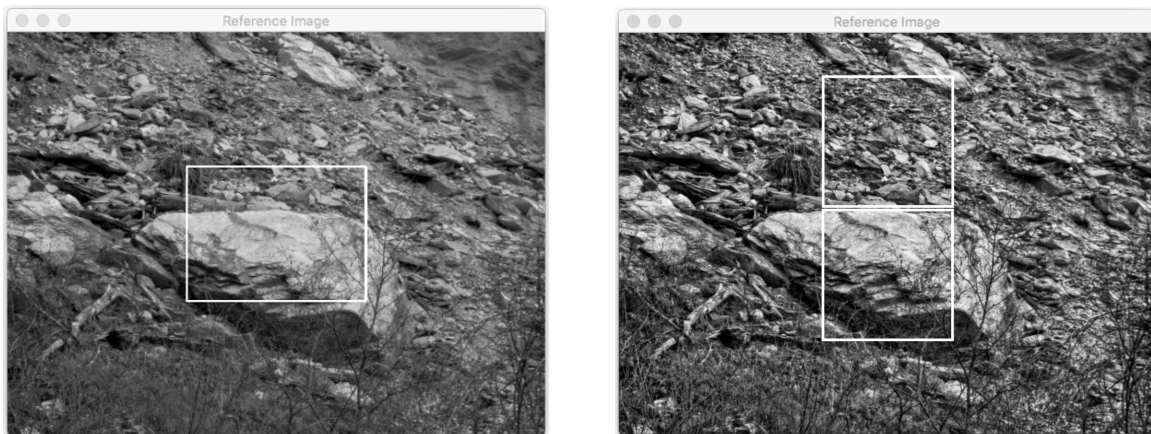
(a) One region of interest   **(b)** Two seperate regions of interest

Figure 6.11: Performing feature matching for central regions in the picture

For each region of interest, a displacement vector in horizontal and vertical direction (equation 6.10) can be determined, where one representative pixel difference and the referring precision is calculated based on the mean and corresponding standard deviation.

$$\Delta u_i = \begin{pmatrix} (u_1 - u_{1,\text{ref}}) \\ (u_2 - u_{2,\text{ref}}) \\ (u_3 - u_{3,\text{ref}}) \\ ... \\ (u_{n-1} - u_{n-1,\text{ref}}) \\ (u_n - u_{n,\text{ref}}) \end{pmatrix} \qquad \Delta v_i = \begin{pmatrix} (v_1 - v_{1,\text{ref}}) \\ (v_2 - v_{2,\text{ref}}) \\ (v_3 - v_{3,\text{ref}}) \\ ... \\ (v_{n-1} - v_{n-1,\text{ref}}) \\ (v_n - v_{n,\text{ref}}), \end{pmatrix} \qquad (6.10)$$

where (u_n, v_n) are the image coordinates of a feature in the current frame, whereas $(u_{\text{ref}}, v_{\text{ref}})$ refer to counterpart feature in the reference image. As a consequence, it is possible to combine the displacements of both regions based on the arithmetic average assuming that all points (features) move in the same direction. Therefore, one representative displacement value for both components u and v is derived and added to the middle point of the sensor (equation 6.11). The overall standard deviation is computed by adapting a variance propagation (equation 6.13).

$$u_{\text{pixel}} = u_{\text{mid}} + \Delta u$$
$$v_{\text{pixel}} = v_{\text{mid}} + \Delta v \qquad (6.11)$$

where

$$\Delta u = \frac{\Delta u_1 + \Delta u_2}{2}$$
$$\Delta v = \frac{\Delta v_1 + \Delta v_2}{2}. \qquad (6.12)$$

$$\sigma_u^2 = \left(\frac{\partial \Delta u}{\partial \Delta u_1} \right)^2 \cdot \sigma_{u_1}^2 + \left(\frac{\partial \Delta u}{\partial \Delta u_2} \right)^2 \cdot \sigma_{u_2}^2$$

$$\sigma_v^2 = \left(\frac{\partial \Delta v}{\partial \Delta v_1} \right)^2 \cdot \sigma_{v_1}^2 + \left(\frac{\partial \Delta v}{\partial \Delta v_2} \right)^2 \cdot \sigma_{v_2}^2 \qquad (6.13)$$

6.3.2.2   Transformation from pixel differences to angle deviations

After computing u_{pixel} and v_{pixel}, a transformation from image coordinates to theodolite angles has to be applied (Ehrhart, 2017, pp.159-179). Here different computation levels have to be considered, when transforming pixel differences to angle deviations:

1. Relation between image sensor and image system

2. Relation between image and camera system

3. Relation between camera and telescope system

4. Relation between telescope and theodolite system

These relations are also called mapping relations and visualized in form of four coordinate systems,

shown in figure 6.12 (Walser, 2005, p.50).
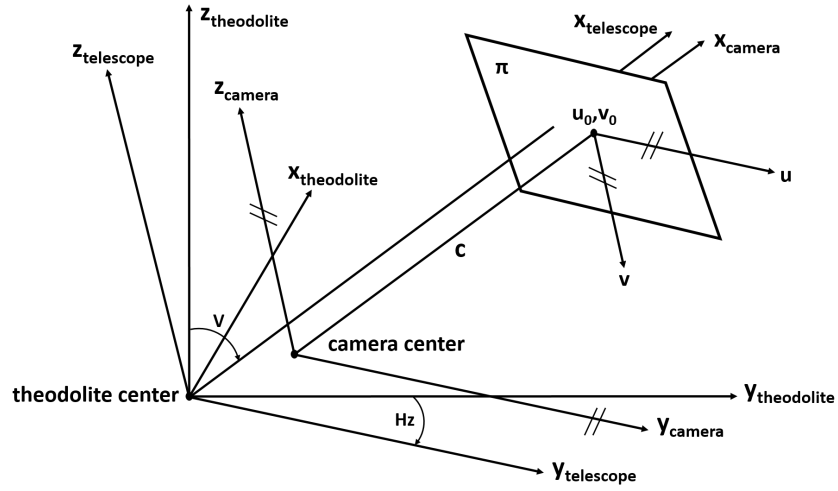
Figure 6.12: Coordinate systems, which are related to each other when computing image-based angles, after Ehrhart (2017)

The first aspect, which has to be taken in account, is when measuring in two faces, the image sensor is once located up side down (shown in figure 6.13).
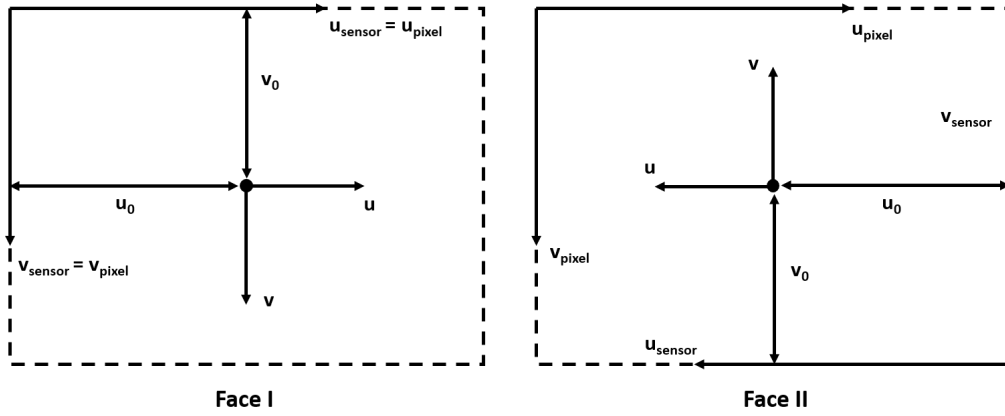
Figure 6.13: Change of the image system depending on measuring in Face I or Face II, after Ehrhart (2017)

So the final image sensor coordinates for both faces result from the pixel coordinates, shown in equation 6.14, where w and h denote the width and the height of the sensor.

$$u_{\text{sensor}}^{\text{I}} = u_{\text{pixel}}^{\text{I}}$$
$$v_{\text{sensor}}^{\text{I}} = v_{\text{pixel}}^{\text{I}}$$
$$u_{\text{sensor}}^{\text{II}} = w - u_{\text{pixel}}^{\text{II}} \tag{6.14}$$
$$v_{\text{sensor}}^{\text{II}} = h - v_{\text{pixel}}^{\text{II}}$$

The next step of the processing routine is to correct the derived image sensor coordinates. Here different influences have to be considered due to an erroneous camera system, such as

- Different scale factor of the axis of the image sensor coordinate system

- Sheared axis (affine axis) of the image sensor coordinate system

- Distortions caused by lens system (radial, tangential).

Theoretically, all these influences effect the sensor coordinates u_{sensor} and v_{sensor} like

$$\begin{pmatrix} u \\ v \end{pmatrix} = \begin{pmatrix} m & o \\ 0 & 1 \end{pmatrix} \begin{pmatrix} u' \\ v' \end{pmatrix} + \begin{pmatrix} \Delta u_{rad} \\ \Delta v_{rad} \end{pmatrix} + \begin{pmatrix} \Delta u_{tan} \\ \Delta v_{tan} \end{pmatrix} \tag{6.15}$$

with o equalling the non-orthogonality of the axis u and v and $(\Delta u_{rad}, \Delta v_{rad})$ and $(\Delta u_{tan}, \Delta v_{tan})$ describing the lens distortions. Additionally, the offset of the principle point

$$\begin{pmatrix} u' \\ v' \end{pmatrix} = \begin{pmatrix} u_{sensor} - u_0 \\ v_{sensor} - v_0 \end{pmatrix}. \tag{6.16}$$

influences the distortion functions, which are described as polynomial functions and depend of the location of the principle point on the sensor. The radial distortion is described in equation 6.17, whereas the tangential distortion is shown in equation 6.18. Here, r^2 is defined as $r^2 = u'^2 + v'^2$ and r_0 refers to approximately 2/3 of the maximum image radius (Luhmann, 2018, pp.180-184).

$$\begin{pmatrix} \Delta u_{rad} \\ \Delta v_{rad} \end{pmatrix} = \begin{pmatrix} u' \\ v' \end{pmatrix} \left(\left(r^2 - r_0^2\right) K_1 + \left(r^4 - r_0^4\right) K_2 + \left(r^6 - r_0^6\right) K_3 \right) \tag{6.17}$$

$$\begin{pmatrix} \Delta u_{tan} \\ \Delta v_{tan} \end{pmatrix} = \begin{pmatrix} \left(r^2 + 2u'^2\right) P_1 + 2\,P_2\,u'v' \\ \left(r^2 + 2v'^2\right) P_2 + 2\,P_1\,u'v' \end{pmatrix}. \tag{6.18}$$

The next step is to find the transition from 2D image coordinates u and v to 3D camera coordinates $(x_{camera}, y_{camera}, z_{camera})$ (shown in figure 6.14). Here, the basic principle of a pinhole camera is used to relate

$$\begin{pmatrix} x_{camera} \\ y_{camera} \\ z_{camera} \end{pmatrix} = \alpha \begin{pmatrix} c \\ u \\ -v \end{pmatrix}. \tag{6.19}$$

where

$$\alpha = \frac{d}{\sqrt{u^2 + v^2 + c^2}}. \tag{6.20}$$

c stands for the camera constant and d describes the distance from camera centre to the measured target. Additionally, this step provides the image coordinates in meters by introducing the distance d.
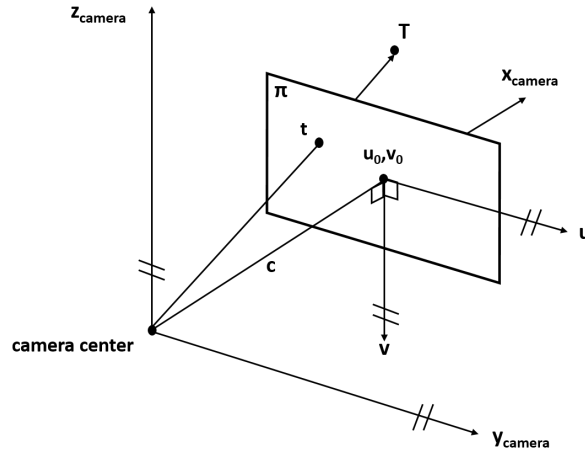
Figure 6.14: Relation between image and camera system based on the pinhole camera geometry, after Ehrhart (2017)

It is necessary to transform the camera system into the telescope system by a well-known 6 parameter transformation, because the camera is rigidly mounted to the telescope of the used IATS (Luhmann, 2018, pp.60-61), shown in figure 6.15

$$
\begin{pmatrix} x_{\text{telescope}} \\ y_{\text{telescope}} \\ z_{\text{telescope}} \end{pmatrix} = \mathbf{R}_\omega \mathbf{R}_\varphi \mathbf{R}_\kappa \begin{pmatrix} x_{\text{camera}} \\ y_{\text{camera}} \\ z_{\text{camera}} \end{pmatrix} + \begin{pmatrix} x_0 \\ y_0 \\ z_0 \end{pmatrix}
\tag{6.21}
$$

where κ, φ, ω refer to the three Euler rotation angles and (x_0, y_0, z_0) are the camera centre coordinates in the telescope system.
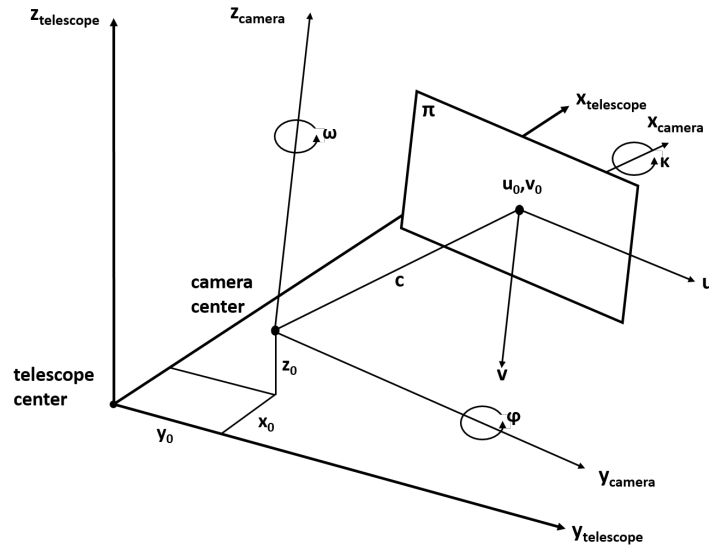
Figure 6.15: Relation between camera and telescope system based on 6 parameter transformation, after Ehrhart (2017)

The last mapping relation is the transition from the telescope to theodolite system (shown in equation 6.22).

$$\begin{pmatrix} x_{\text{theodolite}} \\ y_{\text{theodolite}} \\ z_{\text{theodolite}} \end{pmatrix} = \mathbf{R} \begin{pmatrix} x_{\text{telescope}} \\ y_{\text{telescope}} \\ z_{\text{telescope}} \end{pmatrix} \tag{6.22}$$

Here, a rotation matrix is declared shown in equation 6.23. The horizontal angle Hz and V of the current telescope position have to be considered, because of the relation to the theodolite system. These have to be regarded without the tilt correction. Therefore, it is necessary to take the inclination readings into account (shown in equation 6.24).

$$\mathbf{R} = \begin{pmatrix} \cos(Hz) & -\sin(Hz) & 0 \\ \sin(Hz) & \cos(Hz) & 0 \\ 0 & 0 & 1 \end{pmatrix} \begin{pmatrix} \sin(V) & 0 & -\cos(V) \\ 0 & 1 & 0 \\ \cos(V) & 0 & \sin(V) \end{pmatrix} \tag{6.23}$$

$$\begin{aligned} Hz &= Hz_{\text{tilt}} - C_i \cot(V_{\text{tilt}}) \\ V &= V_{\text{tilt}} - L_i \end{aligned} \tag{6.24}$$

In the end, it is possible to compute the angles in the theodolites coordinate system like

$$\begin{aligned} Hz_T &= \arctan\left(\frac{y_{\text{theodolite}}}{x_{\text{theodolite}}}\right) \\ V_T &= \arctan\left(\frac{\sqrt{x_{\text{theodolite}}^2 + y_{\text{theodolite}}^2}}{z_{\text{theodolite}}}\right). \end{aligned} \tag{6.25}$$

Afterwards, it is necessary to re-correct the theodolite angles, because the tilting influence is not neglectable (Walser, 2005, p. 56), written as

$$\begin{aligned} V_{T,\text{tilt}} &= V_T + i_{\text{long},T} \\ Hz_{T,\text{tilt}} &= Hz_T + i_{\text{trans},T} \cot(V_{T,\text{tilt}}). \end{aligned} \tag{6.26}$$

The tilting influence relative to the current horizontal pointing direction is declared as follows (Walser, 2005, p. 56)

$$\begin{aligned} i_{\text{long},T} &= i_{\text{abs}} \sin(i_{\text{angle}} + Hz_T) \\ i_{\text{trans},T} &= i_{\text{abs}} \cos(i_{\text{angle}} + Hz_T). \end{aligned} \tag{6.27}$$

where

$$\begin{aligned} i_{\text{abs}} &= \sqrt{L_i^2 + C_i^2} \\ i_{\text{angle}} &= \arctan\left(\frac{L_i}{C_i}\right) - Hz \end{aligned} \tag{6.28}$$

Summing up all these mapping relations, it clearly has to be pointed out that not every of these influences can be determined with statistical significance. Different reasons approving this assumption

are shortly presented (Ehrhart, 2017, pp. 170-171):

- x_0, y_0 and z_0 cannot be estimated due to small rotation angles κ, φ, ω and the fact, that the distance between the camera and telescope centre can only be determined with a precision of about 2 mm (Vogel, 2006; Wasmeier, 2009).

- Due to Schirmer (1994) and Hartley and Zisserman (2004) scale differences and non-orthogonality of the image sensor system (u and v axis) are unlikely and therefore defined as $m = 1$ and $o = 0$.

- Based on Walser (2005) and Vogel (2006), lens distortion can be linearised or neglected. As a consequence, only the first term of the radial distortion including the coefficient $K1$ is considered (Wasmeier, 2009, p.34). The tangential is omitted because its impact is one order of magnitude smaller than the influence of radial distortion (Kraus, 2007, p. 53).

In the end, seven quantities, listed in table 6.4, are used to sufficiently parametrize the mapping relation between the image sensor coordinates and the theodolite angles. Therefore equation 6.15 is rewritten to

$$\begin{pmatrix} u \\ v \end{pmatrix} = \left(1 + (r^2 - r_0^2)\, K_1\right) \begin{pmatrix} \cos(\kappa) & -\sin(\kappa) \\ \sin(\kappa) & \cos(\kappa) \end{pmatrix} + \begin{pmatrix} u_{\text{sensor}} - u_0 \\ v_{\text{sensor}} - v_0 \end{pmatrix} \tag{6.29}$$

and after including equation 6.19 into equation 6.21 the computation of $(x_{\text{theodolite}}, y_{\text{theodolite}}, z_{\text{theodolite}})$ changes to

$$\begin{pmatrix} x_{\text{theodolite}} \\ y_{\text{theodolite}} \\ z_{\text{theodolite}} \end{pmatrix} = \mathbf{R} \begin{pmatrix} 1 & -\omega & \varphi \\ -\varphi & 0 & 1 \\ 1 & -\omega & \varphi \end{pmatrix} + \alpha \begin{pmatrix} c \\ u \\ -v \end{pmatrix} \tag{6.30}$$

It is important to mention that the angles φ and ω are approximated. This is because of the assumption only working with small rotations. Furthermore, because the OAC of the Leica MS60 is used, the factor α does not depend on the distance between camera and telescope centre. The downside using the OAC is that the calibration parameters change due to the varying focus position of the telescope. Therefore, corresponding modelling of these changes is necessary (Ehrhart, 2017, pp. 191-192).

Table 6.4: Estimated calibration for the OAC of the Leica MS60 (Ehrhart, 2017, p.203)

Description	Symbol	Value
Camera constant	c [px]	105029 ± 4
Rotation of image sensor about sighting (principle) axis	κ [mgon]	-21.0 ± 0.7
Rotation angles describing non-parallelism of principle axis to collimation axis	φ, ω [mgon]	$-4 \pm$ n.a.; $-3 \pm$ n.a.
First coefficient of radial distortion	$K1$ [px^{-2}]	$-5.8^{-10} \pm 0.4 \mathrm{e}^{-10}$
Principle point (left→right) [px]	u_0 [px]	1280.0 ± 0.1
Principle point (top→bottom) [px]	v_0 [px]	961.5 ± 0.1

6.3.3   Set of Videos

The data evaluation of the SoV data is similar to the evaluation routine of the SoI data in the previous chapter. Again, data obtained from images can be compared with the read angle data. However based on the measurement process, the order of performing different computations steps varies, as shown in figure 6.16.
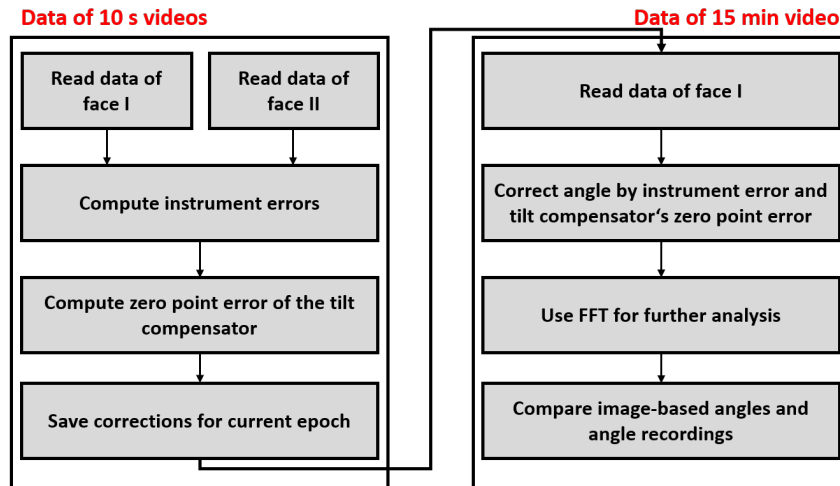
Figure 6.16: Chart of the SoV data evaluation process

The evaluation procedure goes along with the idea, to combine the data from the 10 seconds recordings in both faces for the computation of instrument errors and zero-point errors and afterwards correct the measurements of the 15 minute sequences.

6.3.3.1   Angle encoder readings

The following section handles the evaluation of the dynamic angle measurements. Based on the measurement procedure described in section 6.2.4 Hz and V can be written as

$$
\begin{aligned}
\mathrm{Hz}_{\mathrm{GetAngle}} &= \mathrm{Hz}_{\mathrm{encoder}} + \mathrm{Ci} \cdot \cot(\mathrm{V}_{\mathrm{GetAngle}}) \\
\mathrm{V}_{\mathrm{GetAngle}} &= \mathrm{V}_{\mathrm{encoder}} + \mathrm{Li}.
\end{aligned}
\tag{6.31}
$$

Evaluation of 10 second videos recorded in both faces
The first step is the computation of systematic errors, which might have an impact on the measurements of the 15 min sequences. Therefore, at the beginning of each epoch two data sets of 10 sec are recorded. Similar to the evaluation routine of the RTS data, it is possible to combine those in terms of computing face averages, like in equation 6.1. Especially the instrument errors and the zero-point-error of the tilt compensator along both axes will have an impact on the data evaluation of the 15 minutes video sequences, computed like in equation 6.2.

Evaluation of 15 minute video recorded in face I
One issue, which appears when measuring only in one face, is that systematic errors can not be

neglected in contrast to averaging measurements in both faces. Following quantities, inter alia, affect a measurement in one face:

- Instrument errors ϵ_{coll}, ϵ_{tilt}, ϵ_{index}

- Zero-point-errors of tilt compensator ϵ_{Li}, ϵ_{Ci}

Influences, which cannot be cancelled out via face averaging, are the inclination Li and Ci based on the fact, that a tilted setup cannot be corrected by a two-face measurement (Deumlich and Staiger, 2002, p. 209). For better understanding, in figure 6.17 a schematic drawing is shown and how e.g. the vertical angle is influenced. In the end, the corrected angle readings can be written as

$$
\begin{aligned}
\text{Hz}_{\text{GetAngle},*} &= \text{Hz}_{\text{encoder}} + (\text{Ci} - \epsilon_{\text{Li}}) \cdot \cot(V) + f(\epsilon_{\text{coll}}) + f(\epsilon_{\text{tilt}}) \\
V_{\text{GetAngle},*} &= V_{\text{encoder}} + \text{Li} - \epsilon_{\text{Li}} + \epsilon_{\text{index}},
\end{aligned}
\tag{6.32}
$$

where

$$
\begin{aligned}
f(\epsilon_{\text{coll}}) &= \frac{\epsilon_{\text{coll}}}{\sin(V)} \\
f(\epsilon_{\text{tilt}}) &= \epsilon_{\text{tilt}} \cot(V) \\
f(\alpha_{\text{across}}) &= \alpha_{\text{across}} \cot(V).
\end{aligned}
\tag{6.33}
$$
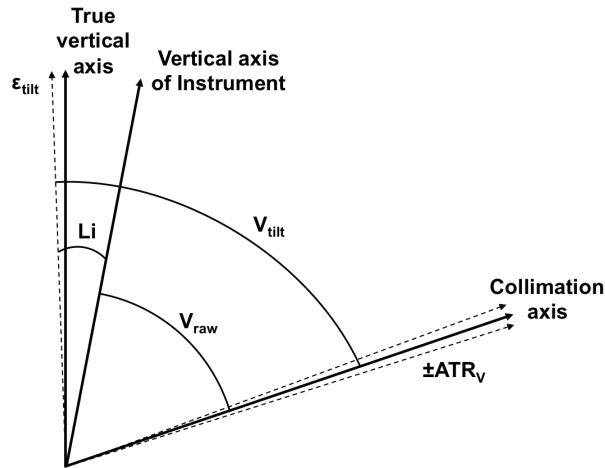
Figure 6.17: Schematic drawing of different effects influencing the vertical angle measurement

6.3.3.2   Image-based evaluation of Set of Videos

The image-based angle results can be written as

$$
\begin{aligned}
\text{Hz}_{\text{Video}} &= \text{Hz}_{\text{GetAngle}} + \arctan\left(\frac{u}{f \cdot \sin(V_{\text{GetAngle}})}\right) \\
V_{\text{Video}} &= V_{\text{GetAngle}} + \frac{v}{f},
\end{aligned}
\tag{6.34}
$$

where f refers to the focal length in pixel. However, the shown equation introduced by Bürki et al. (2010) is only a simplification of the relation between theodolite angles of the IATS and the image coordinates or rather the pixel movements between a reference frame and the current frame.

Further computations are performed with regard to the influence of the refraction change over time, which means that mainly the vertical angle V is of interest. Based on the obtained results, it should be possible to define the effect of the refraction. However, because the image-based angles depend on the angle readings of the encoders, it has to be considered that the data shows similar effects caused by the readings of the angle measurements.

Image-based angle readings

Similar to the angle readings via the GeoCOM interface, the obtained vertical angles from the $10\,\mathrm{sec}$ video sequences are used to compute a combined vertical index error. This quantity includes the telescope's vertical index error $\epsilon_{\mathrm{index,video}}$, the zero-point error of the inclination sensor and finally variations of the image sensor's principle point (Ehrhart, 2017, p.89). As a consequence, this value is used to correct the derived vertical angle from the $15\,\mathrm{min}$ video sequences (shown in equation 6.35). Otherwise its variations would infect the computation of the refraction angle δ.

$$V_{\mathrm{Video}} = V_{\mathrm{GetAngle}} + \frac{v}{f} + \epsilon_{\mathrm{index,video}} \qquad (6.35)$$

Computation of the refraction angle δ

The video sequences capture a widely known aspect, which affects the line of sight. The so-called refraction angle is responsible for bending the sighting axis of the instrument based on the temperature gradients along the path from setup point to target. Based on Ehrhart (2017) a possible approach of describing the refraction angle δ by practical measurements is fed into data acquisition procedure described in figure 6.6 in section 6.2.4.

An approach for the estimation of the refraction angle was introduced by Brunner (1979) and Brunner (2014). Here, the estimation of δ comes from the standard deviation of the angle-of-arrival fluctuations s_δ assuming a turbulent atmosphere. However, the corresponding theoretical framework also presupposes a homogeneous terrain underneath the LOS, which in case of the measurement situation at Wald am Schoberpass does not apply to this condition. Nevertheless, the theory written in Ehrhart (2017) will be seen as sufficient enough. Therefore, the aim of computing the refraction angle δ or rather its change $\Delta\delta$ over time would be useful for correcting the vertical angle to derive the true zenith distance like

$$V_{0,i} = V_i + (\delta_1 + \Delta\delta_i), \qquad (6.36)$$

where δ_1 refers to the first measurement epoch and is declared as a small value. Due to equation 6.36, the computation of the refraction angle's deviations over time should be sufficient enough to distinguish between the movements of the object and influences caused by refraction changes. Consequently, the knowledge of $\Delta\delta$ covers most of the monitoring purposes e.g. computing height

differences based on the trigonometrical approach

$$\Delta h_{0,i} = SD_i \cos(V_{0,i}) + (1-k)\frac{SD_i^2 \sin(V_{0,i})}{2R}.$$ (6.37)

To derive the refraction angle δ, Brunner (1979) proposes to use the standard deviation of the angle-of-arrival s_δ. Therefore, δ can be written as

$$\delta = \delta(s_\delta).$$ (6.38)

s_δ is directly related to the refraction angle because it is measured along the same LOS and furthermore is simultaneously observed with measurements of the vertical angle. Based on the theoretical framework worked out in Ehrhart (2017) the searched quantity δ based on equation 6.38 is rewritten as

$$\delta = -\sin(V^*)\,\frac{\mu}{T}\,\frac{s}{2}\left(A - \frac{W}{z\,k}\,\frac{\varphi_h}{f^{1/2}}\right),$$ (6.39)

where μ and W refer to

$$\mu = 79e^{-6}\,\frac{p}{T}$$
$$W = 0.97\,\text{sign}\,\Theta_*\,s_\delta\,(z\,k)^{1/3}\,D^{1/6}\,T\,\mu^{-1}s)^{-1/2}.$$ (6.40)

V^* and s_V^* refer to the segementwise computed average and corresponding standard deviation based on 2 minute sequences taken from the 15 minute video recordings. The resulting values for s_V^* are used to calculate the standard deviation of the angle-of-arrival fluctuation like

$$s_\delta = \sqrt{s_V^{*2} - \min(s_V^*)^2}.$$ (6.41)

To reduce the IATS's measurement noise and separate it from the standard deviation of the angle-of-arrival fluctuation, the minimum value of all segments of s_V^* is subtracted.
$\text{sign}\,\Theta_*$ presents the sign of the temperature scale depending on whether there are stable atmospheric conditions, like at night, or unstable conditions, like during the day

$$\text{sign}\Theta_* = \begin{cases} +1 & \text{for stable atmospheric conditions} \\ -1 & \text{for unstable atmospheric conditions.} \end{cases}$$ (6.42)

The sign of $\text{sign}\,\Theta_*$ is negative is assumed to be negative, because all of the measurements included in the SoV data set had taken place between 8 o'clock in the morning and 20 o'clock in the evening. After determining the refraction angle δ it should be possible to compute the true vertical angle V_0 like

$$V_0 = V + \delta.$$ (6.43)

6.4 Results and interpretation

In the following section the derived results from all data sets, which have been acquired during the measurement campaign, are shown and discussed. The outcome, whose computation was explained in the further chapter, is used to assess the behaviour of the landslide at Wald am Schoberpass. In the end, it should be possible to evaluate all results and rate the acquisition methods in case that improvements can be proposed for a second measurement campaign.

6.4.1 Meteorological data

The first data, which will be presented, are the recordings of the mobile weather station. Following quantities are presented in figures 6.18 a-e:

- Temperature given in $[°\mathrm{C}]$

- Air pressure given in $[\mathrm{hPa}]$

- Air humidity given in $[\%]$

- Wind velocity given in $[\frac{\mathrm{m}}{\mathrm{s}}]$

- Wind direction given in $[°]$

Based on these observations it is possible to get an idea of the changes, which happened during the whole measurement campaign at Wald am Schoberpass. Especially the temperature indicates environmental variations throughout the measurements. Like shown in figure 6.18a daily cycles can be seen. The warmest temperature was about $25°\mathrm{C}$, the lowest approximately $0°\mathrm{C}$. In connection with the air humidity, the cooling and warming phases can be perfectly described. A better overview can be taken from table 6.5, where specific quantities are highlighted.

In figures 6.18d-e the wind velocity and direction are shown. In contrast to the other observations, these quantities suffer from a malfunction of the sensor in the meteo station. However, it is possible to see that there was a maximum velocity of 6 m/s. The direction of the wind changes unpredictably over time and therefore is inconclusive.

(a) Temperature

(b) Air Pressure

(c) Air Humidity

(d) Wind Velocity
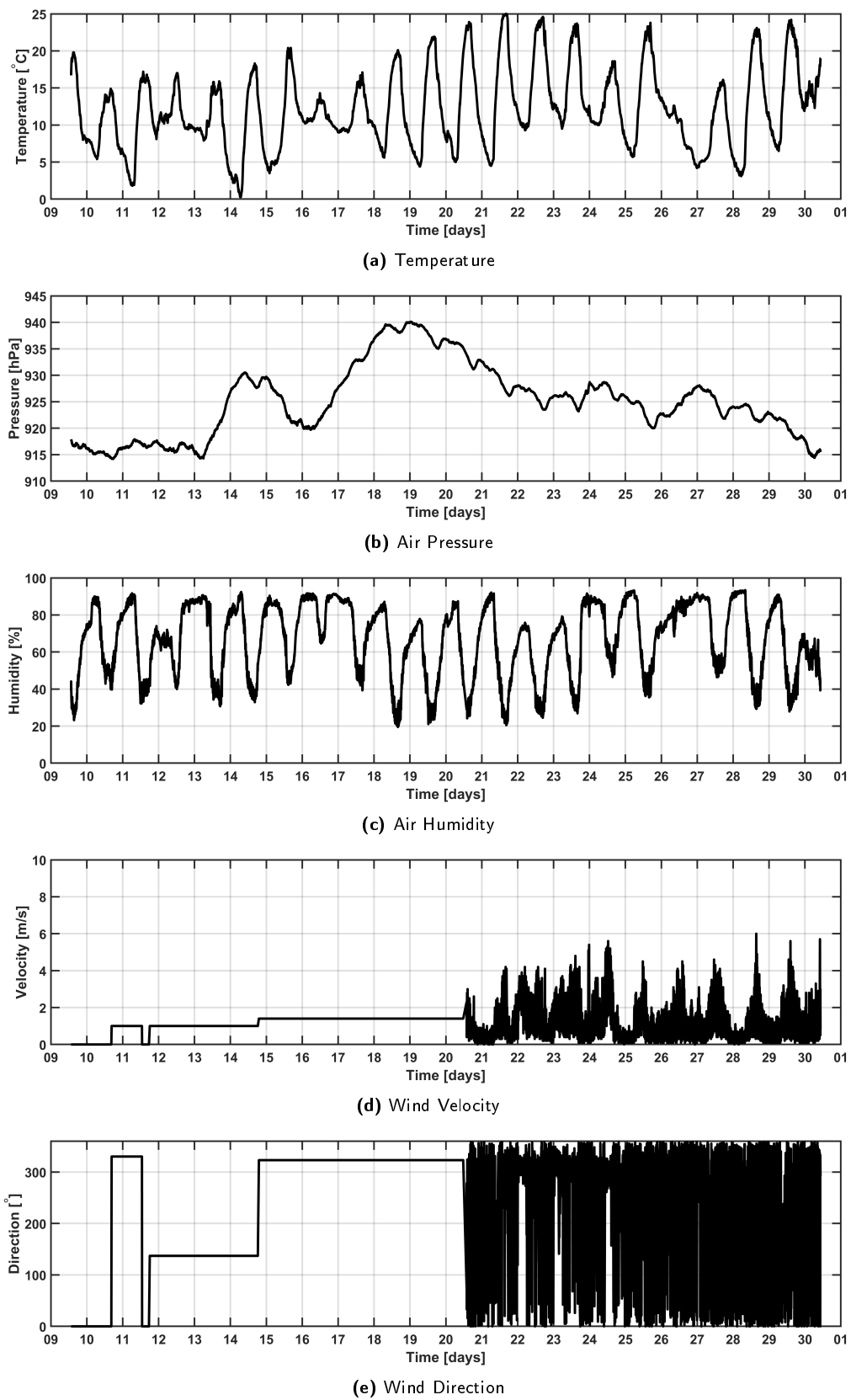
(e) Wind Direction

Figure 6.18: Meteorological data - temperature, air pressure and air humidity averaged wind velocity and direction

Table 6.5: Analytics concerning progress of temperature

$\bar{\text{T}}[^\circ\text{C}]$	max. $\text{T}[^\circ\text{C}]$	min. $\text{T}[^\circ\text{C}]$	Range w.r.t. $\bar{\text{T}}[^\circ\text{C}]$
12.1	25.1	0.3	[-11.8 13.0]

Due to the temperature range of approximately $\pm 12^\circ$C and a roughly assumed change of air pressure of about 25 hPa a first assessment concerning the meteorological distance correction can be announced (Deumlich and Staiger, 2002, p.163) like

$$\pm 1\text{K}(^\circ\text{C}) = 1\text{ppm}$$
$$\pm 3\text{hPa} = 1\text{ppm}.$$
(6.44)

This leads to an estimated variation of about 9 mm when performing a distance measurement of about 400 m.

6.4.2   Robotic Total Station

The main components of the measurements using the Leica MS60 as a RTS are the horizontal angle Hz, vertical angle V, slope distance SD, length inclination Li and cross inclination Ci. These quantities have to be processed for each target. To achieve a better overview some figures show target groups, which are either located in the landslide or the stable area. Furthermore, the results are shown for specific targets at specific epochs and also over the whole period of observation time. Based on the evaluation routine, the first step is to detect false positives in the raw data. Figures 6.19 give an insight into how many measurements are declared as gross errors. Table 6.6 corresponds to the outcome in figure 6.19. Additionally, the total amount of performed measurements is presented, concluding that targets installed in the landslide were measured about four times more often than the reference points.

There is a main difference between the measured quantities when comparing them with each other. For instance, the angle measurements depend on the installed type of each target. Targets 12-15 and 1001-1003, utilizing bireflex targets and refelctives tapes, do not include any gross errors. This is because the angle readings refer to the steering angles, which are introduced by the GeoCOM protocol. For these, no ATR is activated and therefore no fine adjustement is needed. Consequently, a possible orientation drift of the instrument cannot be seen in the corresponding angle data. Despite that, the prism targets 11 and 16, which are also located nearby the setup point, indicate similar problems like the landslide targets.

Comparing Hz and V, it is visible that the vertical angle shows less false positives. All targets, which are defined as steady, do not trouble with any gross errors in V. Taking a look at targets 108 and 109, which have been proven to be the same observation points, the amount of blunders for Hz and SD are similar. This does not apply for V. It is assumed that the sequential order within a set measurement has an impact on the results, because target 109 is measured before 108.

Summarising, Hz seems to be more affected by e.g. atmospheric changes than the other observation quantities, which is also readable in table 6.6. Another aspect is that the measurements recorded in

the first face are more likely to suffer from false observations. This maybe is also a consequence of the defined sequential measurement order.

(a) Horizontal Angle Hz

(b) Vertical Angle V

(c) Slope Distance SD
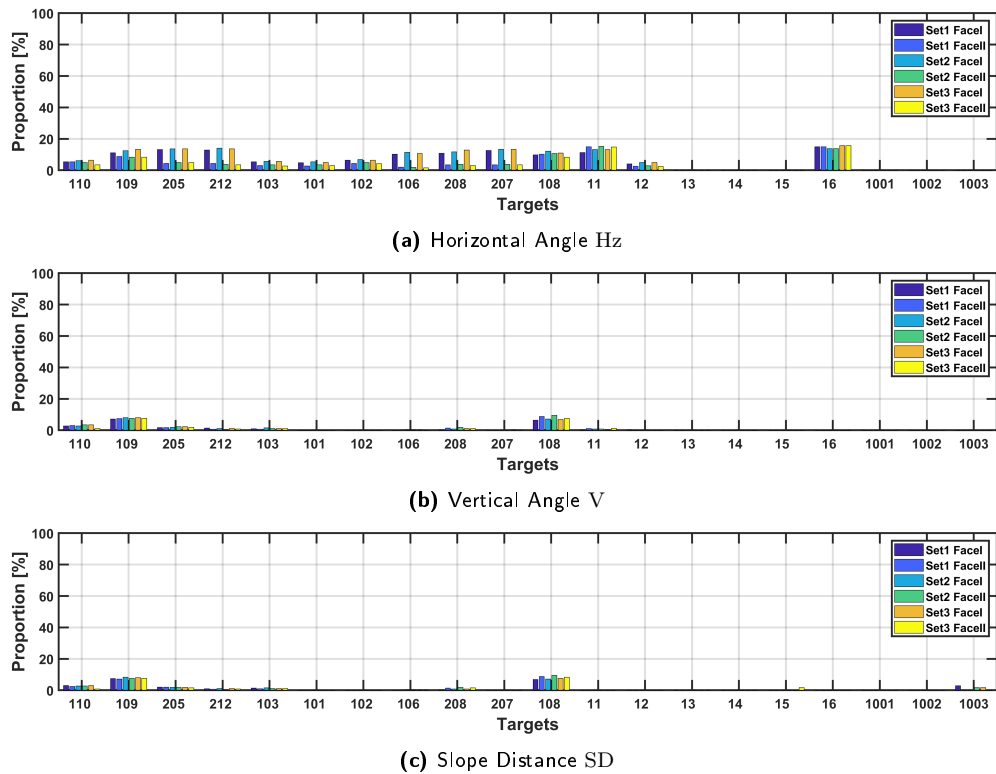
Figure 6.19: Proportion of detected gross errors w.r.t. to the total amount of epochs

Table 6.6: Proprtion of gross errors w.r.t. to the total amout of uncorrected measurements

ID	Type	Area	Epochs	r_{Hz} [%]	r_V [%]	r_{SD} [%]
110	Mini Prism (MP)	Rock Face	295	5.3	2.7	2.4
109	Mini Prism (MP)	Rock Face	295	10.4	7.6	7.7
205	Mini Prism (MP)	Rock Face	295	9.1	1.9	1.9
212	Mini Prism (MP)	Rock Face	295	8.7	0.9	0.9
103	Mini Prism (MP)	Rock Face	295	4.3	1.1	1.2
101	Mini Prism (MP)	Rock Face	295	4.0	0.2	0
102	Mini Prism (MP)	Rock Face	295	5.5	1.1	0
106	Mini Prism (MP)	Rock Face	295	6.3	0.1	0.2
208	Mini Prism (MP)	Rock Face	295	7.6	7.7	1.1
207	Mini Prism (MP)	Rock Face	295	8.3	0.8	0
108	Mini Prism (MP)	Rock Face	295	10.3	0.1	8.0
11	Mini Prism (MP)	Stable Area	274	13.8	0	0
12	Bireflex Target (BRT)	Stable Area	274	3.6	0	0
13	Bireflex Target (BRT)	Stable Area	68	0	0	0
14	Bireflex Target (BRT)	Stable Area	68	0	0	0
15	Bireflex Target (BRT)	Stable Area	68	0	0	0.3
16	Mini Prism (MP)	Stable Area	248	14.8	0	0
1001	Reflective Tape (RM)	Stable Area	68	0	0	0
1002	Reflective Tape (RM)	Stable Area	68	0	0	0
1003	Bireflex Target (BRT)	Stable Area	68	0	0	1.1

Filtered data sets

Based on the the filtered data sets, the results of target 101 are shown in figures 6.20 a-c. Here, different aspects are visible. First of all, the horizontal angle shows a drift progressing until the 24th of April. Additionally, between the 19th and 20th of April only one set measurement is available. After the 24th of April the time series shows a gap and afterwards an offset compared to the former behaviour. The gap can be traced to a dismantling of the Leica MS60 during the campaign because of another measurement project of the IGMS. Nevertheless, the difference between the last data point of the 24th and the first data point of the 26th of April is approximately 120 cc. One reason obviously is the new fixing procedure when setting up the Leica MS60.

Based on the absolute inclination visualized in figure 6.21, the correction of the tilt compensator increases up to 100 cc across and approximately up to 300 cc along the instrument's axes. According to these two indicators, the whole measurement system tilts. Additionally, L_i shows daily variations of at least 100 cc a day.

(a) Unreduced horizontal angle Hz

(b) Vertical angle V

(c) Meteorological corrected slope distance $\mathrm{SD_m}$
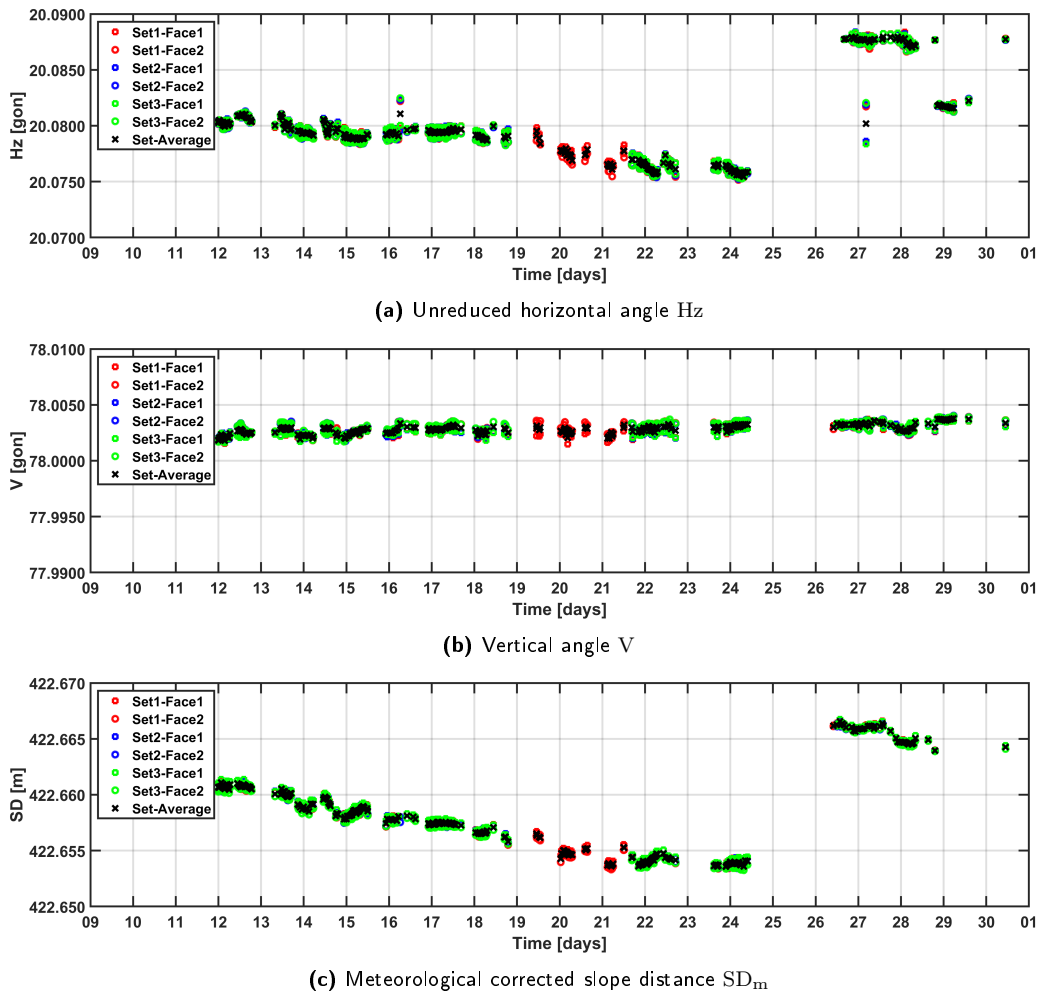
Figure 6.20: Times series of the observations Hz, V and $\mathrm{SD_m}$ of target 101(MP)
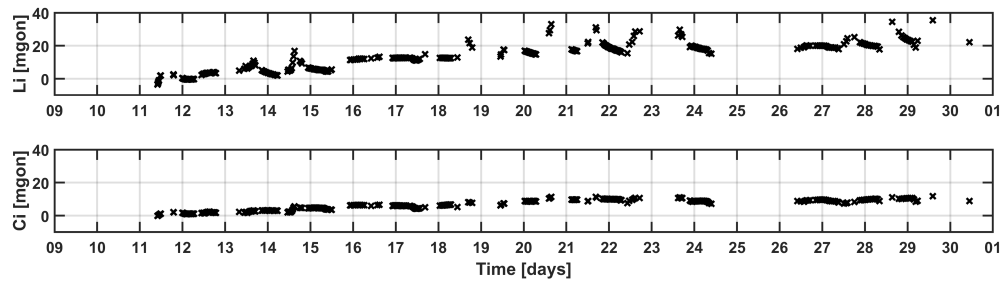
Figure 6.21: Time series of the offset corrected tilt compensator readings in both axes. Computing the absolute inclination based on both face readings, the zero point error of the tilt compensator vanishes.

Based on the recorded meteorological data it is possible to compute the referring meteorological distance correction for the EDM measurement. The range of $\Delta \mathrm{SD_m}$ is about 5 to 15 mm. The maximum corresponds to the warmest temperature measured by the mobile weather station.

Considering the meteorological distance correction it is possible to compute the changes along the LOS. The deformations across the LOS are mainly determined by the angular readings. These components in terms of aiming at the targets are more informative compared to the coordinate computation based on the first geodetic task. Additionally, the height component based on an assumption for the refraction coefficient $\mathrm{k} = 0.13$ is also visualized in figure 6.22. As mentioned in the previous chapter 6.3.1 the changes along the LOS correspond to the variations of the distance measurement. Moreover, the component across the LOS clearly shows the same behaviour like the horizontal angle measurement. In contrast to this, the height coordinate does not show any kind of variations, which of course is possible due to the assumption of a continuous uniform refraction coefficient and the to some extent constant progress of the vertical angle.
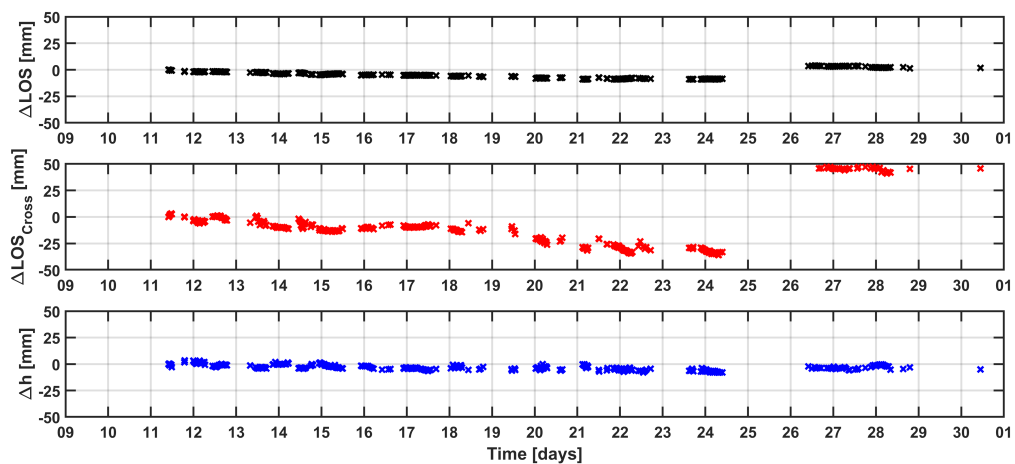
Figure 6.22: Comparison of the components concerning height, along and across the line-of-sight

To visualize the single quantities in dependency of each other, figure 6.23 shows a 2-dimensional deformation plot including the components along and across the LOS. The crosses going from darker to lighter blue show the temporal progress. Based on the gained knowledge concerning the deviations of the horizontal angle and the distance, the motion of target 101 indicates, that the landslide was

83

subject to a deformation process. However, the motion itself does not really comply to the results of other installed sensors like the laser scanner. For instance, the lateral drift does not make sense and therefore has to be an artefact of the horizontal angle readings based on the ATR.
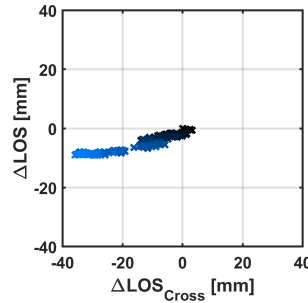
Figure 6.23: Deformation plot of target 101 based on the components along and across the LOS

Declaring the orientation problem of the instrument, the idea is to rectify this issue. One possibility is to recalculate the angles based on a new reference direction. One target, which seems to be suitable enough, is the target 16 in the stable area. To show the impact of changing the reference direction, figures 6.24a and b show the angle differences w.r.t. the first epoch. The second one though is more stable, however there are still daily events, which can not be smoothed.

(a) Unrectified Hz

(b) Rectified Hz
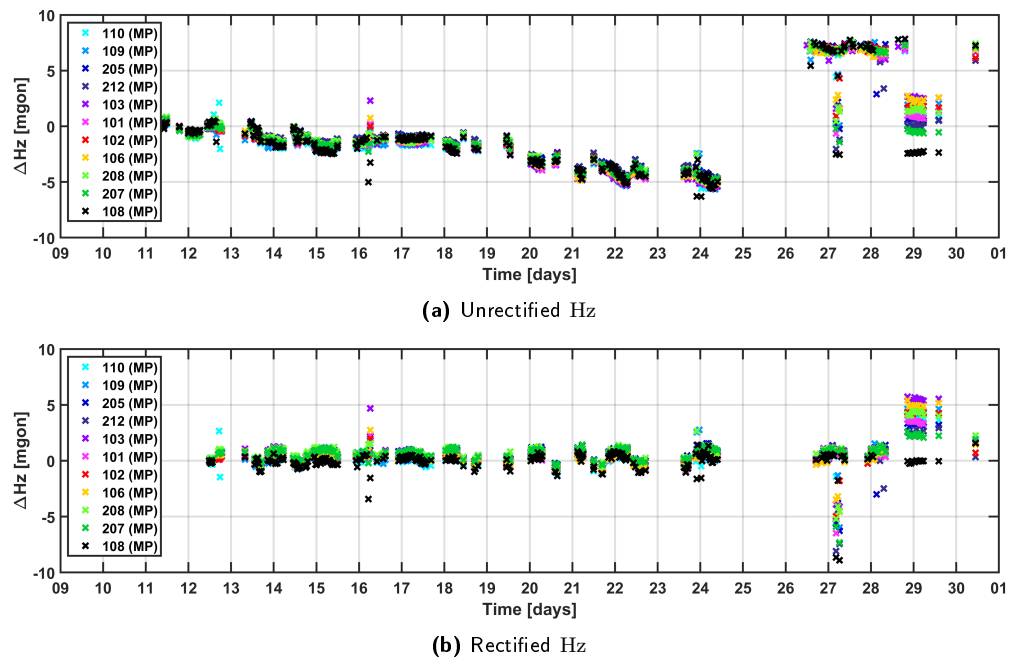
Figure 6.24: Differences of Hz w.r.t. to the reference epoch concerning all targets located in the landslide of Wald am Schoberpass

After recalculating the horizontal angle, it is again possible to compute the changes along and across the LOS. This time the influence of the horizontal angle is mostly eradicated and only the change of the distance measurement seems to cause a variation. Especially the brighter coloured group does not fit to the others, however these measurements were taken after the 25th of April. Here the slope

distance shows a significant variation.
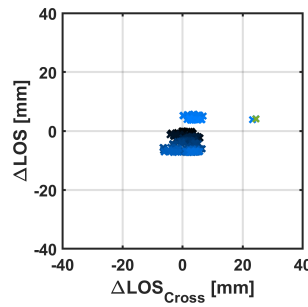
Figure 6.25: Deformation plot of target 101 visualizing the components along and across the LOS after reducing Hz

The results shown so far are mainly covering the measurements taken to the targets located in the landslide. On the contrary, the behaviour of the points in the stable area also have to be considered. In figure 6.26a-c the deviations of Hz, V and SD w.r.t. the first epoch are presented. The horizontal angle shows various behaviours. It is important to highlight, that the targets 11 and 16 are prisms. Here, the ATR position refinment is activated. On the other hand, the angular observations of the bireflex targets and reflective tapes only rely on the defined steering angle. For better understanding, in 6.26a-c different markers are utilized. ATR based measurements are highlighted as crosses, angular readings based on the given steering angle as circles.

As assumed when describing the outlier detection, targets 12-15 and 1001-1003 do not show any change in Hz or V. The only variations are caused by the position settings of the telescope's engine drive. In contrast to that, targets 11 and 16 suffer from daily variations. Target 16 behaves similar to the ones in the landslide. However, target 11 shows unpredictable jumps. It is assumed, that the fixing for this point, a wooden peg in the grass, was not stable enough.

(a) Horizontal Angle Hz

(b) Vertical Angle V

(c) Slope Distance SD
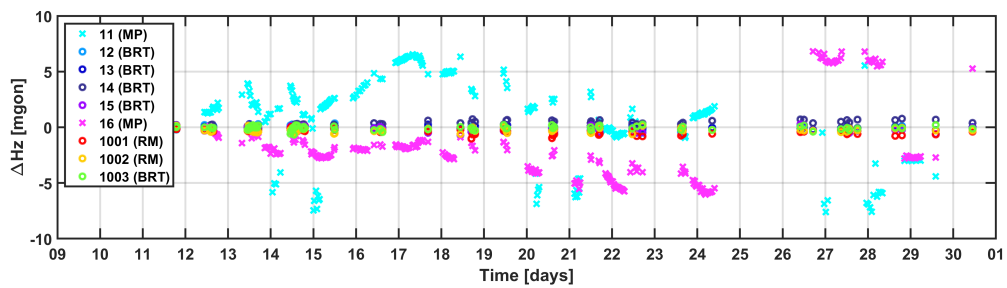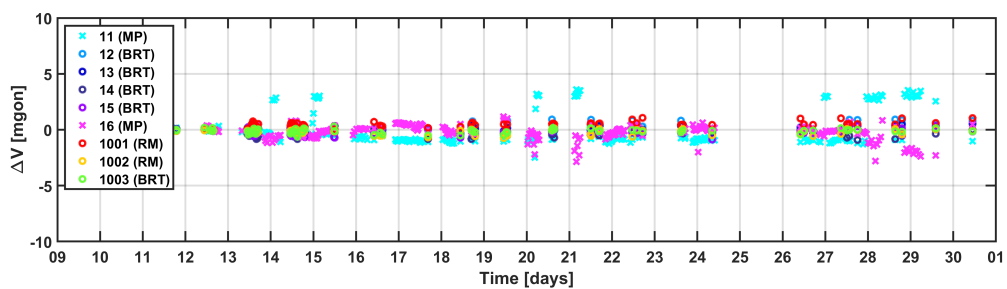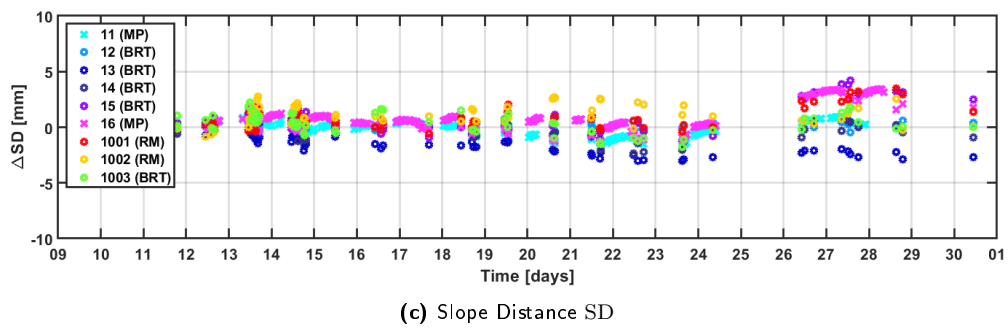
Figure 6.26: Differences of the observations Hz, V and SD w.r.t. the first epoch concerning all targets of the stable area

Summarising, based the results obtained by classical geodetic data (angles, distances, inclination) it can be concluded that the landslide did not show any significant deformation. The visible variations in the each observation quantity can traced back to the behaviour of the setup point. The recorded absolute inclinations of Ci and Li indicate that the stability of the Leica MS60 suffered from physical change of the concrete wall, where the instrument was installed on. Here, the simple relation written as $\frac{\Delta SD[m]}{\Delta Li[rad]}$ gives information whether the instrument tilted or the whole setup, as depicted in figure 6.27. Assuming physical change of the EDM's zero point of around 7 mm (ΔSD) due to the tilting of approximately 30 mgon (ΔLi), the corresponding height difference equals around 1.5 m, which would refer to the height of the whole setup.
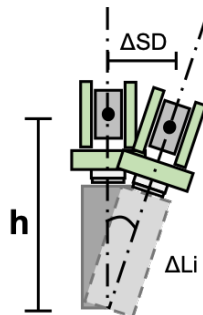
Figure 6.27: Schematic to show the consequences of a tilting setup.

6.4.3   Set of Images

The main component of the measurements using the Leica MS60 as an image-assisted total station is next to the horizontal angle Hz, vertical angle V, slope distance SD, length inclination Li and cross inclination Ci also the ability of taking images. As already mentioned in chapter 6.3.2, the results correspond to the evaluation process. The first step is implementing the feature matching algorithm resulting in pixel differences and the second one is to compute angle deviations based on these image-based changes.

6.4.3.1   Feature Matching

The feature matching process is the first step to evaluate the taken images from Wald am Schoberpass. As already explained, for each target in every measurement epoch the image registration was performed to find corresponding feature points to draw conclusions regarding the behaviour of two scenes. The first conclusion, which can be drawn, is that the amount of detectable features with an approximate range of 5000-15000 features decreases with further progress. A very likely explanation is that the differences between the reference image and the second image increase because of changing vegetation and exposure conditions. As a consequence, also the number of matched feature points dwindles, shown in figure 6.28. For the sake of completeness, all so far known influences are listed as follows

- Background
  - Vegetation
  - Scree

- Exposure
  - Position of the sun
  - Clouds

- Image quality
  - False focus
  - Blurred images (shown in figure 6.29)
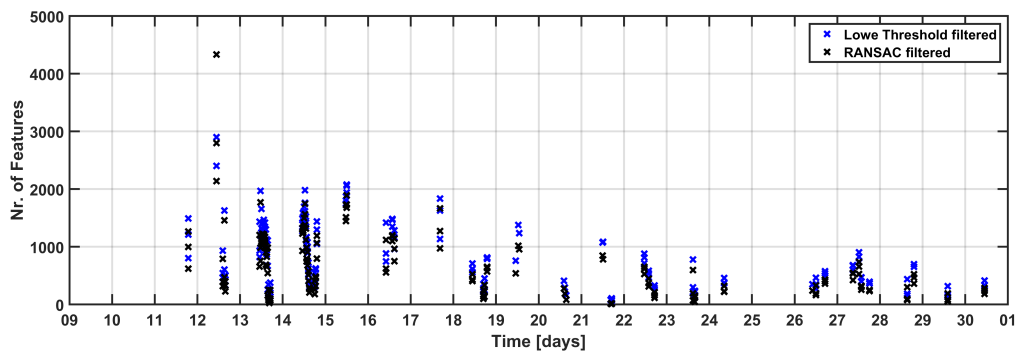
Figure 6.28: Number of detected feature points after adpating Lowe's threshold and the RANSAC algorithm

Figure 6.29: Example for bad image comparison. The second picture is heavily blurred.

A further issue is the receivable precision of the computed pixel differences. Based on the detection of mismatches and the assumption that all feature points move along the same direction, the scattering of the pixel differences should be quite small. In figure 6.30 the standard deviation of the computed pixel differences is shown in contrast to the amount of good features. Even when dealing with a lower number, the standard deviation is considerably stable.

The first consideration when looking on the pixel deviations suggests that the amount of detected features has an impact on the outcome, as shown in figure 6.31. Dealing with a total amount of up to 500 features, there is a distinctive offset in the pixel deviations. However, it is important to link this behaviour to the knowledge gained in chapter 6.4.2. The progress of u and v is similar to the one of Hz and V. Both horizontal components u and Hz suffer from the dismanteling of the instrument after the 24th of April. For rough estimations, one pixel refers to approximately 0.6 mgon. This is based on the camera calibration obtained by Ehrhart and Lienhart (2015b). Consequently, a difference of 12 px equals 7 mgon, which is similar to the result of Hz depicted in figure 6.24a.
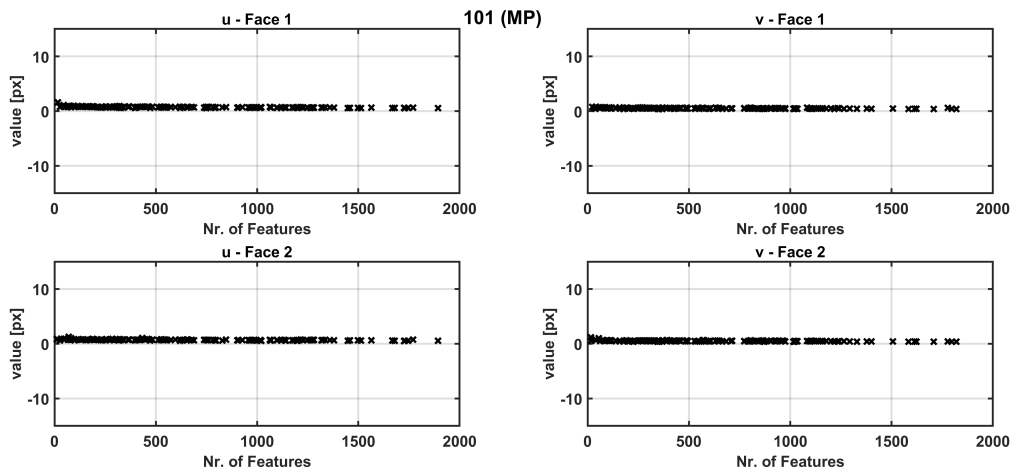
Figure 6.30: Number of features in contrast to the achievable standard deviation
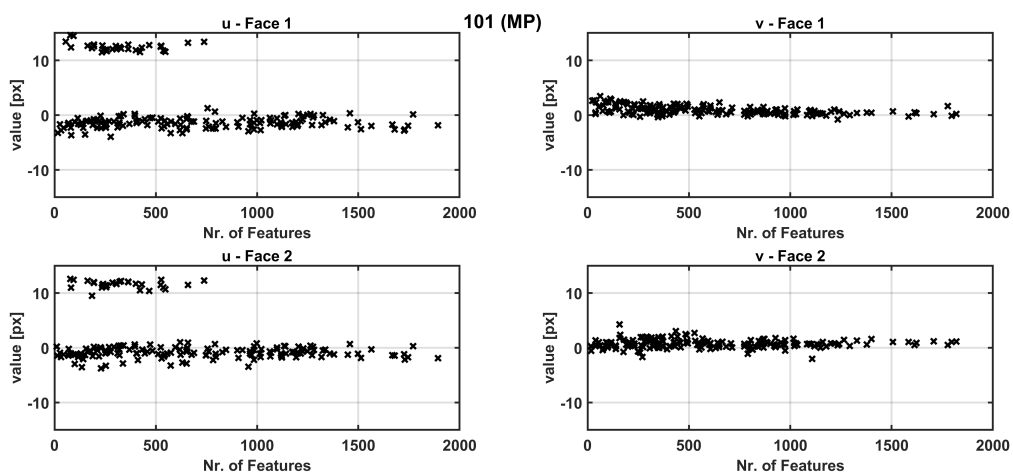
Figure 6.31: Number of features in contrast to the pixel deviation

6.4.3.2   Transformation from pixel differences to angle deviations

The following results originate from the transformation process computing angle deviations from pixel differences, like described in chapter 6.3.2. In figure 6.32a-b a comparison is shown between the outcomes of image-based and ATR based angles. The depicted data sets for Hz refer to the reduced horizontal angles w.r.t. target 16. The frequency of image-based data is quite low, which makes a comparison difficult. Nevertheless, when there has been an epoch, where images have been taken, the derived results seem to fit. The differences between both processed data sets are computed and depicted in figure 6.33. Here, the vertical angle shows distinctive deviations for the targets targets 106 (yellow) and 110 (turquoise) of approximately $\pm$4-5 mgon.

(a) Horizontal angle Hz

(b) Vertical angle V
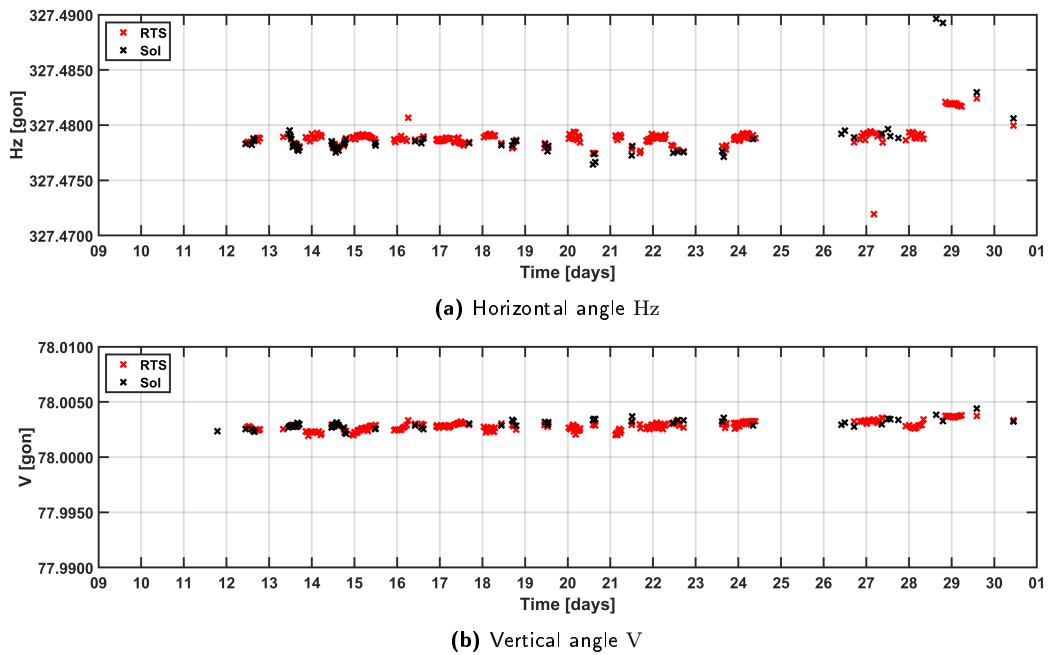
Figure 6.32: Comparison of Hz and V based on the RTS and Sol data sets, shown for target 101 (MP)
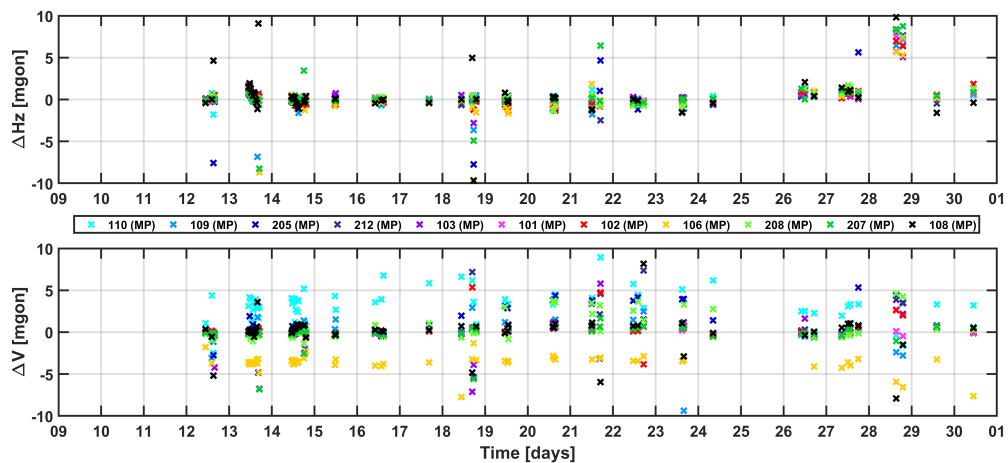
Figure 6.33: Differences between the data sets of Sol and RTS

Having a look at the elevation profile in figure 6.34, one possible reason could be the measuring geometry. Based on the red and blue lines, the mean differences of V and Hz are visualized. The vertical component clearly shows a relation between the targets and their locations. In figure 6.35 the displacement vectors, which originate from detected feature points, show a distinctive alignment and scaling. Consequently, the orientation of the telescope camera does not match the same position as the captured reference image. It is assumed that the position refinement based on the ATR mode causes this variations. According to Leica-Geosystems (2008), the fine adjustment mathematically corrects the angle reading when the ATR deviations are within a threshold of about 5 mgon. Otherwise, the motorization again aligns the telescope, which has to be done when aiming at targets 106 and 110. This newly performed position setting is assumed to be responsible for the deviations in V.
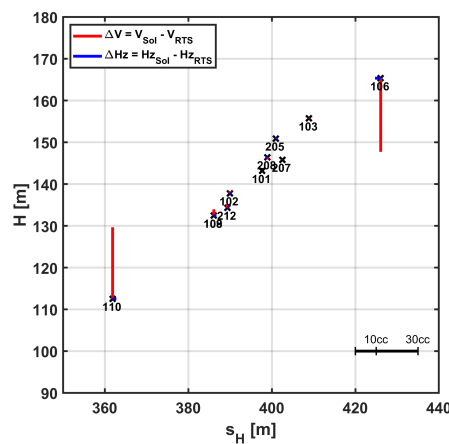
Figure 6.34: Elevation profile of targets in landslide showing mean differences between the results originating from the Sol and RTS data set
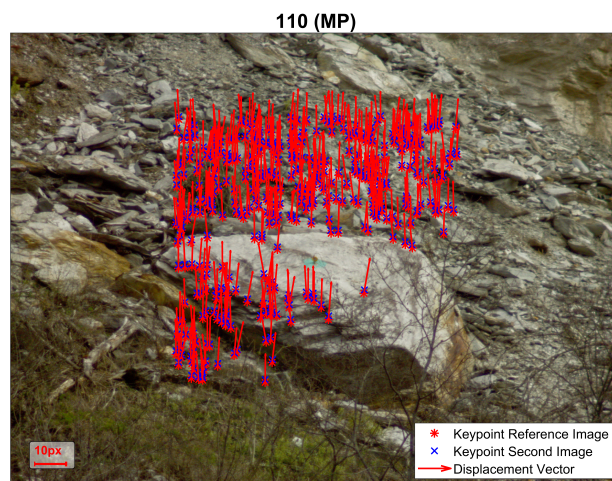
Figure 6.35: Deformation vectors between two different images taken from target 110. Here, the varying telescope alignments of the two images cause significantly high pixel deviations along the vertical axis

Summarising, the image-based observations recorded at Wald am Schoberpass describe the same behaviour as the results from the RTS data sets. The image analysis based on the SIFT algorithm and FLANN based matcher computes features, which can be used to describe the change w.r.t. a reference image. The total amount of matched feature points decreases as a result of changing vegetation. Additionally, the image quality is affected by altering illumination.

The final comparison of the angle readings based on images and ATR yields that there are target depending differences. These are assumed to refer to the steering and correction process of the ATR fine adjustment. Knowing this issue, it can be stated that the image based approach works in terms of repeatability. Nevertheless, a consistent image recording procedure and a exposure control are problems which have to be considered and solved for further monitoring applications.

6.4.4   Set of Videos

The results of the data obtained by the SoV should mainly cover the purposes of dynamic deformation monitoring. As presented in current state-of-the-art applications, where inter alia the Leica MS60 was used, vibration measurements based on the use of the OAC are possible. Seen in the context of Wald am Schoberpass, one of the main goals was to derive knowledge about the influence of the air fluctuation, rephrasing the refraction angle δ.

6.4.4.1   Comparison of the angle measurements and image-based results

The measurement procedure introduced in section 6.2.4, is schmetically presented in figure 6.36.
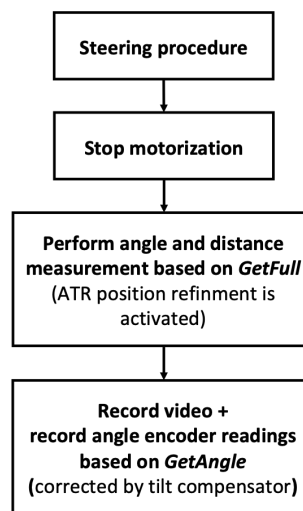
Figure 6.36: Schematic to explain the basic procedure when recording SoV data

Based on the presented implementation, the angle measurements, which are simultaneously recorded next to the video, are corrected by inclination measurements of the tilt compensator. Consequently, the tilt corrected angle observations are the basis for the computation of the image-based angle measurements. In figure 6.37 one day is taken as an example to depict the recorded data. Furthermore, the averaged 2 minute sequences are shown. The angle measurements, which are only corrected by

the tilt compensator, show a deterministic effect for almost all epochs measured on this day. Here, it seems that the angles significantly changed during the 15 minute videos. Especially the data set, depicted in the zoomed window, shows an increase for V of approximately 1.5 mgon. Taking a look at the average values of the 2 minute sequences, the image-based results compensate the drifting of the angle measurements.
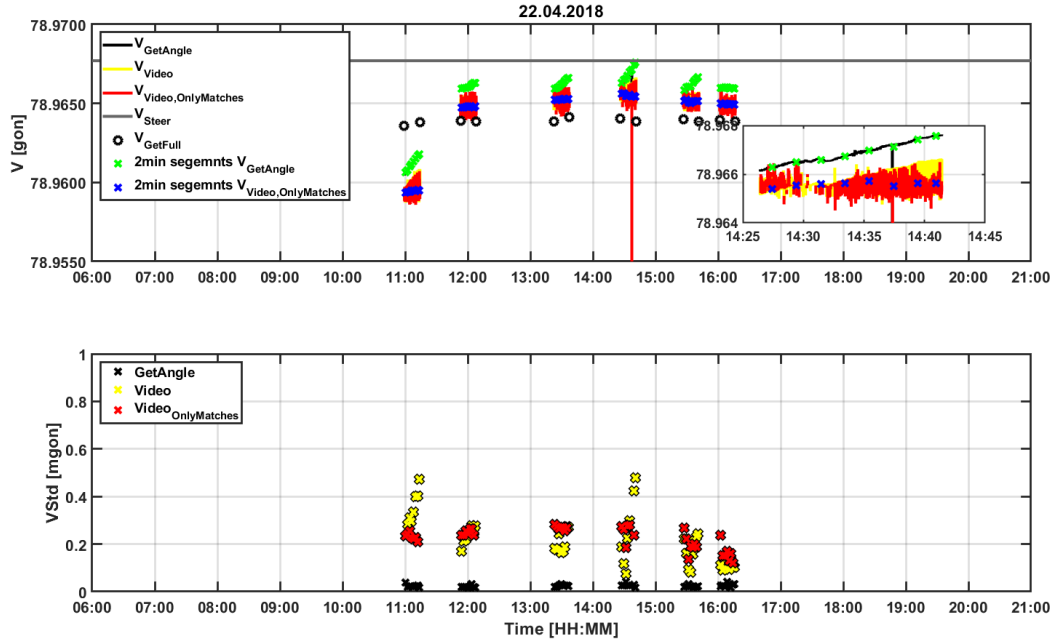
Figure 6.37: Deformation vectors between two different images taken from target 110. Here, the varying telescope alignments of the two images cause significantly high pixel deviations along the vertical axis

Different reason can be formulated for finding an explanation for the drifting of the vertical angle. Therefore, the GetAngle GeoCOM request is analysed. The referring vertical angle reading can be written as

$$V_{GetAngle} = V_{encoder} + Li. \tag{6.45}$$

Based on this equation, three different aspect can be helded as responsible:

1. The instrument tilts
   $\rightarrow V_{encoder} = const. \rightarrow Li$ changes

2. The telescope tilts
   $\rightarrow V_{encoder}$ changes $\rightarrow Li = const.$

3. The tilt compensator drifts
   $\rightarrow V_{encoder} = const. \rightarrow Li$ changes

4. Combination of variants 1.,2. and 3.

For better evaluation, the data from the zoomed window of figure 6.37 is taken as an example. The deviations for the single face readings of the longitudinal inclination Li and the vertical angle V are

congruent. Consequently, subtracting Li from V the differences scatter around zero. Based on this calculation, the first variant applies for the discussed tilting issue. It seems, that the angle readings remain constant however the tilt compensator measures a continuous change.
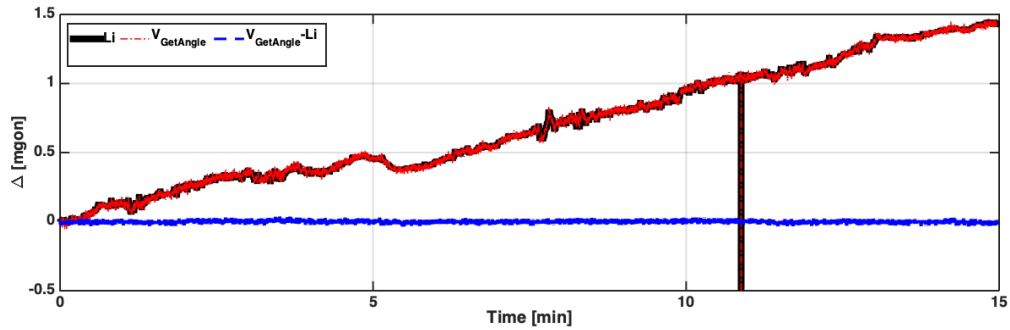
Figure 6.38: Change of Li and $\mathrm{V_{GetAngle}}$ compared to describe the tilting seen in the raw data

Therefore, when taking the video of one specific epoch into account, it is visible that the framed scene changes with further duration of the video and moves upwards, as depicted in figure 6.39. Computing the features points between the first and the last frame of the referring video sequence, a pixel movement of approximately 2 px is measurable. The equivalent would be approximately 1.2 mgon, which refers to the change of $\mathrm{V_{GetAngle}}$.
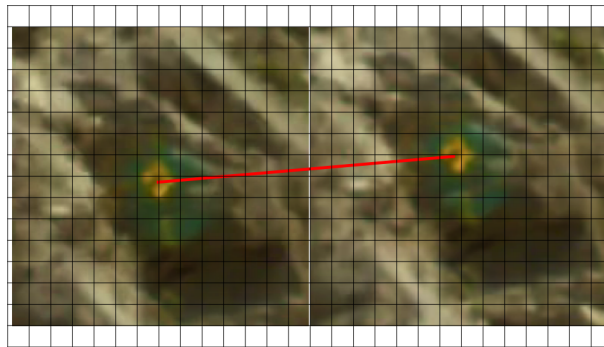
Figure 6.39: Visualization of the first (left) and last (right) frame of a video sequence showing a changed field of view

As proclaimed in section 6.3.3, the standard deviation of the image-based angle measurements is important for the determination of the refraction angle δ. Here, it is absolutely necessary to check whether the feature matching algorithm is able to detect features between the current and reference frame or not. Otherwise, the image-based observations would be wrongly affected by pure angle measurements based on the *GetAngle* GeoCOM request (yellow data in figure 6.37). Therefore, only image-based angle measurements are at the core of interest, where the feature matching algorithm is able to detect similar features between two comparable frames (red data in figure 6.37). However, this computation strongly depends on the image quality of the video, which, in case of the recording situation and video resolution, suffers from blurring.

The depicted outcome for the refraction angle depends on the results of $\mathrm{V_{Video,OnlyMatches}}$ including only successful feature matching processing. This circumvents the drifting behaviour of $\mathrm{V_{Video}}$. The

amplitude of the refraction angle is beneath the angle precision, however the outcome has to be doubted, because parts of the environmental influences such as grass height are roughly estimated or terms in the underlying theoretical framework are unified or excluded, like for instance the impact of the wind.

(a) Refraction angle vs. time

(b) Refraction angle vs. ambient temperature
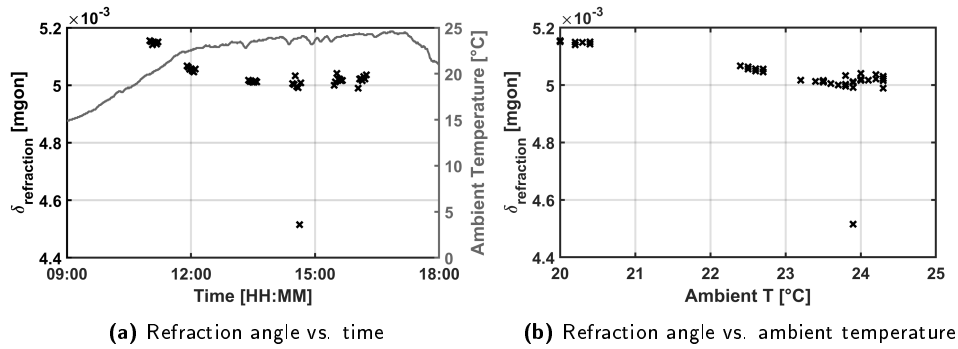
Figure 6.40: Computed refraction angle δ showing same deterministic behaviour such as the standard deviation of V_{Video}

The stability of the Leica MS60 is a major problem during the dynamic measurements. During the entire measurement campaign the inclination observations show a continuously change of absolute inclinations of Ci and Li. Furthermore, the zero point errors ϵ_{Ci} and ϵ_{Li} depicted in figure 6.42 indicate at least daily variations.
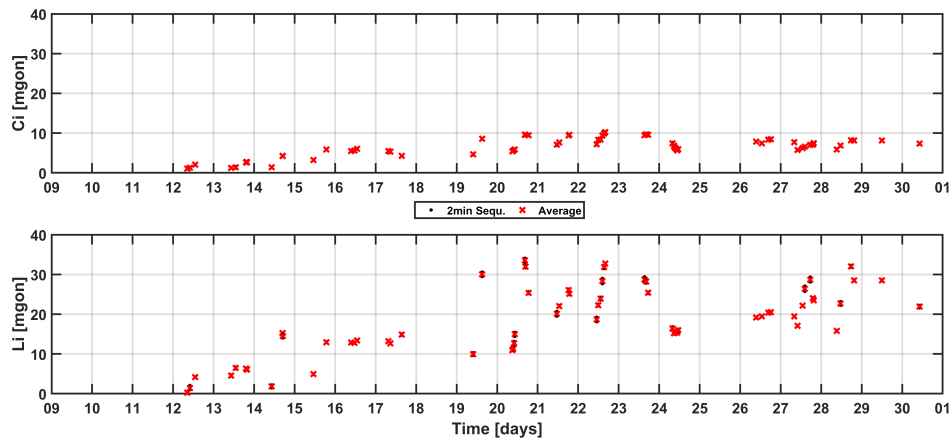
Figure 6.41: Absolute inclination measurements for both transversal and longitudinal axes from the 15 minute recordings
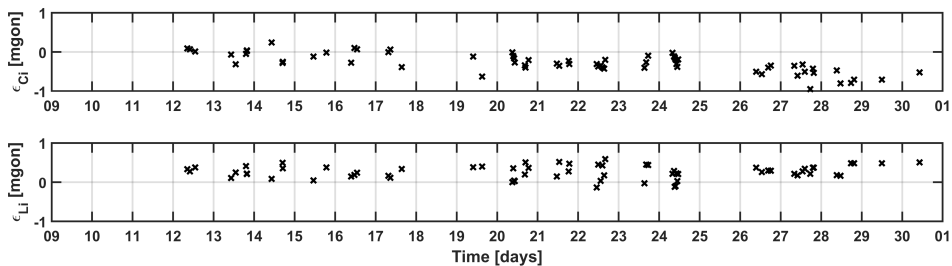
Figure 6.42: Computed zero-point errors of the inclination sensor in both axes

94

Another aspect, which is also visible in figure 6.37, is the difference between angle measurements, which have been taken based on different GeoCOM requests. *GetFull* and *GetAngle* are two different ways to perform an angle measurement. The angle readings based on the *GetFull* request are corrected by the ATR fine adjustment. Having this in mind, figure 6.43 shows the derived data for the different approaches of angle measurement. The referring differences are depicted in figure 6.44. As proclaimed in chapter 4, the steering process is based on the ATR fine adjustment, where a insufficient position alignment of the telescope is compensated. The mentioned threshold of 5 mgon (section 4.2) is hardly exceeded.

Additionally to the differences in the angle acquisition, $\mathrm{Hz_{GetAngle}}$ shows three different phases during the measurement campaign, which does not necessarily relates to $\mathrm{Hz_{GetFull}}$. The first one, going from the 12th of April to the 17th of April, shows a rather steady behaviour with a maximum deviation of about 10 cc. The second one, taking place from the 19th to the 24th April, is mainly showing a drift of approximately 60 cc. Here, it has to be mentioned, that during these days the hottest stages were reached for the measurement campaign. The third one is already known from the RTS results, where after dismantling and reinstalling the Leica MS60, a significant orientation offset overlays the observed data, however similar to the first interval shows a steady progress of the measurements.

(a) Comparison of Hz

(b) Comparison of V
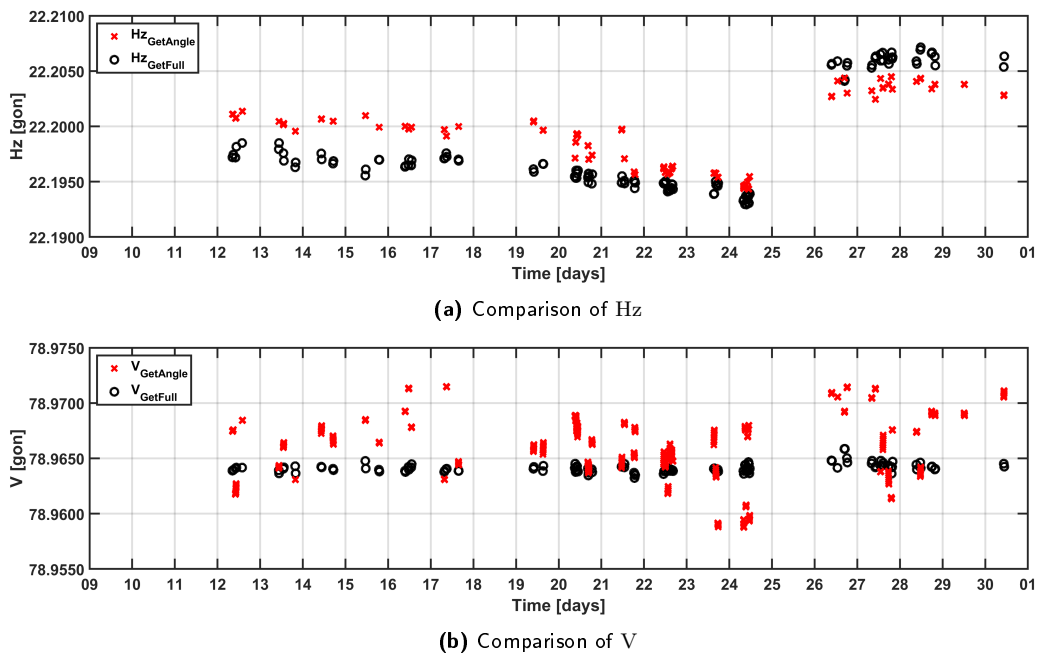
Figure 6.43: The *GetFull* command provides ATR corrected angles, the *GetAngle* command without prism lock only considers the tilt compensator's measurements

(a) Comparison of ΔHz

(b) Comparison of ΔV
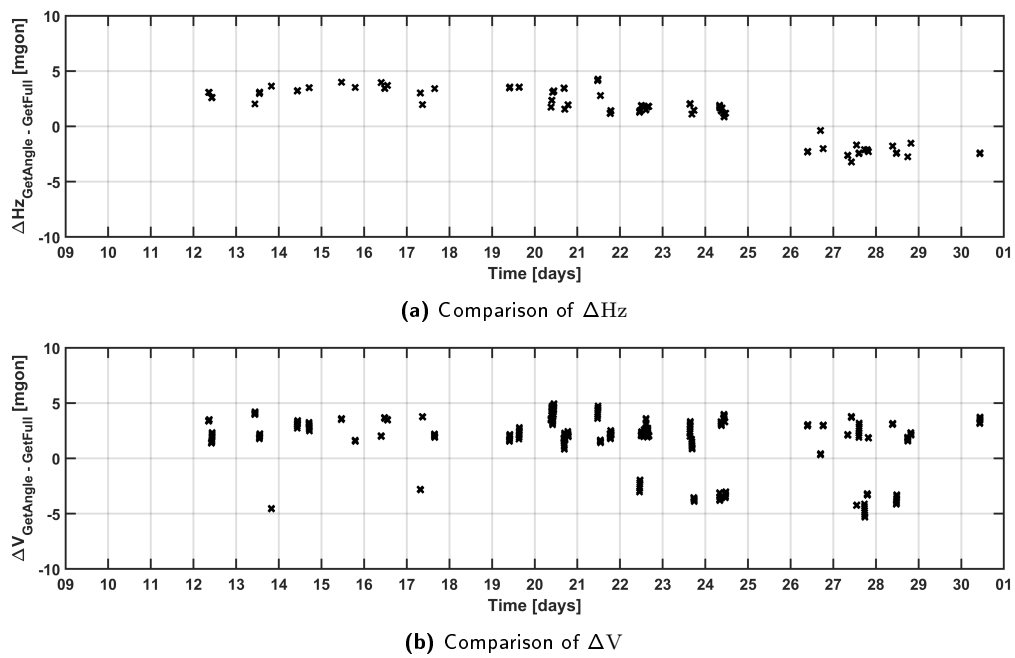
Figure 6.44: Differences between the angle measurements derived by using the *GetFull GetAngle* command.

6.5 Summary and conclusion of the measurement campaign at Wald am Schoberpass

The aim of the measurement campaign was to get information about the behaviour of the landslide at Wald am Schoberpass. Therefore, different sensor systems have been used to assure valid results for evaluation. For this thesis, the main sensor is the Leica MS60 used as both, RTS and IATS to derive images and videos besides angle and distance measurements. Based on these types of observation, different targets have been measured during each epoch performing set measurements in both faces. As a consequence of their locations, it is possible to gather these into two groups, one located in the landslide, the others are spread close around the setup point and therefore are seen as stable.

All together, one set normally includes 20 targets. All points located in the landslide are installed via mini prisms, most of the stable points utilise reflector tapes or bi-reflex targets. Based on these reflector types, the steering or rather aiming routine varies, which is based on the GeoCOM requests. Here some aspects are given, which has to be considered when dealing with altering target types

- Specific target offset (prism, reflector tape)

- Distance measuring mode (infrared, red Laser)

- De-/Activation of ATR mode.

These specifications are transferred via the used GeoCOM protocols. Based on the data acquisition routines presented in figure 6.4 (section 6.2.2), the listed issues are handled. Though, because the data acquisitions for RTS, SoI or SoV are not strictly separated, taking images depends on the same

settings like a normal geodetic measurement based on the steering process of the RTS data. Especially the proclaimed switch for the activation or deactivation of the ATR mode does influence how the collimation axis of the instrument aims at the target.

Based on the tilt compensator's measurements, the long-term stability of the setup point has to be discussed. Li and Ci increase with further duration. A possible explanation might be the experimental setup. Like shown in figure 6.45 the inclination readings of target 11 and 16, which both are located near to the setup point, indicate a tilting motion. The one-sided irradiation of the sun is seen as an explanation, because it causes physical expansion of the concrete wall. A comparison of Li and Ci facing the ambient temperature change during the SoV measurement epochs depicted in figure 6.46 shows that the ambient temperature change correlates with the change of Li and Ci. In fact, the tilting of the whole setup is irreversible, because the tilt compensator does not reach its starting position. This could have caused a problem if the internal threshold of the used Leica MS60 would throw an error message due to instability.
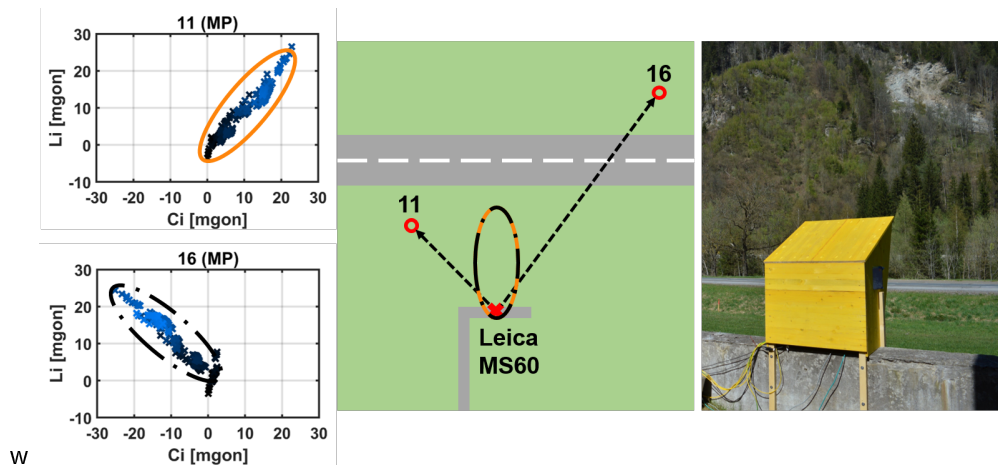
Figure 6.45: Schematic visualization of the tilting effect measured by the tilt compensator caused by the expansion of the installation site
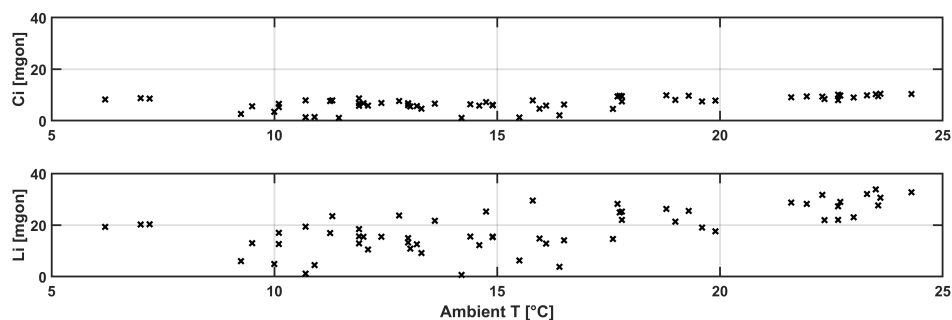
Figure 6.46: Dependency of the absolute inclinations Ci and Li facing the ambient temperature change during the SoV measurement epochs

Summing up the discussed results of the RTS observations, they have to be discussed in differentiated way. The slope distance SD is assumed to suffer from the physical change of the EDM's zero point,

which is caused by the tilting of the whole setup. The deviations in V are also linked to the inclination of the concrete wall, where the instrument is installed. The horizontal angle Hz shows a significant orientation drift during the entire measurement campaign influencing the results. When reducing Hz in terms of setting a new orientation, this impact can be compensated and furthermore also eradicates the significant changes across the LOS.

Taking the derived results of the SoI and SoV data sets into account, it has to be said, that the image quality concerning contrast is one of the most decisive parts for a valid evaluation. Bad focusing and fixed exposure settings cause insufficient image results, which affects the efficiency of the feature matching algorithm. Another aspect is the steering procedure. Here, the impact of position refinement caused by the ATR is not determinable and therefore wrongly indicates discrepancies between two images. Nevertheless, the image-based angle readings refer to the results of the RTS derived observations.

There are various techniques how to extract displacement out of an image. However, this depends on the target type which is captured. Ehrhart (2017) describes the use of ellipse fitting or template matching. As discussed in chapter 3 the different illumination situations cannot be compensated using template matching and therefore the use of a feature-based approach is preferable.

For a monitoring application like at Wald am Schoberpass, the captured sceneries have to be well defined. Here, growing or changing vegetation simulates changes between two recording epochs. Applications like bridge monitoring therefore might be more attractive due to the fact, that the scenery does not necessarily change over time depending on whether single structure elements are observed or cars maybe appear in the background. On the other hand improvements could be achieved when defining smaller areas in the recorded images or videos. Single rocks or exposed rock faces could be favourable in the context of image analysis.

The computation of the refraction angle is based on the SoV data set. The current implementation misses the modelling of the underlying surface, such as the grass height, or the impact of the wind. As shown in section 6.4 the data sets of the recorded meteorological data suffer from a lack of useful data concerning the wind orientation or wind velocity. Furthermore, the exact determination of the height over ground of the sighting axis due to the measuring geometry can only be estimated coarsely. Consequently, the obtained results are highly doubted also because the frame rate of the video data is assumed to be not sufficient enough.

As proposed in chapter 5, the measurement noise can be used as an indicator to assess angle observations. For Wald am Schoberpass, the video-based angle observations can also be evaluated based on this approach. Computing averages and corresponding standard deviations of 2 min data segments, it is possible to assess these. In figure 6.47, a compilation including both horizontal and vertical angle is given. The indicator, which depends on a slope distance of approximately 408 m and the relations

introduced in section 5.5, is marked as black line. The red crosses are those measurements, which would be excluded.
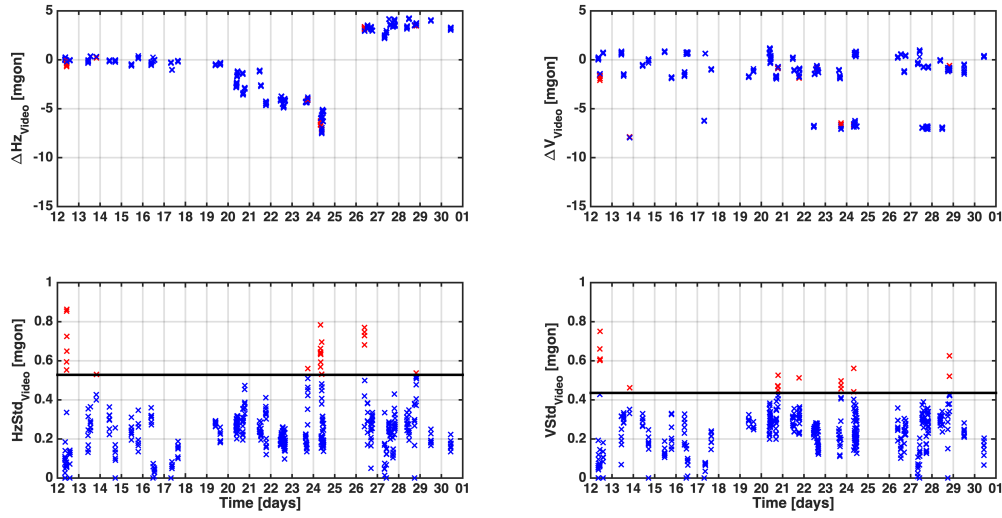
Figure 6.47: Implementing the indicator model for the video based angle observations

The indicator model from chapter 5 is meant to fit different applications. However, when taking the presented outcome depicted in 6.47, the video-based approach suffers from different aspects, which complicate the evaluation process using the self-developed routine. The noise of image-based angle measurements is not only affected by refraction, which is supposed to be related to the influence of atmospheric turbulence, but also from camera related error sources. These can arise from insufficient or varying illumination on the detector (image sensor), electronic noise coming from warm-up effects and the chosen image analysis algorithms.

Especially the feature matching procedure is affected by the resulting image quality using a resolution of 480p (640×480 px). As mentioned previously, the observed target 109 is about 408 m away. Due to the distance, the utilized video resolution is not an ideal sampling pattern. It is not as applicative as the chosen resolution for the SoI data of 2560×1920 px considering different fields of view. As a consequence, it must be said that the shooting situation for videos is not satisfying because of the large distance. To ensure useful data using a resolution of 480p, the target should be nearer to avoid blurring effects causing less contrast in each frame.

For better evaluation of video-based observations, it would necessary to perform field test in a well-defined framework concerning recording situation, image quality (exposure) and analysis. Additionally, dynamic angle readings using the ATR mode could be taken as a reference to examine the measurement noise of each approach and find similarities. For the measurement campaign at Wald am Schoberpass a corresponding comparison is not recommendable.

7 Approach for an optimized data acquisition and evaluation

Based on the knowledge gained in the chapters about the data acquisition and evaluation of the measurement campaign at Wald am Schoberpass, in this section a revised approach is suggested. To do so, different parts of the previous routines from RTS, SoI and SoV are taken and reconsidered. Therefore, own GeoCOM protocols are written to gain knowledge about the different components which are significantly important for a measurement run, such as the

- Angle encoder readings

- ATR sensor

- Image sensor

- Tilt compensator

Especially the part of taking images shows some aspects which could be developed for further field experiments. The current implementation does not consider any kind of adapting the image settings. Furthermore, the automatic exposure measurement of the used Leica MS60 could be helpful to obtain valid results. Another aspect is the idea to separate the different observation routines, especially the measurement procedure of taking images and ATR based observations.

7.1 Adapting image settings and recording procedure

In this section an approach is introduced to improve the capturing procedure of images in the means of enhancing the image quality. Based on the knowledge which was gained during the evaluation of the different data sets and especially the SoI, the current approach lacks adapting the image settings during the measurement, because only a predefined configuration is used. However, it would a be huge benefit obtaining an algorithm which varies the image settings in case of changing exposure conditions.

Furthermore, besides the idea of altering manual settings the recording procedure itself should be rethought according to reduce influences. One aspect would be the deactivation of the ATR mode. As seen in section 5, it suffers from temperature influences. Because the used camera OAC corresponds to the aiming axis of the instrument, the position refinement of ATR effects taking images and consequently in computing deformation based on the image differences.

Therefore a new routine is suggested, including ideas of compensating exposure changes and a steering process without the influence of the ATR, shown in figure 7.1. However, based on this new routine a test setup has to be manually predefined containing the angles and distances of the targets, which are included in one set.

```
          ┌──────────────────────────────┐
          │      Steering to target*      │
          ├──────────────────────────────┤
          │  Read angles from encoder     │
          │  (Hz, V) + tilt compensator   │
          │  (Ci, Li) + distance          │
          │       measurement             │
          ├──────────────────────────────┤
          │      Image recording          │
          ├──────────────────────────────┤
          │       Image analysis          │
          ├──────────────────────────────┤
          │     New image settings        │
          ├──────────────────────────────┤
          │     Capture final image       │
          ├──────────────────────────────┤
          │        Next target            │
          ├──────────────────────────────┤
          │        Second face            │
          ├──────────────────────────────┤
          │         Next set              │
          └──────────────────────────────┘
          * Steering procedure
          based on predefined
          learning set
```
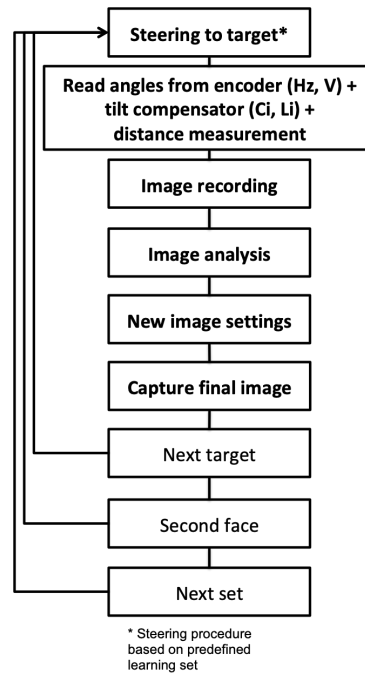
Figure 7.1: Measurement procedure when taking images. Here an image analysis step is included for adapting image settings. Furthermore, the steering process in performed based on a predefined setup of targets and is not based on the ATR method.

7.1.1 Image analysis routine

The idea of changing the image settings during the measurement procedure is mostly depending on the momentary prevalent daylight, which involves the natural daily cycle and other phenomena like current cloudiness or reflectivity. Because of the different shadowing depending on the locations of the targets, this is also a unknown influence.

The image analysation routine is based on the basic understanding of three components. In photography the image quality can be significantly enhanced through consideration of following parameters:

- Exposure time

- Sensor sensitivity (ISO)

- Aperture

However, the current operating system of the Leica MS60 provides an automatic exposure setting, which also has to be considered when redesigning the measurement routine. If the automatic exposure measurement does not provide the necessary conditions, it is important to support the instruments abilities by implementing a routine (shown in figure 7.2), which measures the exposure value of an image in real time.
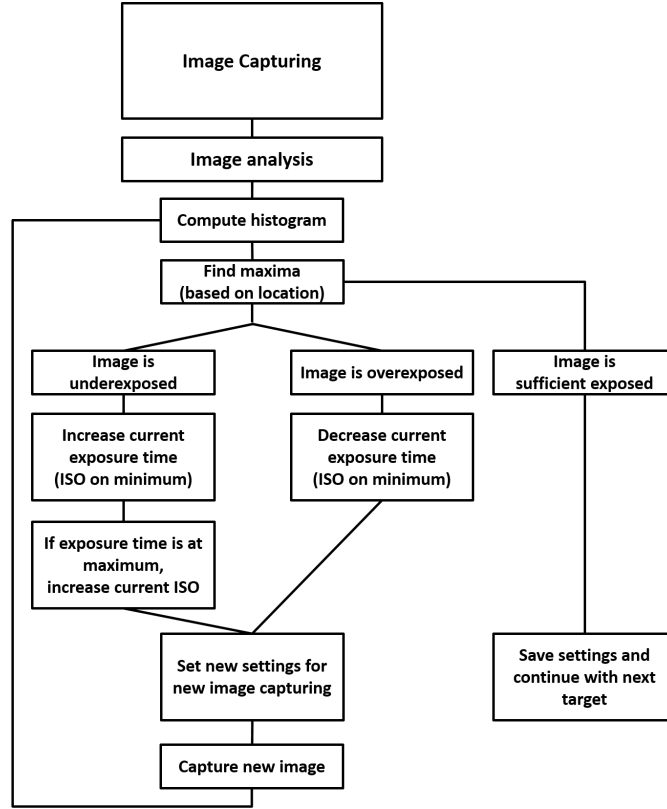
Figure 7.2: Image analysis routine showing the procedure of handling the issue of over- or underexposure

To do so, the histogram of an image indicates, whether it is over- or underexposed. It has to be determined whether the image is too dark or bright, which both do not comply with an effective feature matching procedure for detecting deformation. However, there is a high probability that different areas in an image are differently exposed, which means that there are brighter and darker areas. Based on the steering routine though, the target will be depicted more or less in the middle of the image sensor. Therefore, the centre part of the image sensor should take a more important role than the corner sections of the sensor. To compensate a heterogeneous exposure contribution in the picture, the image sensor will be arranged into 9 zones, which are used as a basis for the computation of the image greyscale maximum value. Here, the centred zone is attributed with a higher weight than the other areas, written as

$$g_{max} = \frac{g_1 + g_2 + g_3 + g_4 + 8 \cdot g_5 + g_6 + g_7 + g_8 + g_9}{16}. \tag{7.1}$$

The last step of the image analysis is the classification whether the current exposure value fits the condition of a sufficient enough exposed image or not. Therefore, a threshold is defined limiting the possible greyscale range [0+x 255-x], where x equals a predefined integer. As a result, the image analysis is similar to bracketing, known from photography. Figure 7.3 shows the idea behind bracketing to finally obtain an image which meets the condition to have the right exposure. The referring histograms indicate the exposure of the image.
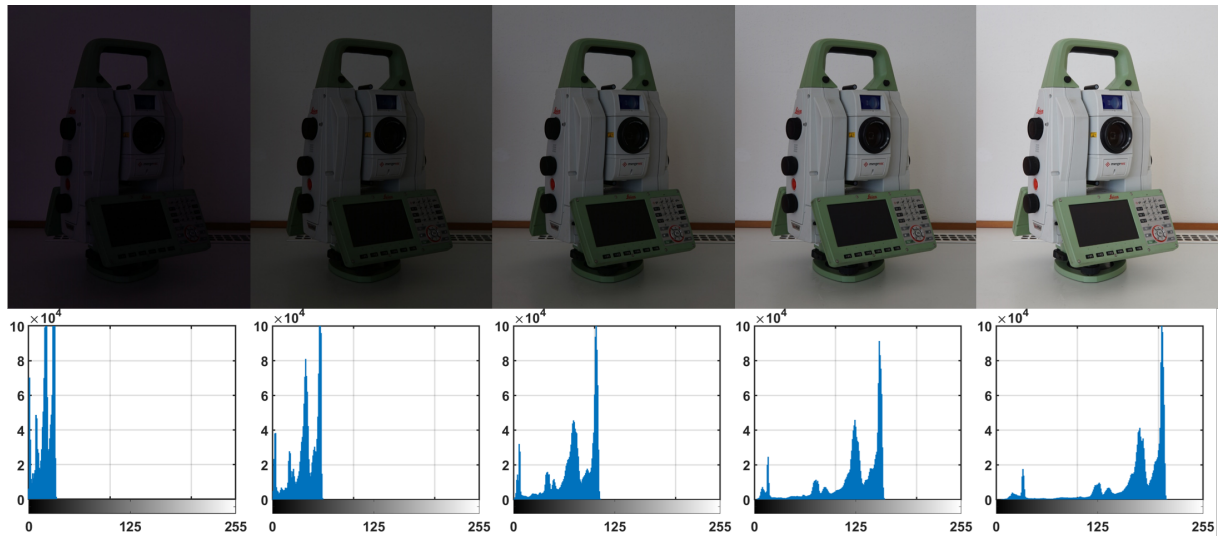
Figure 7.3: Bracketing working with predefined settings for the ISO = 100 and changing exposure time (1/50 sec, 1/25 sec, 1/13 sec, 1/6 sec, 1/3 sec).

7.1.2   Measurement setup concerning the image analysation algorithm

Based on the presented image analysation routine, a field test is performed to see whether the image quality during a real measurement application ensures better results and furthermore if changing the steering routine brings any advantage when just using a predefined angle and not using the ATR position refinement. Therefore, the Leica MS60 is installed on a surveying pillar at the institute's roof top at Steyrergasse 30 (Camups Neue Technik, University of Technology Graz). The locations of the used targets are presented in figure 7.4. The reason for choosing these on the one hand is to have different scenes concerning illumination and background. On the other hand especially the prism targets are used to obtain knowledge whether the steering process without ATR also provides useful results.
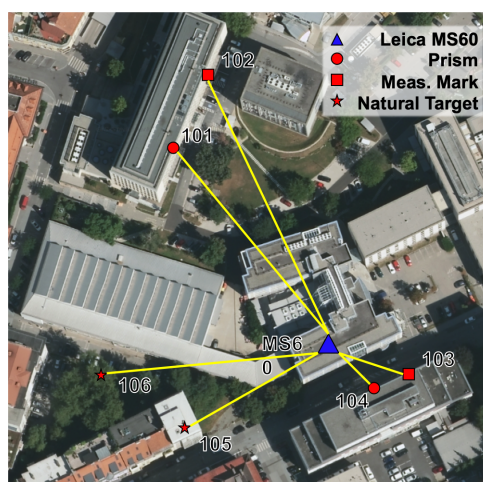
Figure 7.4: Overview of the used targets during the field test to evaluate the image analysis routine and an altered steering approach.

For the measurement procedure a manually measured set was used to define the steering angles.

Here, given Hz and V are implemented to align the telescope of the Leica MS60 in the direction of the current target. The overall following measurement procedure is performed as follows:

1. Start set measurement using the ATR for the position refinement of the telescope

    (a) Aim at current target using predefined Hz and V using the fine adjustment of ATR

    (b) After finishing a complete set (all targets measured in both faces), continue with next set

    (c) When three complete sets are measured, pass over to image recording procedure

2. Start set measurement for the image taking procedure

    (a) The set measurement procedure is performed as suggested in figure 7.1

    (b) The image taking procedure is performed as suggested in figure 7.2

    (c) After measuring three complete sets, wait until next epoch is triggered

7.1.3   Evaluation of the image analysation algorithm

To evaluate the implemented routine, different quantities are helpful. Here, the contrast of an image indicates a possible enhancement. Another opportunity would the amount of detected features, which also correspond to better contrast in an image (Sieberth et al., 2014). The contrast can be computed as

$$K = \frac{g_{max} - g_{min}}{g_{max} + g_{min}}, \tag{7.2}$$

where g_{min} and g_{max} refer to the minimum greyscale value and the maximum greyscale value of the histogram. Further image quality parameters are (Luhmann, 2018, pp.420-421):

- g_{min}, g_{max}

- Mean value of all greyscale values $\bar{g}$

$$\bar{g} = \frac{1}{M} \sum_{x=0}^{m-1} \sum_{y=0}^{n-1} s(x, y) = \sum_{g=0}^{255} g \cdot p_s(g)$$
$$p_s(g) = \frac{a_s(g)}{M} \tag{7.3}$$

Here, $p_s(g)$ refers to the relative frequency of a greyscale value based on the absolute frequency $a_s(g)$

- Entropy H

$$\sum_{g=0}^{255} [p_s(g) \log_2 p_s(g)] \tag{7.4}$$

- Symmetry α

$$\frac{-\sum_{g=0}^{k} [p_s(g) \log_2 p_s(g)]}{H}, \tag{7.5}$$

where k refers to the minimal greyscale value based on $\sum_{\mathrm{k}}^{\mathrm{g}=0} \mathrm{p_s(g)} \geq 0.5$.

These quantities have different meanings. $\mathrm{g_{min}}$ and $\mathrm{g_{max}}$ next to K also indicate the contrast of an image, whereas $\bar{\mathrm{g}}$ is used to describe the brightness of a picture. The entropy H is also known for showing the information content in an image. Its absolute value equals the mean amount of bits to code the greyscale values. The last quantity is the symmetry α indicating how symmetrical the histogram of an image is.

In figure 7.5 a comparison shown between image A, where the image evaluation routine was adapted, and image M using predefined image settings like at Wald am Schoberpass is given. It is a fitting example for how difficult the exposure measurement could be. The casing around the prism heavily reflects the light of the sun, whereas the under part is quite dark. It is visible, that working with predefined image settings for exposure time and ISO will not cover the needs of a high contrast picture. In table 7.1 the quality parameters based on their histograms is computed. Based on the results, it is possible to that variant A is better to work with due to its higher contrast and the more balanced exposure over the whole image.

Table 7.1: Image quality parameters of taken images during the image analysation field test

	$\mathrm{g_{min}}$	$\mathrm{g_{max}}$	$\bar{\mathrm{g}}$	Contrast K	Entropy H	Symmetry α
M	99	256	203.6	0.44	-4.8	-0.77
A	50	254	151.3	0.67	-5.8	-0.62

(a) Images taken from a target 101 using different settings for ISO and the exposure time
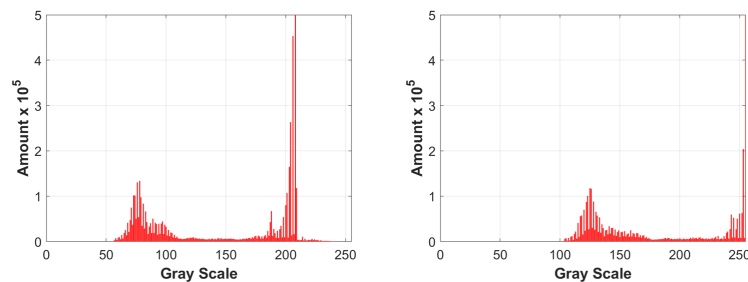
(b) Refering histograms to the taken images of target 101

Figure 7.5: Comparison of different exposure setting approaches

When working with daylight, the automatic exposure measurement of the Leica MS60 works quickly to obtain good results. However, in the evening hours the daylight is not sufficient enough. Here the image analysation routine has to alter the image settings. However, even when altering the image settings first of all its just the exposure time, which will be increased. Due to the operating system of the Leica MS60, the maximum exposure time lies at 0.48 seconds and the ISO settings are only available in large ascending steps, like table 7.2 illustrates. It is assumed, that because of the dynamic range and the low-light performance of the camera, the signal-to-noise ratio increases and therefore, even altering the image settings, the images do not bring the wanted results. However, it has to be noted, that when working with longer exposure time than 0.48 seconds, the stability during the image taking process has to be questioned if not setup on a stable pillar or in case of high frequent movements of the target.

Table 7.2: Possible variations of the ISO predefined by the Leica MS60 operating system

ISO Leica MS60	88	220	553	2212	8850

In figure 7.7 different combinations of exposure time and ISO are presented. Working with a low ISO value and a longer exposure time does not affect the image quality so much in contrast to using a higher ISO value. This is because the image sensor becomes more and more sensible to any light sources. The noise in the image finally occurs as detected features, which nevertheless can be filtered based on the outlier detection using Lowe's threshold and the RANSAC algorithm, shown in figure 7.6.
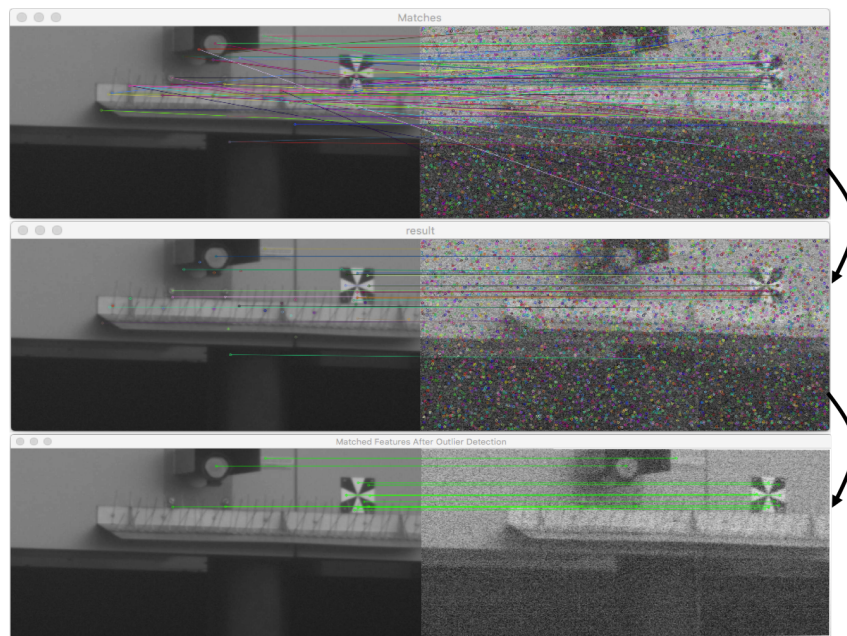

Figure 7.6: The higher noise simulates more features in the image, which however can be filtered based on the Lowe's threshold and the RANSAC algorithm. (Top: results of matching with wrong correspondeces; middle: after adapting Lowe's threshold; bottom: after adapting RANSAC algorithm
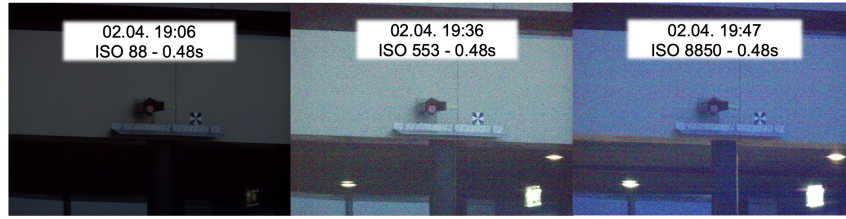
Figure 7.7: Altering image settings during dusk. The higher the ISO parameter is chosen, the more noise appears in the image.

As an overview, figure 7.8 illustrates the amount of features detected over time. To gain knowledge about the performance the automatic exposure settings of the Leica MS60, on the first only the image evaluation routine was used for taking images. On the second day, a combination of the automatic exposure measurement and the evaluation routine was implemented. Based on the amount of features detected during day 1 and day 2, both approaches achieved similar results. Nevertheless, it has to be mentioned that using the automatic exposure regulation of the Leica MS60, a set measurement is performed much quicker than starting with a predefined combination for exposure and ISO and then alter the settings stepwise. Overall, most of the time about 40-60% of the detected features can be used for further computations.

However, in the evening hours, when the prevalent daylight vanishes, both approaches will not obtain useable feature points for extraction. Here, it has to be mentioned that the used targets, because of their surroundings, are not favourable for finding features at all. Nevertheless, to compare the angle computations, the next section gives an overview and compares angle measurements derived by images and the ATR mode.
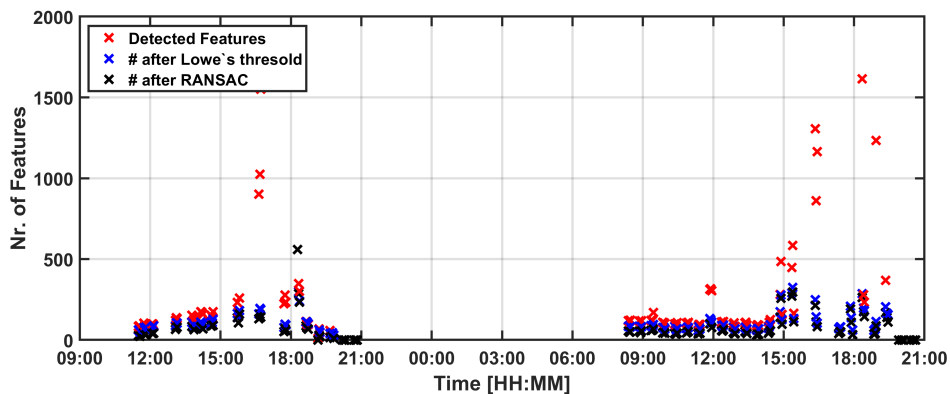
Figure 7.8: Resulting feature detection. The higher noise simulates more features in the image, which though can be filtered based on the Lowe's threshold and the RANSAC algorithm

7.1.4   Comparison of the ATR based and image based measurements

For the comparison of the steering routines, target 104 is used. The taken images are more favourable due to the fact that the plaster of the building, where target 104 is located, gives a natural pattern to the image, shown in figure 7.9.
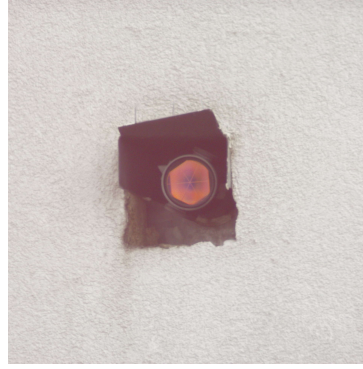
Figure 7.9: Target 104 is installed on a neighbouring building

First of all, the raw angle readings for Hz and V are shown in figure 7.10a-b. The crosses mark the ATR based readings, the circles refer to variations of the steering angle. Furthermore as a dashed line, the given steering angles from the predefined set are shown. Due to the depicted data, it is possible to see that the raw angle measurements of Hz based on ATR mode correspond to the change of the temperature. Additionally to that, there is an offset between day one and day two. This is because the Leica MS60 was dismantled from the surveying pillar and again installed for the second day, however using the same steering angle as an input for the targets. Next to the influence of the ATR, the steering process also shows some variations. Especially the vertical component has to deal with data jumps in face 1. Consequently, these variations are also visible in the face averages, depicted in figure 7.11. In contrast to that, the horizontal angle based on the ATR mode suffers from residual errors of approximately 1-2 mgon.
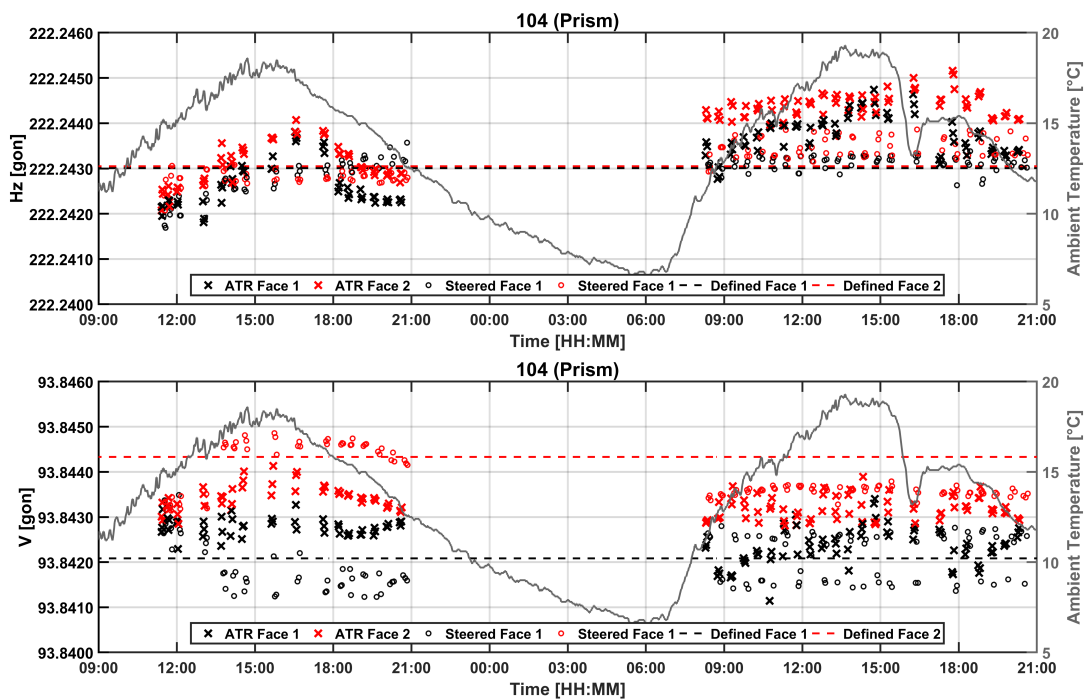
Figure 7.10: Readings of Hz and V with and without the ATR's fine adjustment
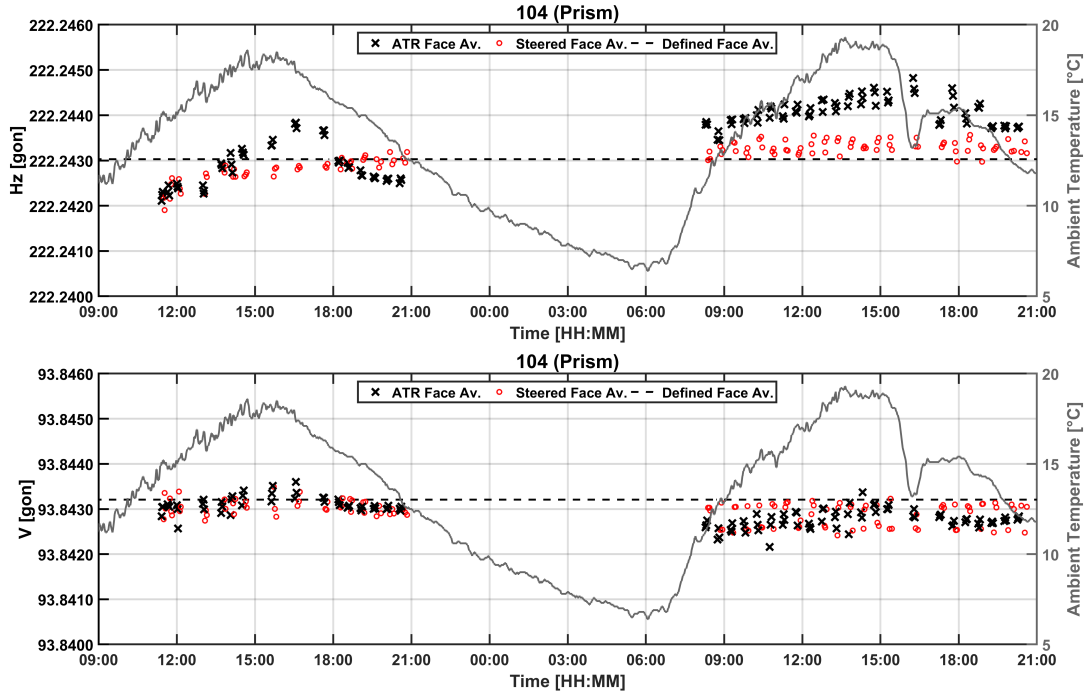
Figure 7.11: Face averages of Hz and V with and without the ATR's fine adjustment

Computing the residual errors, the differences in Hz show a maximum deviation of approximately 2 mgon referring to the ATR based measurements. The scattering of the steered angles has a range of approximately 4-6 cc. Nevertheless, these variations are compensated when it comes to the computation of the image-based angles. The idea is to mathematically correct the actual telescope alignment to simulate a stable positioning of the sighting axis and consequently of the OAC. The only variations finally should come from the feature matching process, which is explained in section 3.3.2, and the referring transformation from pixel differences to actual angles, which is explained in section 6.3.2.
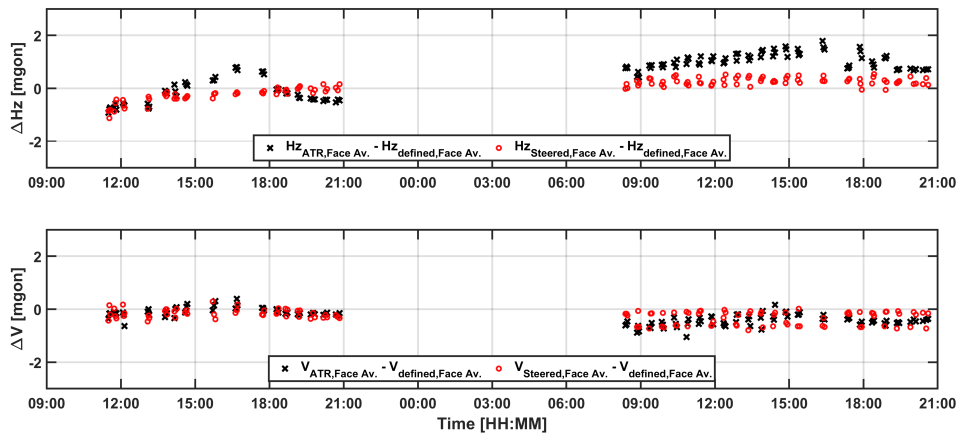
Figure 7.12: Residual errors of the face averages of Hz and V w.r.t. the predefined steering angle

Finally, having the variations of the steering process in mind, the comparison of the image based angles and the ATR based angles should yield similar results. Though as depicted in the face averages,

109

the ATR itself deals with residual errors, which cannot be eliminated via computing the face average. In section 5 a referring field test is performed to gain knowledge about these variations. For the current implementation, the residual error of the ATR is eliminated by computing the angle difference w.r.t. the first target (target 101), which is used to define the orientation of the instrument. The image-based angle measurements are corrected by the difference between the steering angles from the learning set and the actual alignment of the telescope.

Based on the results depicted in figure 7.13 there is a correspondence between the image based and ATR based angles, considering the different approaches concerning the measuring procedure. The remaining variations e.g. can come from the feature matching procedure. The position accuracy of one pixel inter alia depends on the resolution of the image sensor. The Leica MS60 indicates a scale factor of $1\,\text{px} \equiv 0.6\,\text{mgon}$ (**?**), which can be considered for rough estimations concerning achievable accuracies of image based angle measurements due to Ehrhart (2017). Based on the range of the differences between image-based and ATR based angle measurements in Hz and V, it would equal around $1\,\text{px}$. In the context of repeatability this lies within $3\sigma \equiv 9\,\text{cc}$. The measurements, which do not meet this condition can be mainly found in the vertical angle V during the evening hours. However, here the feature extraction suffers from the illumination conditions and the signal-to-noise ratio of the image sensor.
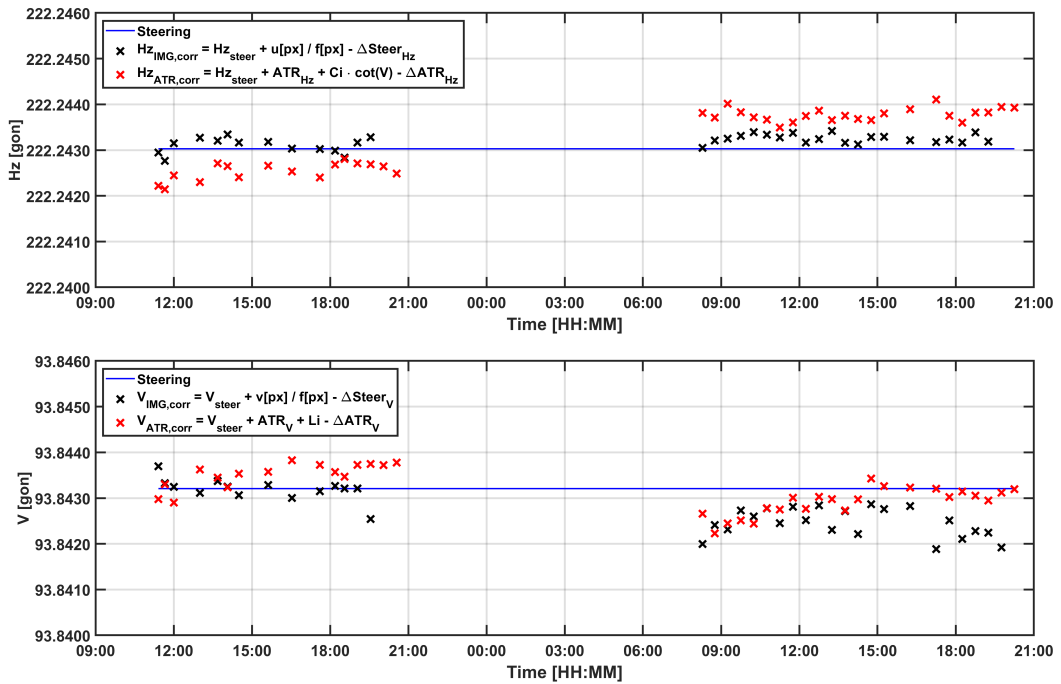
Figure 7.13: Raw angle readings influenced by the ATR zero point drift

7.2   Conclusion of the approach for improved image recording

The main aim of a better image recording procedure using a state-of-the-art IATS is the situational adaptation of image settings depending on the current illumination conditions of the scenery. Here, an approach is introduced trying to compensate the environmental limitations whether an image is over- or underexposed. Here, the used Leica MS60 offers changeable image settings, which can be user specified. These settings are the exposure time and the ISO, which both are responsible for a correct exposure of an image. Additionally, to an evaluation algorithm based on the exposure time and ISO, the automatic exposure measurement of the Leica MS60 is added into the image recording procedure. This tool fixes the exposure measurement in a shorter time, which is an advantage in real field measurements. Nevertheless, during the morning or evening hours it can come to unforeseen variations, where the image evaluation routine is of benefit being an extra control unit. Nevertheless, the dynamic range of the inbuilt image sensor of the Leica MS60 is not favourable for long exposure settings or for low-light situations. Nevertheless, having a maximum exposure time of 0.48 sec will be sufficient for working during daylight.

The second goal was to establish an altered steering routine for the static image taking procedure. In contrast to the approach chosen for Wald am Schoberpass, the now developed routine is based on simply using a given steering angle. Possible variations due to the braking process of the engine drive are compensated by computing the differences between the predefined steering angles and the actual alignment of the telescope. The outcome of the changed image recording routine is comparable to the ATR based angle measurements. For the chosen target 104, the differences between the image-based and ATR based measurements are within a range of approximately $3\sigma \equiv 9$ cc.

8 Summary and outlook

In this chapter, a summary of the derived results is given to finally state further outlook for this specific approach of performing deformation monitoring. Basis of this thesis is the evaluation of image-based measurements using a state-of-the-art IATS in the context of a landslide monitoring at Wald am Schoberpass, Styria. Here, next to other sensor types the Leica MS60 is used to derive common observations such as angle and distance measurement. Furthermore, images and videos are taken. The obtained data sets are analysed concerning quality and reliability and compared to common geodetic data. For referring investigations, the theoretical frameworks and measurement routines introduced by Ehrhart (2017) are used.

One very important aspect when working with image data, is the use of image analysis algorithms coming from the field of CV. Based on application requirements, different techniques can be used to detect information in a picture. For this thesis, mainly two ways of image registration and matching were considered, also known as the DIC and IRM technique. The DIC technique is very useful when it comes to surface deformation. One possible implementation is template matching. Here, a template window is compared to a search image to find its referring position by computing the degree of agreement between the two images via image correlation. Introducing 2D interpolation techniques, it is possible to derive subpixel accuracy, which is a huge advantage. Nevertheless, this approach strongly depends on an unique pattern (speckle pattern), which often has to be attached artificially to the surface of the object of interest. Furthermore, changes in illumination and position of the recording sensor cannot be compensated or rather lead to false or ambiguous matching results.
However, if an unique pattern is available (natural given or artificially attached) it is a very trustworthy tool to describe mechanical change. Within a field test, DIC was used to reproduce the bending motion of a grouted steel anchor. Its successful implementation proved the results derived by Monsberger et al. (2018) using DFOS.

Another way for image matching is the IRM technique detecting features in images. When matching two images, it is possible to describe the change between these based on the motion of the feature points. To ensure that these unique spots can be detected and compared, feature descriptors are introduced. Here, aspects like illumination changes, rotation and translation of the image sensor are compensated. Based on these characteristics, this technique meets the requirements to be implemented for the image evaluation at Wald am Schoberpass. For the feature detection, the SIFT algorithm is considered to evaluate the epochwise taken images as well as the video recordings. Consequently, the image based results are used to evaluate the capabilities of an IATS in the context of deformation monitoring of landslides.

Based on the current implemented image acquisition and evaluation processes, distinctive aspects have to be rethought. These mainly cover the image exposure and the recording procedure. When image editing is not considered in post processing, the exposure of images has to be adapted during the

recording procedure to compensate changing illumination. Additionally, when it comes to deformation monitoring, where epoch wise measurements of several targets are taken, the long-term stability of the sensor system has to be considered. Examples discussed by Reiterer et al. (2010) handle the process of image acquisition, image processing, feature extraction and feature matching, however they do not deal with the topic of repeatability, which seen in the context of geodetic deformation monitoring is of great importance.

The first issue, which faces both image and video recordings, is the current way of adapting image settings. At Wald am Schoberpass, these were kept constant and therefore often did not meet the current illumination situation. Next to a stable aiming procedure, it is important to obtain correct image exposure, no matter whether the images are taken during the morning hours, where the light is shallow, or the midday, where it might come to overexposure of the scene. Therefore, an image evaluation routine is implemented using the distribution of the histogram of an image as an indicator. Based on this method, it is possible to evaluate the current exposure and, after checking, correct the exposure time or ISO to obtain correct exposed images. Needing quick performance during a set measurement, the Leica MS60 offers an automatic exposure measurement which can be used for quick adaptation of the exposure settings. Summing up, the image evaluation works similar to bracketing which is often used in photography.

The second issue, which appears during the measurements, is the inconsistency concerning the telescope alignment and consequently of the OAC, which is located in the optical path of the instrument. Due to the use of ATR, the offset between target axis and sighting axis is compensated by mathematically correcting the cross hair into the centre of the prism. Nevertheless, the offset between those two axes remains in the captured scenery. As a consequence, it is a systematic effect influencing the steering process for each aiming procedure. At the current state, the ATR deviations are not readable via the GeoCOM protocol. Therefore, a field test is performed, where an altered aiming routine for capturing images is experimentally tested. This approach is based on manually defined steering angles from a learning set. As a consequence, the aiming process is only influenced by the positioning accuracy of the motorization of the Leica MS60. The corresponding deviations are determined by reading the angles of the actual orientation of the telescope ($Hz_{encoder}$, $V_{encoder}$) and then compared to the predefined angles (Hz_{steer}, V_{steer}). The computed differences are decisive for the transformation from image coordinates to absolute angles.

To avoid these variations during the recording of the videos, the current aiming routine excludes the prism tracking mode for dynamic deformation measurements. Compared to the altered steering procedure for the image recording, the current dynamic approach equals the idea of deriving useful measurements, which consequently can be introduced into the transformation of image coordinates to absolute angles. Unfortunately, during the measurement campaign at Wald am Schoberpass, the stability of the setup point of the Leica MS60 suffered from a continuous tilting motion recorded by the tilt compensator. This affects the results from the video recordings and consequently the

image-based angle results. Especially, the vertical angle shows a distinctive behaviour due to the fact, that the vertical angle is corrected by the longitudinal inclination. Here, it is absolute vital to check whether the feature matching algorithm was able to detect useful features or not. Otherwise, the video-based angle readings are overlaid by the drifting behaviour of vertical angle readings.

The computation of the refraction angle cannot be accomplished like proposed in Ehrhart (2017). This is because of missing meteorological information and rough estimations for grass heights or the average height of the LOS over ground. Therefore, the obtained results are highly doubted, also because of the fact that the frame rate is assumed to be not sufficient enough for an application like at Wald am Schopberpass. The chosen resolution combined with the focus settings result in blurry video recordings.

Generally spoken, image-based measurements are very attractive due to the fact that no targets have to be cumbersomely installed on the object of interest. Furthermore, because of the current methods implemented in CV (object tracking, feature extraction, etc.), the natural given features or structures of an object can be used instead (Ehrhart, 2017).
The automatic target recognition technique is a gladly used tool in geodetic applications. Comparing the functionality of an inbuilt camera system with the way e.g. the ATR mode in Leica instruments works, there are similarities because both using image processing. The main difference is that the ATR mode is an active sensor sending an infrared signal to detect a prism in a scene, on contrary camera system is a passive one instead. Even when the sensor resolution of the telescope camera is better, the ATR mode is very attractive for different automated monitoring applications. Nevertheless, there are distinctive deviations influencing the measurements based on the ATR mode. During a field test it was visible that the face averages, which normally are independent from instrument and zero point errors, show a range of 1.5 to 5 mgon. Seen as metric deviations, these would equal up to approximately 1 cm on 120 m. Compared to the proclaimed angle precision by the manufacturer, this residual error is significant.
Therefore, especially when dynamic ATR measurements are performed, an evaluation approach is introduced by analysing the measurement noise. An indicator is computed based on the correlation of the empiric standard deviation of angle measurements and the distance. The resultant linear relation can be used to assess an observation based on its measurement noise and rank it whether it should be considered or not.
The outcome of the referring field test yields that using such an approach, a distinctive enhancement concerning the quality assessment of measurements is achieved. Although the best time for performing measurements still is when the atmospheric conditions are stable like at night, using this approach even measurements during the day can be detected being useful. Seen in the context of a fully automated monitoring system, the measurements are classified whether they are trustworthy or not and as a consequence an erroneously triggered evacuation alarm can be controlled.

The outlook for the applicability of an IATS for different scopes is described by e.g. Ehrhart (2017) and

Reiterer and Wagner (2012). Especially the fields of deformation monitoring, vibration measurements and computation of the refraction angle are only some examples of how an IATS could be applied to solve geodetic tasks. Especially Ehrhart and Lienhart (2015a) show the use of an IATS for vibration monitoring of civil structures like bridges. However, when it comes to an epoch wise measurement with changing targets, one of the biggest issues found in this thesis is the recording procedure. Based on the application's requirements, the measurement routines have to be well-thought with regard to repeatability. This issue is to some extent handled in this thesis. Other aspects are the adaptation of illumination changes, natural given or artificially attached patterns and the use of multiple camera systems, which in the end will define the best fitting image evaluation routine based on the techniques introduced by CV. Taking a landslide monitoring as an example, the image-based approach might be useful for further investigations like for single crack monitoring, where edge- or points based methods are relevant for the image processing. For further investigations it could be useful to manually move single rocks to test other methods like shape-based matching.

For the determination of refraction caused by air fluctuation, an IATS will be a useful tool. In the context of the monitoring at Wald am Schoberpass, a valid computation was not possible due to the video quality (frame rate, resolution) and the missing meteorological data.

The main achievements of this thesis cover the recording approaches for images and videos and a measurement assessment based on the corresponding measurement noise. These aspects have to be considered for further deformation monitoring. Increasing the image quality is absolutely vital for better contrast and consequently for successful image analysis. In the field, this is done via an evaluation algorithm for a correct image exposure based on the grayscale histogram. Additionally, the steering procedure is rethought to exclude systematic effects like the position alignment of the telescope based on the ATR fine adjustment.

For the case that measurements are recorded during atmospheric unstable phases of the day, an indicator model is introduced to assess the observations based on their measurement noise. The obtained model is assumed to fit for different applications, however to ensure its value, it is recommended to perform dynamic measurements in advance to consider the prevalent measurement conditions.

In the end it has to be said that the inbuilt camera systems bring huge advantages concerning the planning and implementation of deformation monitoring. Next to documentation, its field of applications will increase, because it proved to be an equivalent to other sensor systems.

References

[Bähr and Vögtle 1991]   BÄHR, Hans-Peter ; VÖGTLE, T.: *Digitale Bildverarbeitung : Anwendungen in Photogrammetrie, Kartographie und Fernerkundung*. 2., völlig neu bearb. Aufl. Wichmann, Heidelberg, 1991. – ISBN 3-87907-224-8

[Barras and Chapotte 2017]   BARRAS, Vincent ; CHAPOTTE, Guillaume: Überwachung ohne Reflektoren. In: *Beiträge zum 18. Internationalen Ingenieurvermessungskurs, Graz* (2017). – 163-184

[Bay et al. 2008]   BAY, Herbert ; ESS, Andreas ; TUYTELAARS, Tinne ; GOOL, Luc V.: Speeded-Up Robust Features (SURF). In: *Computer Vision and Image Understanding* 110 (2008), Nr. 3, S. 346 – 359. – URL `http://www.sciencedirect.com/science/article/pii/S1077314207001555`. – Similarity Matching in Computer Vision and Multimedia. – ISSN 1077-3142

[Bayoud 2006]   BAYOUD, Fadi: Leica's Pinpoint EDM Technology with Modified Signal Processing and Novel Optomechanical Features. (2006), 01

[Brunner 1979]   BRUNNER, Fritz K.:   Vertical refraction angle derived from the variance of the angle-of-arrival fluctuations. In: *In: Refractional influences in astrometry and geodesy. Proceedings of the Symposium, Uppsala, Sweden, August 1-5, 1978. (A80-17560 05-89) Dordrecht* (1979). – p. 227-238

[Brunner 2014]   BRUNNER, Fritz K.: Diskussion der Modellierung der Vertikalrefraktion mit dimensionslosen atmosphärischen Parametern. In: *avn. Allgemeine Vermessungsnachrichten* (2014). – 121(6): 226-230

[Burger et al. 2017]   BURGER, Mathias ; NEITZEL, Frank ; LICHTENBERGER, Ralf: Einsatzpotential der digitalen Bildkorrelation zur Bauwerksüberwachung. In: *Beiträge zum 18. Internationalen Ingenieurvermessungskurs, Graz* (2017). – 165-200

[Burger and Burge 2016]   BURGER, Wilhelm ; BURGE, Mark J.:   *Digital Image Processing. An Algorithmic Introduction Using Java*. Second Edition. Springer Verlag, London, UK, 2016. – ISBN 978-1-4471-6683-2

[Bürki et al. 2010]   BÜRKI, B. ; GUILLAUME, S. ; SORBER, P. ; OESCH, H.:   DAEDALUS: A versatile usable digital clip-on measuring system for Total Stations. In: *2010 International Conference on Indoor Positioning and Indoor Navigation*, Sep. 2010, S. 1–10

[Deumlich and Staiger 2002]   DEUMLICH, Fritz ; STAIGER, Rudolf: *Instrumentenkunde der Vermessungstechnik*. 9.Auflage. Herbert Wichmann Verlag, Heidelberg, 2002. – ISBN 3-87907-305-8

[Ehrhart 2017]   EHRHART, Matthias: *Applications of image-assited total stations: Concepts, experiments, results and calibration*. Shaker Verlag, Aachen, 2017. – ISBN 978-3-8440-5636-5

[Ehrhart and Lienhart 2015a]   EHRHART, Matthias ; LIENHART, Werner: Image-based dynamic deformation monitoring of civil engineering structures from long ranges. In: *Image Processing: Machine Vision Applications VIII, SPIE Vol. 9405*. United States : SPIE, 2015, S. CD–14 p.. – ISBN 978-1-628-41495-0

[Ehrhart and Lienhart 2015b]   EHRHART, Matthias ; LIENHART, Werner: Monitoring of Civil Engineering Structures using a State-of-the-art Image Assisted Total Station. In: *Journal of Applied Geodesy* (2015). – 9(3): 174-182

[Ehrhart and Lienhart 2017]   EHRHART, Matthias ; LIENHART, Werner: Accurate Measurements with Image-Assisted Total Stations and Their Prerequisites. In: *Journal of Surveying Engineering* 143 (2017), 08, S. 04016024

[Fischler and Bolles 1981]   FISCHLER, Martin A. ; BOLLES, Robert C.: Random sample consensus: a paradigm for model fitting with applications to image analysis and automated cartography. In: *Communications of the ACM* 24 (1981), S. 381–395. – ISSN 0001-0782

[Fleckl 2006]   FLECKL, Johannes: *Präzisionsbestimmung des Prüffeldes "Dach, Steyrergasse 30" zur Überprüfung von geodätischen Instrumenten*, Technische Universität Graz, Dissertation, 2006

[GOM 2019]   GOM: GOM Correlate. (2019). – URL `https://www.gom.com/3d-software/gom-correlate.html`

[Gorny et al. 2013]   GORNY, B. ; MAIER, H.J. ; TRÖSTER, T.: *Einsatzmöglichkeiten und Anwendungsgrenzen der digitalen Bildkorrelation zur Frühdetektion struktureller und funktioneller Schädigungen und Versagensvorhersage in metallischen Werkstoffen, Werkstoffverbunden und Verbundwerkstoffen*, Technische Universität München, PhD thesis, 2013. – URL `https://books.google.at/books?id=Hu-EnQEACAAJ`

[Hartley and Zisserman 2004]   HARTLEY, Richard ; ZISSERMAN, Andrew: *Multiple View Geometry in Computer Vision*. 2nd Edition. Cambridge University Press, Cambridge, U.K., 2004. – ISBN 978-0-511-18618-9

[Heunecke et al. 2013]   HEUNECKE, Otto ; KUHLMANN, Heiner ; WELSCH, Walter ; EICHHORN, Andreas ; NEUNER, Hans: *Handbuch Ingenieurgeodäsie. Auswertung geodätischer Überwachungsmessungen*. 2., neu bearbeitete und erweiterte Auflage. Wichmann Verlag, Berlin, 2013. – ISBN 978-3-87907-467-9

[Joeckel and Stober 1999]   JOECKEL, Rainer ; STOBER, Manfred: *Elektronische Entfernungs- und Richtungsmessung*. 4., neu bearbeitete und erweiterte Auflage. Verlag Konrad Wittwer Stuttgart, 1999. – ISBN 3-87919-266-9

[Kraus 2007]   KRAUS, Karl: *Photogrammetry: Geometry fromImages and Laser Scans*. 2nd Edition. de Gruyter, Berlin, Germany, 2007. – ISBN 978-3-11-019007-6

[Lachat et al. 2017]   LACHAT, Elise ; LANDES, Tania ; GRUSSENMEYER, Pierre: Investigation of a Combined Surveying and Scanning Device: The Trimble SX10 Scanning Total Station. (2017). – Sensors 2017, 17(4), 730

[Leica-Geosystems 2006]   LEICA-GEOSYSTEMS: Leica TPS1200 - GeoCOM Reference Manual.   (2006). – URL http://webarchiv.ethz.ch/geometh-data/student/eg1/2010/02_deformation/TPS1200_GeoCOM_Manual.pdf. ISBN 754953-1.10.0en

[Leica-Geosystems 2008]   LEICA-GEOSYSTEMS: Leica TPS1200+ - White Paper. (2008). – URL https://www.gefos-leica.cz/ftp/White_papers/Total_stations/Leica_TPS1200+_Whitepaper_0709_762676_en.pdf

[Leica-Geosystems 2015a]   LEICA-GEOSYSTEMS: ATRplus - White paper. (2015). – URL https://globalsurvey.co.nz/wp-content/uploads/2014/10/ATRplus_WP.pdf

[Leica-Geosystems 2015b]   LEICA-GEOSYSTEMS: Leica TS15 - User Manual. (2015). – URL https://surveyequipment.com/assets/index/download/id/844/. ISBN 781004-6.0.0en

[Leica-Geosystems 2019a]   LEICA-GEOSYSTEMS: Leica Nova MS60 - User Manual. (2019). – URL https://leica-geosystems.com/de-at/products/total-stations/multistation/leica-nova-ms60. ISBN 836397de - 05.15 - INT

[Leica-Geosystems 2019b]   LEICA-GEOSYSTEMS: Leica Viva TS15 - Datenblatt. (2019). – URL https://w3.leica-geosystems.com/downloads123/zz/tps/Viva%20TS15/brochures-datasheet/Leica%20Viva%20TS15%20Datasheet_de.pdf

[Lienhart 2017a]   LIENHART, Werner: *Geotechnical Monitoring - Tunneling, Landslides and Building Foundations - Lecture notes.* Graz University of Technology, 2017

[Lienhart 2017b]   LIENHART, Werner: Geotechnical monitoring using total stations and laser scanners: critical aspects and solutions. In: *J.Civil Struct. Health Monit.* (2017). – 7(3): 315-324

[Lienhart et al. 2016]   LIENHART, Werner ; EHRHART, Matthias ; GRICK, Magdalena: High frequent total station measurements for monitoring of bridge vibrations. In: *Proc. Joint International Symposium on Deformation Monitoring (JISDM), Vienna, Austria* (2016)

[Lowe 2004]   LOWE, David G.: *Distinctive Image Features from Scale-Invariant Keypoints.* Computer Science Department, University of British Columbia, Vancouver, Canada, 2004. – URL https://www.cs.ubc.ca/lowe/papers/ijcv04.pdf

[Luhmann 2018]   LUHMANN, Thomas: *Nahbereichsphotgrammetrie. Grundlagen - Methoden - Beispiele.* 4., neu bearbeitete und erweiterte Auflage. Wichmann Verlag, Berlin, Germany, 2018. – ISBN 978-3-87907-640-6

[Monsberger et al. 2018]   MONSBERGER, Christoph M. ; LIENHART, Werner ; CAPOROSSI, Paolo: Distributed Fiber Optic Sensing along Grouted Anchors to Assess Curvature and Bending Character- istics. In: *26th International Conference on Optical Fiber Sensors*, Optical Society of America, 2018, S. TuE98. – URL `http://www.osapublishing.org/abstract.cfm?URI=OFS-2018-TuE98`

[Möser et al. 2012]   MÖSER, Michael ; HOFFMEISTER, Helmut ; MÜLLER, Gerhard ; STAIGER, Rudolf ; SCHLEMMER, Harald ; WANNINGER, Lambert: *Handbuch Ingenieurgeodäsie Grundlagen*. 4.Auflage. Herbert Wichmann Verlag, Heidelberg, 2012. – ISBN 978-3-87907-504-1

[Pulli et al. 2012]   PULLI, Kari ; BAKSHEEV, Anatoly ; KORNYAKOV, Kirill ; ERUHIMOV, Victor: Real-time Computer Vision with OpenCV. In: *Communications of the ACM* 55 (2012), S. 61–69. – ISSN 0001-0782

[Reiterer et al. 2010]   REITERER, Alexander ; HUBER, Niko ; ARNOLD, Bauer: Image-Based Point Detection and Matching in a Geo-Monitoring System. In: *Allgemeine Vermessungsnachrichten (AVN)* (2010), 01, S. 129–139

[Reiterer and Wagner 2012]   REITERER, Alexander ; WAGNER, Andreas: System Considerations of an Image Assisted Total Station - Evaluation and Assessment. In: *avn - Allgemeine Vermessungs- Nachrichten* 119 (2012), Nr. 3, S. 83–94. – ISSN 0002-5968

[Ryf and Studer 2014]   RYF, A. ; STUDER, M.: Erkenntnisse aus dem geodätischen Langzeitmoni- toring beim Bau des Gotthard-Basistunnels. 6 (2014), 01

[Sassa et al. 2007]   SASSA, Kyoji ; FUKUOKA, Hiroshi ; WANG, Fawu ; GONGHUI, Wang: *Progress in Lanslide Science*. Springer Berlin Heidelberg New York, 2007. – ISBN 978-3-540-70964-0

[Schirmer 1994]   SCHIRMER, W.: *Universaltheodolit und CCD-Kamera: ein unpersönliches Messsys- tem für astronomisch-geodätische Beobachtungen*. München, Germany, Technische Universität München, PhD thesis, 1994

[Sieberth et al. 2014]   SIEBERTH, Till ; WACKROW, Rene ; CHANDLER, Jim: Influence of blur on feature matching and a geometric approach for photogrammetric deblurring. In: *ISPRS - International Archives of the Photogrammetry, Remote Sensing and Spatial Information Sciences* XL-3 (2014), 08, S. 321–326

[Striewisch 2007]   STRIEWISCH, Tom!: *Digitalfotographie für Fortgeschrittene*. 2. vollständig aktualisierte Auflage. Humboldt Verlag, Hannover, Deutschland, 2007. – ISBN 978-3-89994-012-1

[Topcon 2019]   TOPCON: IS-3 Series Brochure.   (2019). –   URL `https://www. topconpositioning.com/sites/default/files/product_files/is-3_broch_7010_2096_ revc_sm.pdf`

[Trimble 2016–2017]   TRIMBLE: Trimble SX10 Datasheet.   (2016-2017). – URL `https://geospatial.trimble.com/sites/default/files/2019-03/Datasheet%20-% 20SX10%20Scanning%20Total%20Station%20-%20English%20USL%20-%20Screen.pdf`

[Varnes 1978]   VARNES, D.J.: Slope Movement, Types and Processes. In: *Landslides: Analysis and Control* 176 (1978), S. 11–33

[Vogel 2006]   VOGEL, Michael: *Vom Pixel zur Richtung: Die räumlichen Beziehungen zwischen Abbildungsstrahlen und Tachymeterrichtungen.* Darmstadt, Germany., Technische Universität Darmstadt, PhD thesis, 2006

[Walser 2005]   WALSER, Bernd H.: *Development and calibration of an image-assisted total station.* PhD thesis, No. 15773. Swiss Federal Institute of Technology Zurich, 2005

[Wang et al. 2015]   WANG, Zhaoyang ; HIEN, Kieu ; HIEU, Nguyen ; MINH, Le: Digital image correlation in experimental mechanics and image registration in computer vision: Similarities, differences and complements. In: *Optics and Lasers in Engineering* 65 (2015), S. 18 – 27. – URL http://www.sciencedirect.com/science/article/pii/S0143816614000906. – Special Issue on Digital Image Correlation. – ISSN 0143-8166

[Wasmeier 2009]   WASMEIER, Peter: *Grundlagen der Deformationsbestimmung mit Messdaten bildgebender Tachymeter.* München, Germany, Technische Universität München, PhD thesis, 2009

[Weyman-Jones 2010]   WEYMAN-JONES, Ashley: *An investigation into the accuracy and limitations of automatic target recognition in total stations*, Faculty of Engineering and Surveying, University of Southern Queensland, PhD thesis, 2010. – URL https://eprints.usq.edu.au/18405/1/Weyman-Jones_2010.pdf

[Wunderlich 2006]   WUNDERLICH, Th.: Geodätisches Monitoring – ein fruchtbares Feld für interdisziplinäre Zusammenarbeit. In: *VGI - Österreichische Zeitschrift für Vermessung und Geoinformation* (2006), Nr. 1. – Tagungsband zum 9. Österreichischen Geodätentag

[Zogg et al. 2019]   ZOGG, Hans M. ; LIENHART, Werner ; NINDL, Daniel: Leica TS30 White Paper. (2019), March. – URL https://w3.leica-geosystems.com/downloads123/zz/tps/general/white-tech-paper/WhitePaper_TS30_de.pdf